CRYSTALLIZATION STUDY OF SILICOALUMINOPHOSPHATE ZEOLITES TEMPLATED USING PYRIDINIUM CATIONS AND THEIR CATALYTIC BEHAVIORS IN ESTERIFICATION REACTIONS

AL ISSA JEHAD MOHDFATHI MOHAMMAD

UNIVERSITI SAINS MALAYSIA

2025

CRYSTALLIZATION STUDY OF SILICOALUMINOPHOSPHATE ZEOLITES TEMPLATED USING PYRIDINIUM CATIONS AND THEIR CATALYTIC BEHAVIORS IN ESTERIFICATION REACTIONS

by

AL ISSA JEHAD MOHDFATHI MOHAMMAD

Thesis submitted in fulfilment of the requirements
for the degree of
Doctor of Philosophy

June 2025

ACKNOWLEDGEMENT

Alhamdulillah, all praises to Allah for the strengths and His blessing in completing this thesis. I would like to take this opportunity to express my profound gratitude to my dear mother Hyam Obidat, my father Dr. Mohammad Fathi Al Issa, and all my family members (Hiba, Hend, Mujahed, Hanaa, Ahmad, Saad, and both little Sara and Shams) for their unwavering support and love.

Next, my deepest gratitude to my supervisor, Assoc. Prof. Dr. Ng Eng Poh for his guidance and continuous support throughout my studies.

I would also like to thank School of Chemical Sciences, Universiti Sains Malaysia for giving me an opportunity to undertake this research work in fulfilment of my PhD degree also the staff of the School of Chemical sciences and the Archaeology Centre for their help in doing all samples test for me. I would also like to thank our collaborators for carrying out solid state NMR and TPD analyses for our samples.

Lastly, my sincere appreciation to my friends, Atiqah binti Zaid, Norfarizah Hanim binti Hassan, Nur Izzati binti Nordin, Dr. Fatin Silmi, Anas Alwadi, Musab Alghodran, Tareq Zboon, Ali Kouli, Dr. Ye Zar Ni Htwe, and Dr. Mohammad Ali Diab for their endless encouragement, help and motivation which gave me strength to complete this study successfully.

TABLE OF CONTENTS

LIST OF TABLES

Page

LIST OF FIGURES

Page

LIST OF SYMBOLS

°C	degree Celsius
g	gram(s)
m	meter(s)
h	hour(s)
min	minute(s)
cm	centimeter(s)
µ	micrometer(s)
nm	nanometer(s)
ppm	part per million
kV	kilovolt(s)

LIST OF ABBREVIATIONS

AlPO	Aluminophosphate
D6R	Double-6-ring
DBA	Dibutylamine
DEA	Diethylamine
DIPA	Di-iso-propylamine
D_p	Pore diameter
DPA	Dipropylamine
EFAL	Extraframework Al
EL	Ethyl levulinate
ELc	Ethyl lactate
[EMMIM]Br	1-Ethyl-2,3-dimethylimidazolium bromide
[empy]OH	5-Ethyl-2-methyl-1-propylpyridinium hydroxide
EtOH	Ethanol
FESEM	Field emission scanning electron microscopy
EDX	Energy dispersive X-ray spectroscopy
FTIR	Fourier transform infrared spectroscopy
GC-FID	Gas chromatography with flame ionization detection
GC-MS	Gas chromatography-mass spectroscopy
HDO	Hydrodeoxygenation
IUPAC	International Union of Pure and Applied Chemistry
IZA	International Zeolite Association
IZC	Interzeolite conversion
LA	Levulinic acid

LcA	Lactic acid
MCS	Mechanochemical synthesis
MTO	Methanol-to-olefins
NLDFT	Non-local density functional theory
NMR	Nuclear magnetic resonance
OSDA	Organic structure-directing agents
PBU	Primary building units
[PPy]Br	1-Propylpyridinium bromide
SAC	Steam-assisted crystallization
SAPO	Silicoaluminophospate
SBU	Secondary building units
SDA	Structure-directing agents
S_{BET}	Surface area
S_{MIC}	Microporous characteristics
TEA	Triethylamine
TEAOH	Tetraethylammonium hydroxide
TMAOH	Tetramethylammonium hydroxide
TG-DTG	Thermogravimetric-differential thermogravimetric analysis
TEOS	Tetraethyl orthosilicate
TMS	Tetramethylsilane
To	Toluene
TPD-NH_3	Temperature-programmed desorption of ammonia
UV-Vis	Ultraviolet-visible spectroscopy
V_{tot}	Total pore volume
XRD	X-ray diffraction

8MR	Eight membered rings

KAJIAN PENGHABLURAN ZEOLIT SILIKOALUMINOFOSFAT MENGGUNAKAN KATION PIRIDINIUM DAN SIFAT PEMANGKINANNYA DALAM TINDAK BALAS PENGESTERAN

ABSTRAK

Silikoaluminofosfat (SAPO), khususnya SAPO-11 dan SAPO-5, adalah zeolit yang sangat berguna dalam industri kerana struktur liang yang unik dan kekuatan keasidannya yang sederhana. Sintesis ionotermal SAPO-11 dengan cecair ionik berasaskan imidazolium menghadapi cabaran dalam mengawal ketulenan dan morfologi, tetapi cecair ionik berasaskan piridinium masih kurang diterokai. Selain itu, asid fosforik (H_3PO_4) sebagai sumber P digunakan secara meluas dalam sintesis zeolit SAPO-5 tetapi penggunaan asid pirofosforik ($H_4P_2O_7$) masih belum dikaji dengan mendalam. Tesis ini membentangkan tiga kajian yang saling berkaitan tentang penghabluran zeolit SAPO. Kajian pertama mengkaji penghabluran SAPO-11 dalam keadaan ionotermal menggunakan 1-propilpiridinium bromida ([PPy]Br) sebagai acuan. Kesan parameter sintesis dikaji, dan SAPO-11 bersifat asid dan mempunyai luas permukaan yang tinggi dapat disintesis selepas 133 jam pemanasan pada 150 °C. Kajian kedua menerokai penghabluran SAPO-5 dalam keadaan hidrotermal menggunakan 5-etil-2-metil-1-propilpiridinium hidroksida ([empy]OH) sebagai acuan baharu, di mana H_3PO_4 dan $H_4P_2O_7$ digunakan sebagai sumber P perbandingan. Kedua-dua proses penghabluran diikuti, dan kesan sumber P ini terhadap penghabluran dan sifat struktur SAPO-5 dikaji. Penemuan mendedahkan H_3PO_4 menghasilkan hablur SAPO-5 berstruktur hierarki yang berkeasidan tinggi, manakala $H_4P_2O_7$ menggalakkan penukleasan dan menghasilkan SAPO-5 berbentuk nano-kepingan yang mempunyai liang tekstur meso. Komponen ketiga memberi tumpuan

kepada prestasi pemangkinan zeolit SAPO yang disintesis. SAPO-11 yang dihablurkan secara ionothermal menunjukkan keaktifan mangkin yang luar biasa (93.4% penukaran, 100% kepilihan) dalam penukaran asid levulinik kepada etil levulinat dalam keadaan pemanasan segera bukan gelombang mikro (180 °C, 30 min), dan prestasinya adalah lebih baik daripada mangkin homogen konvensional. Sementara itu, SAPO-5 yang disintesis dengan [empy]OH menggunakan sumber H_3PO_4 dan $H_4P_2O_7$ diuji dalam pengesteran asid laktik untuk membentuk etil laktat. SAPO-5 yang disintesiskan dengan H_3PO_4 menunjukkan prestasi yang lebih baik (87.0% penukaran, 100% kepilihan) daripada rakan saingannya, dan prestasinya setanding atau lebih baik daripada mangkin homogen H_2SO_4 (100% penukaran, 86.3% kepilihan), HCl (100% penukaran, 90.1% kepilihan) dan H_3PO_4 (57.1% penukaran, 92.0% kepilihan). Kedua-dua SAPO-11 dan SAPO-5 menunjukkan kebolehgunaan semula yang tinggi dengan kehilangan keaktifan yang minimum selepas kitaran tindak balas ke-5.

CRYSTALLIZATION STUDY OF SILICOALUMINOPHOSPHATE ZEOLITES TEMPLATED USING PYRIDINIUM CATIONS AND THEIR CATALYTIC BEHAVIORS IN ESTERIFICATION REACTIONS

ABSTRACT

Silicoaluminophosphates (SAPO), particularly SAPO-5 and SAPO-11, are very useful zeolites in industry due to their unique pore structures and mild acidity. Ionothermal synthesis of SAPO-11 with imidazolium-based ionic liquids faces challenges in controlling purity, while pyridinium-based ionic liquids as an alternative remain under explored. In addition, the use of phosphoric acid (H_3PO_4) as a P source is widely studied in the synthesis of SAPO-5 zeolite but the use of pyrophosphoric acid ($H_4P_2O_7$) remains under examined. This thesis presents three interconnected studies on the crystallization of SAPO zeolites. The first study investigates the crystallization of SAPO-11 under ionothermal conditions using 1-propylpyridinium bromide ([PPy]Br) as template. The effects of synthesis parameters are studied, and SAPO-11 with an acidic nature and high surface area is successfully synthesized after 133 h of heating at 150 °C. The second study explores the crystallization of SAPO-5 under hydrothermal conditions using 5-ethyl-2-methyl-1-propylpyridinium hydroxide ([empy]OH) new template, where H_3PO_4 and $H_4P_2O_7$ are used as comparative P sources. Both crystallization processes are followed, and the effects of these P sources on the crystallization and structural properties of SAPO-5 are examined. The findings reveal that H_3PO_4 yields highly crystalline hierarchical SAPO-5 with high acidity, whereas $H_4P_2O_7$ promotes nucleation, forming SAPO-5 nanoplates with textural mesoporosity. The third component focuses on the catalytic performance of synthesized SAPO zeolites. The ionothermally synthesized SAPO-11 demonstrates

remarkable catalytic activity (93.4% conversion, 100% selectivity) in the conversion of levulinic acid into ethyl levulinate under non-microwave instant heating conditions (180 °C, 30 min), which is better than conventional homogeneous catalysts. Meanwhile, the SAPO-5 crystallized with [empy]OH using H_3PO_4 and $H_4P_2O_7$ sources is tested in the esterification of lactic acid. H_3PO_4-synthesized SAPO-5 (87.0% conversion, 100% selective to ethyl lactate) shows better performance than the other counterpart under optimized catalytic conditions (160 °C, 20 min), and its performance is comparable or even better than homogeneous H_2SO_4 (100% conversion, 86.3% selectivity), HCl (100% conversion, 90.1% selectivity) and H_3PO_4 (57.1% conversion, 92.0% selectivity) catalysts. Both SAPO-11 and SAPO-5 show high reusability with only minimal activity loss after 5^{th} reaction runs.

CHAPTER 1

INTRODUCTION

1.1 Background

Zeolites represent a significant category of inorganic crystalline materials that are extensively used in petrochemical and fine chemical industries. They are used as catalysts, adsorbents and ion-exchangers. The development of zeolite molecular sieves dates back in 1950s where these materials were initially designed for gas separation processes (Zones et al., 1996). Zeolites are characterized by their uniform microporosity with diameters less than 2 nm. This framework is mainly composed of TO_4 tetrahedra, where T can be silicon (Si), aluminum (Al) or phosphorus (P). The linkage of TO_4 units results in the formation of various three-dimensional crystalline framework structure. So far, more than 250 types of framework structures have been discovered and synthesized (IZA, 2024).

Silicoaluminophosphates (SAPO) are one of the important classes of zeolites. Among SAPO zeolites, SAPO-11 (AEL topology) is widely used in industry due to its unidimensional channels with elliptical pores of 4.0 × 6.5 $Å^2$. This specific pore structure makes SAPO-11 particularly suited for various catalytic reactions, such as the hydroisomerization of n-paraffins (Dai et al., 2022), dewaxing (Blasco et al., 2006), hydrodeoxygenation (HDO) of vegetable oils (Rabaev et al., 2015), n-alkane cracking (Xing et al., 2019), and oxidation of cyclohexane (Xiao et al., 2016). Furthermore, the unique pore shape of SAPO-11 also gives high product selectivity in these reactions, making it a valuable catalyst in the petrochemical industry.

Traditionally, SAPO-11 is synthesized *via* hydrothermal route using amine or quaternary ammonium salts as organic structure-directing agents (SDA) (Said & Zaky, 2022). The use of these organic species is crucial to ensure the formation of pure SAPO-

11 with distinct morphological structures (Ahmad et al., 2020; Auwal et al., 2020; Tiuliukova et al., 2018). In 2004, a novel ionothermal method was introduced, whereby ionic liquids or deep eutectic solvents are used as solvent and SDA (Cooper et al., 2004). This system is better compared to hydrothermal synthesis, as the zeolite synthesis can be performed under ambient pressure (Han et al., 2023). In addition, the ionothermal approach also offers other advantages, including better negligible vapor pressure, thermal stability, tunable hydrophilicity, and high reusability (Welton, 1999). So far, several SAPO zeolites have been synthesized using this route (imidazolium ionic liquids are used) including SAPO-5 (Khoo et al., 2014), MnAlPO-5 (Ng et al., 2009), SAPO-34 (Fortas et al., 2018), SAPO-LTA (Lin et al., 2019), and GaPO-LTA (Ma et al., 2009). However, the crystallization of SAPO-11 *via* ionothermal synthesis so far can only be achieved with the assistance of microwave heating (Xu et al., 2006).

Besides SAPO-11, SAPO-5 (AFI topology) is another important zeolite in the SAPO family. SAPO-5 consists of 12-membered ring with one-dimensional pore channels of 7.3 × 7.3 Å² (Auwal et al., 2020). Its large pore channels facilitate molecular diffusion and accessibility, thus making SAPO-5 highly effective in catalytic applications, for example in the conversion of methanol to olefins (Yang et al., 2019), alkylation of toluene (Yang et al., 2019), isomerization of xylenes (Basina et al., 2018; Ma et al., 2022; Terasaka et al., 2015), acetylation of 2-methylfuran (Auwal et al., 2020), and transesterification of triacetin (Jadav et al., 2020).

SAPO-5 can be synthesized using various techniques such as hydrothermal (Ali et al., 2020), microwave (Ng et al., 2019), ionothermal (Feng et al., 2019), steam-assisted crystallization (SAC) and dry gel conversion (Deneyer et al., 2020; Ma et al., 2022) methods. For SAPO-5, several compounds have been identified as the organic templates for crystallizing this zeolite, namely choline (Zhao et al., 2012), 1-ethyl-2,3-

dimethylimidazolium bromide ([EMMIM]Br) (Feng et al., 2019), tetraethyl orthosilicate (TEOS) (Radnik et al., 2019), triethylamine (TEA) (Shao et al., 2015) and tetraethylammonium hydroxide (TEAOH) (Ng et al., 2019). The selection of these structure-directing agents, based on factors such as ionic charge, hydrophobicity, molecular dimensions, and shape, critically influences the crystallization process, resulting in the formation of SAPO-5 crystals with diverse morphologies (e.g. hexagonal cylindrical (Basina et al., 2018), plate-like (Auwal et al., 2020), barrel-shaped (Mortén et al., 2018), prismatic (Auwal et al., 2020; Wang et al., 2021), broom-like (Li et al., 2012), flower-like (Jhung et al., 2004), disc-like (Khoo et al., 2013), and spheroidal shapes (Mintova et al., 1998; Zhao et al., 2009).

Besides SDA, the synthesis of SAPO zeolites is also governed by the type of inorganic sources used. Typically, phosphorus (P) plays a very important role in directing the formation of pure SAPO zeolite because it is one of the primary building blocks of SAPO zeolites. Usually, phosphoric acid (H_3PO_4) is used as a P source for crystallizing SAPO zeolites because it is reactive and exists readily as tetrahedral P building unit in the framework structures (Majano et al., 2011). Additionally, non-conventional P sources like phosphorous acid (H_3PO_3) have been applied in P-based zeolite synthesis, such as SAPO-41 (Ma et al., 2006) and NKX-2 (Abdullahi et al., 2019), showing their distinct effects and unique properties as compared to those synthesized using H_3PO_4. Hence, the use of different P sources offers new routes for designing and synthesizing SAPO zeolites, allowing researchers to broaden the scope of zeolite synthesis techniques and enhance our understanding of zeolites.

1.2 Problems statement

Classical method for synthesizing SAPO-11 typically involves hydrothermal route (150–200 °C) utilizing amine or quaternary ammonium salts as organic SDA. Nevertheless, this method has limitations in terms of controlling the purity and morphology of SAPO-11 besides using high pressure synthesis conditions (>40 bar). Recently, ionothermal synthesis has emerged as a promising alternative. However, research has predominantly focused on imidazolium-based ionic liquids. There is a lack of studies exploring the use of other N-heterocyclic ionic liquids, such as pyridinium-based ionic liquids. Hence, an investigation of using pyridinium ionic liquid for crystallizing SAPO-11 is needed as it might exert other physicochemical properties which are beneficial for catalytic reactions.

Meanwhile, the synthesis of SAPO-5 usually uses H_3PO_4 as a P source. The use of H_3PO_4, however, has drawbacks, such as rapid nucleation, limited control over crystal size and morphology. These limitations affect phase purity and the catalytic properties of SAPO-5. The use of other P sources is still under study. Hence, there is a need to explore alternative P sources to better understand their roles for designing SAPO zeolites for specific applications. Pyrophosphoric acid is a polyphosphoric acid with a molecular formula of $H_4P_2O_7$. It consists of two phosphate groups linked by a bridging oxygen atom and tends to hydrolyze in water, forming an equilibrium mixture of H_3PO_4 and $H_4P_2O_7$. By controlling the slow hydrolysis of $P_2O_7^{4-}$ species during crystallization, it has been shown that it is able to regulate the incorporation of Si species into the framework of SAPO zeolite (Zhao et al., 2022). This strategy suggests a new approach for synthesizing P-based zeolites with distinct characteristics, which is worth for further investigation.

1.3 Research objectives

The objectives of this study are:

i. To study the crystallization synthesis of SAPO-11 under ionothermal conditions where 1-propylpyridinium bromide ([PPy]Br) is used as the solvent and template.

ii. To study the crystallization process of SAPO-5 synthesized using phosphoric acid (H_3PO_4) and pyrophosphoric acid ($H_4P_2O_7$) as phosphorus sources, where 5-ethyl-2-methyl-1-propylpyridinium hydroxide ([empy]OH) serves as a new organic template.

iii. To evaluate the catalytic performance of SAPO-11 in the esterification of levulinic acid, and SAPO-5 in the esterification of lactic acid under non-microwave instant heating conditions.

1.4 Scope of study

This study focuses on three aspects. First, the study focuses on the ionothermal synthesis of SAPO-11 using [PPy]Br ionic liquid. Prior study, [PPy]Br is first prepared by reacting pyridine and 1-bromopropane where the purity of the ionic liquid is checked by infrared (IR), proton nuclear magnetic resonance (^{1}H NMR) and CHN analyses. Then, the synthesis parameters, such as crystallization temperature, synthesis time, reagent amounts (P, Si, ionic liquid), will be systematically varied to study their respective effects on the crystallization process. During this study, X-ray Diffraction (XRD) and Scanning Electron Microscopy (SEM) techniques are used to investigate the crystallization and morphological properties of SAPO-11. Thermogravimetric Analysis/Derivative Thermogravimetry (TGA/DTG) and ^{13}C Magic Angle Spinning Nuclear Magnetic Resonance (^{13}C MAS NMR) are also used to prove the direct

participation of [PPy]Br in the crystallization of SAPO-11 as pore filler for stabilizing the framework structure.

Second, this study is devoted on the use of different P sources, namely, H_3PO_4 and $H_4P_2O_7$, to synthesize SAPO-5 in order to study the effects of P source on SAPO-5. Prior study, [empy]Br is first synthesized, purified and confirmed by IR, ^{1}H NMR and CHN analyses. The pure [empy]Br is then ion-exchanged to convert into [empy]OH prior use as organic SDA. The synthesis of SAPO-5 is subsequently performed using similar synthesis recipe and crystallization conditions but different P sources (H_3PO_4 and $H_4P_2O_7$). The comparative study is then characterized using various techniques, such as XRD, FTIR, TGA/DTG, SEM, ^{27}Al and ^{31}P MAS NMR.

Third, the study focuses on the catalytic performance of prepared SAPO zeolites where SAPO-11 is first tested in the esterification of levulinic acid (LA) with ethanol (EtOH). On the other hand, SAPO-5 is tested in the esterification of lactic acid (LcA) with EtOH. Prior the catalytic reactions, the SAPO-11 and SAPO-5 are calcined in order to open their pores. The zeolite catalysts are then measured with N_2 adsorption to study their surface porosity. In addition, their surface acidity is also analyzed with temperature-programmed desorption of ammonia (TPD-NH_3) and/or pyridine adsorption. The catalytic reactions are then performed inside a silicon carbide (SiC) superheat conductor, where this heating condition can mimic rapid heating like microwave heating. The reaction performance is then monitored using a gas chromatography with flame ionization detection (GC-FID) and gas chromatography-mass spectrometry (GC-MS). Furthermore, the effects of catalytic reaction parameters, such as reaction temperature, time duration, catalyst loading, reactants ratio, mode of heating, type of catalysts, are also studied.

The use of pyridinium-based ionic liquids for the ionothermal synthesis represents a novel approach that could lead to the development of SAPO zeolites with unique surface and structural properties. Similarly, exploring alternative P sources and organic templates for the synthesis of SAPO zeolites can enhance the understanding of crystallization and physicochemical properties of these zeolites. This research could pave the way for the design and synthesis of zeolites tailored for specific industrial applications, thereby broadening the scope of zeolite synthesis techniques and enhancing their practical applications in various catalytic processes.

1.5 Outline of thesis

This thesis comprises seven chapters that encompass the background, experimental procedures, research findings, conclusion and recommendations for the project.

Chapter 1 serves as an introduction, providing general information of this research. This chapter also includes the problems statement, objectives, scope and outline of this study.

Chapter 2 describes a comprehensive literature review, detailing the history of zeolites, their framework structures and properties, fundamental concepts of zeolite synthesis, and their applications, particularly in heterogeneous catalysis.

Chapter 3 outlines the experimental methodology used in this study. It describes the chemicals, and the protocols employed for synthesizing SAPO-11 and SAPO-5. In addition, the procedures to study the effects of synthesis parameters on the crystallization of SAPO-11 are also mentioned. Furthermore, the protocols for studying the effects of P sources on SAPO-5 are described too. This chapter also details the experimental set-up for catalytic esterification reactions while the conditions of characterization techniques used in this study are elaborated as well.

Chapter 4 presents the results of the ionothermal synthesis of SAPO-11 zeolite. In this chapter, the effects of various synthesis parameters, such as heating time, temperature, ionic liquid content, amount of water and silica concentration, on the crystallization of SAPO-11 are investigated. Furthermore, the roles of [PPy]Br as pore filler and a stabilizer are also studied.

Chapter 5 discusses the results of synthesis of SAPO-5 zeolites templated by [empy]OH where H_3PO_4 and $H_4P_2O_7$ as different P sources are investigated. In this chapter, the crystallization evolution of SAPO-5 is followed using spectroscopy and microscopy techniques. The roles of both P sources on the formation are then elucidated based on the findings observed.

Chapter 6 focuses on the study of catalytic behavior of SAPO-11 and SAPO-5 where esterification of LA and LcA reactions are performed, respectively. Additionally, this chapter also studies the effects of reaction parameters, such as heating temperature, time, activation temperature, catalyst loading, type of catalyst, reactant ratio, etc. on the performance of SAPO catalysts. The mechanisms of these organic reactions catalyzed by SAPO zeolites are also proposed.

Lastly, Chapter 7 concludes the research findings. Some recommendations for future work in this area of research are also provided.

CHAPTER 2

LITERATURE REVIEW

2.1 Zeolites as microporous materials

Current applications of microporous materials, particularly zeolites, as adsorbents and catalysts in the hydrocarbon processing (oil refining) sector are widespread. Zeolites are used as catalysts in the hydrocarbon processing industry because of their high and adjustable acidity as well as their unique pore architectures, which have channels and cavities with molecular dimensions that enable shape-selective conversions of organic compounds (Rizzo et al., 2000).

Depending on the number of tetrahedral (T) atoms at the pore opening, zeolites can be categorized based on small, medium, large and extra-large pores. 8T atoms are present in zeolites with small pores, 10T is considered medium pores, and 12T are those with large pores. More than 12T atoms can be found in the pore opening of extra-large pore zeolites (Raman, 2023).

The International Union of Pure and Applied Chemistry (IUPAC) divides porous materials into three classes based on the size of their pores: micropores (<2 nm), mesopores (2–50 nm), and macropores (>50 nm) (Bleta et al., 2018). Zeolites are considered as microporous materials due to their pore size <2 nm. Figure 2.1 shows some common microporous zeolite materials with molecular diameter in the range of <2 nm while mesoporous silica materials have pore size ranging from 2-10 nm.

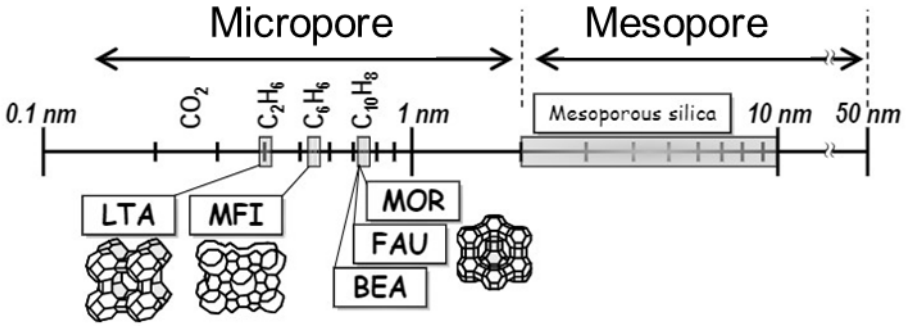

Figure 2.1 Pore sizes of molecular sieves and molecular sizes (Tago & Masuda, 2010)

2.2 What are zeolites?

Zeolites are crystalline aluminosilicates with molecularly dimensional pore channels. Zeolites differ from materials with comparable chemical compositions in that they are characterized by framework structures (Chai et al., 2021). Zeolites were first identified in 1756 but they were only first studied scientifically (including application and synthesis) at the end of 19th century (Millini & Bellussi, 2017). Since then, the zeolite family has experienced substantial growth with 255 topological configurations are identified up to now. Apart from the original Si and Al atoms, the diversity of framework building atoms has also increased to include other heteroatoms such as Ti, Sn, Zr, Fe, P and so on (Xu & Wu, 2022).

Zeolites have a general formula of $A_{x/n}(SiO_2)(AlO_2)_x \cdot mH_2O$, where A denotes a cation (Li et al., 2021). Zeolite is a three-dimensional material made up of networks of tetrahedral $[SiO_4]^{4-}$ and $[AlO_4]^{5-}$ atoms connected by oxygen atoms, as in Figure 2.2. Because of their porous nature and ion-exchange capabilities, zeolites have a wide application nowadays, including environmental, industrial, agricultural, petrochemical and biomedical sectors. Natural zeolites that can be obtained naturally are utilized as building materials and in the paper industry. Along with other uses, agriculture makes use of them as fertilizers. Zeolites produced in laboratories with specific pore sizes are used in various applications, including adsorbents and catalysts. In addition, zeolites are

used as molecular sieves for the removal of radioactive pollutants in laundry. Other benefits of synthetic zeolites are their superior ion exchange properties, uniform crystal size and high purity (Khaleque et al., 2020).

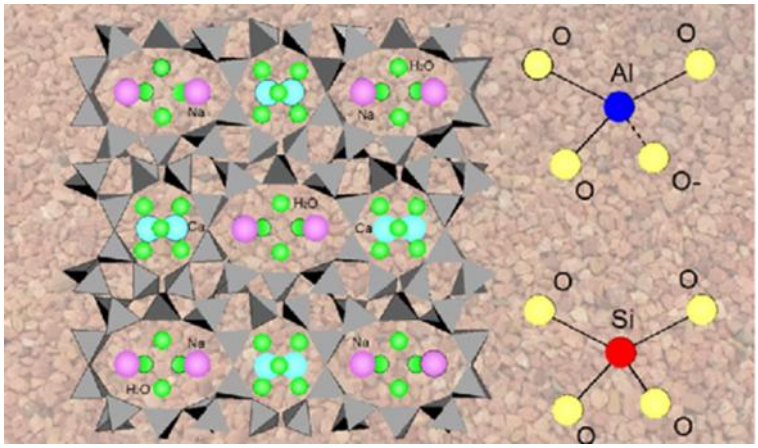

Figure 2.2 Zeolite structure with three-dimensional framework (Santiago et al., 2016)

Because of the homogeneity of crystal size and high purity of crystalline products, synthetic zeolites are widely used in the commercial sector than natural zeolites. They are also employed as chemical sensors in numerous applications, such as medical monitoring, gas collection, heavy metals removal, industrial process control and environmental mitigation. Because of their considerable flexibility and adaptability, scientists and researchers have become interested in synthetic zeolites. Compared to natural zeolites, synthetic zeolites have additional advantages. For example, synthetic zeolites have larger pore volumes than natural zeolites, making them more superior in capturing different types of pollutants from both water and the air. Hence, synthetic zeolite will take the place of natural zeolites due to its many excellent properties over natural zeolites (Moshoeshoe et al., 2017).

2.3 Structural building units, topology codes and framework structures

Zeolites are constructed by primary building units (PBU) that consist of four inter-linked metal-oxo tetrahedral (TO_4, T = Si^{4+}, Al^{3+}, P^{5+}, etc.), forming a variety of three-dimensional (3D) secondary building units (SBU) that are essential for making frameworks with regular channels and cavities (Figure 2.3 and Figure 2.4). The number of possible zeolite structures formed is theoretically unlimited, but the International Zeolites Association (IZA) has identified over 250 different types of zeolitic topologies which can be represented with a unique three-letter code (Baerlocher & McCusker, 2017). For example, zeolite A or so-called Linde Type A has an IZA code of LTA. Zeolite X and Y, which belong to faujasite family, have topological code of FAU. Some zeolite structures with their IZA codes are shown in Table 2.1.

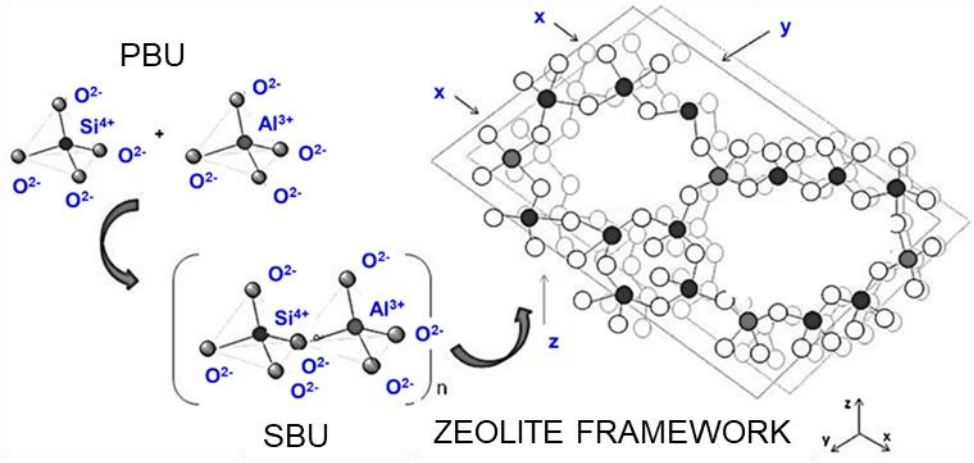

Figure 2.3 The connection of primary building unit (PBU), forming a secondary building unit (SBU) which is important for constructing a zeolite framework (Sani et al., 2014)

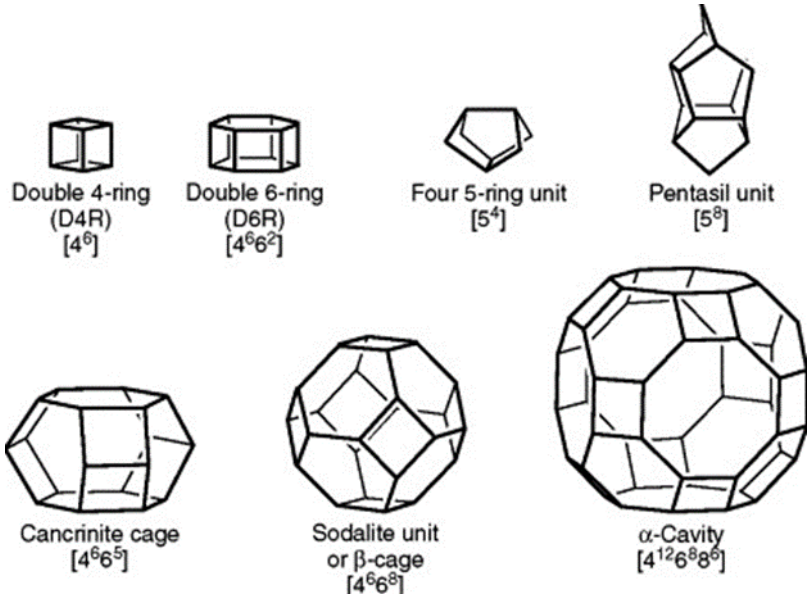

Figure 2.4 Some of the secondary building units (SBU) in cage form found in zeolites (Saleh, 2022)

Table 2.1 Some zeolite structures with their three topological codes named by IZA

Code	Structure	Number of membered ring	Pore size ($Å^2$)	Example(s)
AEI	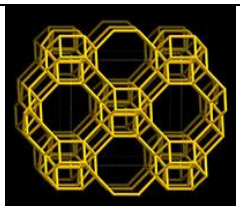	8	3.7 × 3.8	AlPO-18, SAPO-18
AEL		10	4.0 × 6.5	SAPO-11
AFI	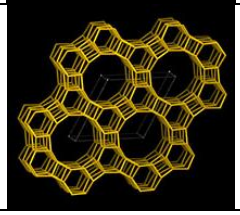	12	7.3 × 7.3	AlPO-5, SAPO-5

ATO	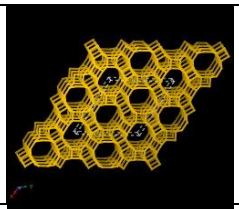	10	6.1 × 6.7	SAPO-31
CHA		8	3.8 × 3.8	SAPO-34
FAU	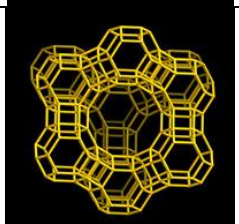	12	7.3 × 7.3	X, Y, SAPO-47
GIS	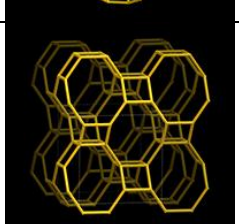	8	2.6 × 4.3	SAPO-43, P
LTA	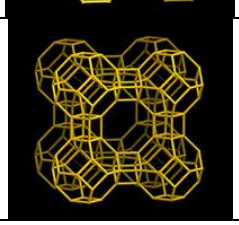	8	4.1 × 4.1	A, SAPO-LTA

2.4 Properties of zeolites

2.4.1 Zeolites as ion exchangers

Ion exchange capacity is an important characteristic of zeolites, where the cations within the zeolite structure can be replaced with external ions from the solution (Wen et al., 2018). These properties result from the isomorphous substitution of an aluminum ion (Al^{3+}) for the silicon ion (Si^{4+}) in the zeolite structure, which gives rise to a negative charge. In order to create a neutral charged zeolite framework, inorganic cations (e.g. Na^{+}) are needed to balance this negative charge. In an ion exchange process, different cations can readily replace the Na^{+} cation in the zeolite framework (Figure 2.5) (Samanta et al., 2018).

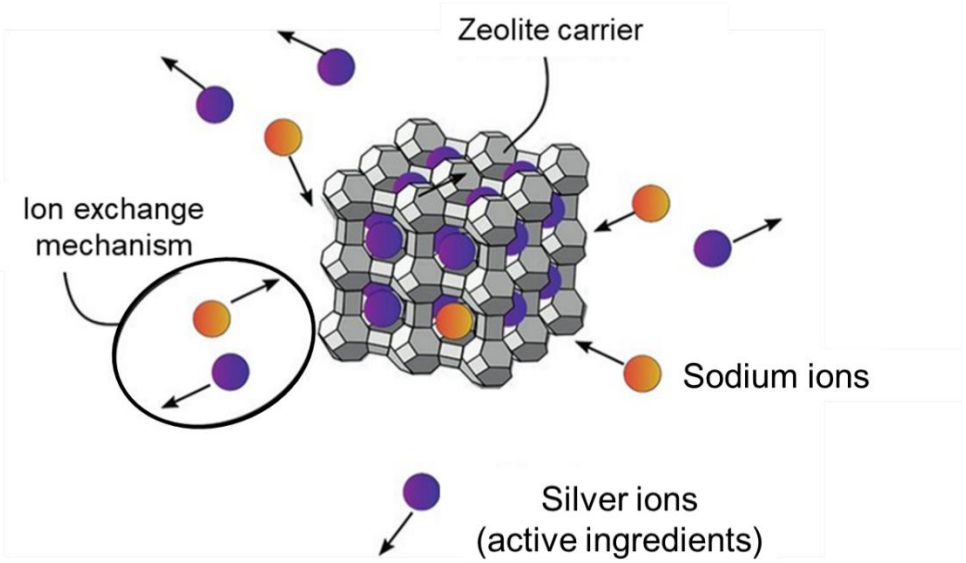

Figure 2.5 Ion exchange mechanism in zeolite loaded with silver ions (zeolite as ion exchanger) (Marturano et al., 2017)

2.4.2 Zeolites as catalysts

Zeolites are also used as catalysts in industry for the production of fuel from petroleum. The catalytic capabilities of zeolites are the result of their surface acidity that possesses Brønsted and Lewis acid sites (Figure 2.6). In order to create these protonated active sites, the original Na^+ cations have to be exchanged with ammonium cation and calcined. The formation of the hydroxyl group on the zeolite surface has a strong electrostatic field and can attract organic reactant molecules for chemical reactions. Some chemical reactions that are catalyzed by zeolites are cracking (Verdoliva et al., 2019), acylation (Smail et al., 2019), esterification (Gomes et al., 2019), ketonization (Yu et al., 2021), alkylation (Huseynova et al., 2022), etc..

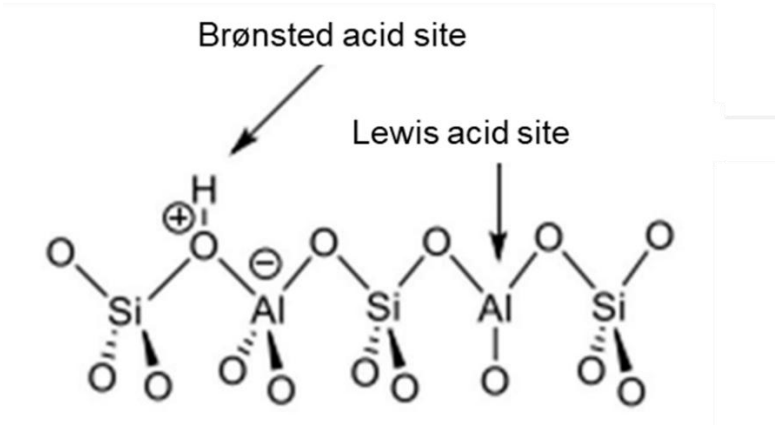

Figure 2.6 Brønsted and Lewis acid sites in zeolites (Orazbayev et al., 2020)

2.4.3 Zeolites as adsorbents

The process in which an atom or molecule of a gas or liquid is adhered on solid surface is called adsorption. A gaseous or liquid mixture can be separated using this process, which depends on the affinity of the atoms or molecules (adsorbate) to the solid surface (adsorbent). The surface area, pore size, chemical composition and hydrophilicity of zeolites can affect the adsorption process (Wang et al., 2019). Hence, these features make zeolites extremely valuable and useful since the surface properties of zeolites can be tuned to suit the specific adsorption process for separation (Baile et al., 2019). For example, modified zeolites for wastewater treatment are currently a hot topic due to their unique characteristics, good performance, and inexpensive cost (Shi et al., 2018).

2.5 Aluminophosphate and silicoaluminophosphate zeotypes

Aluminophosphates (AlPO) are a unique family of zeolite-like materials synthesized in 1982 (Yu & Xu, 2003). These materials have a neutral framework and are composed of AlO_4^- and PO_4^+ tetrahedra units that are strictly alternated through corner sharing. Owing to the alternate arrangement of AlO_4^- and PO_4^+ PBUs within the microporous aluminophosphate framework, this family of structures is acknowledged

as zeotype materials by the International Zeolite Association (IZA) (Baerlocher & McCusker, 2017). Some AlPO materials are shown in Figure 2.7.

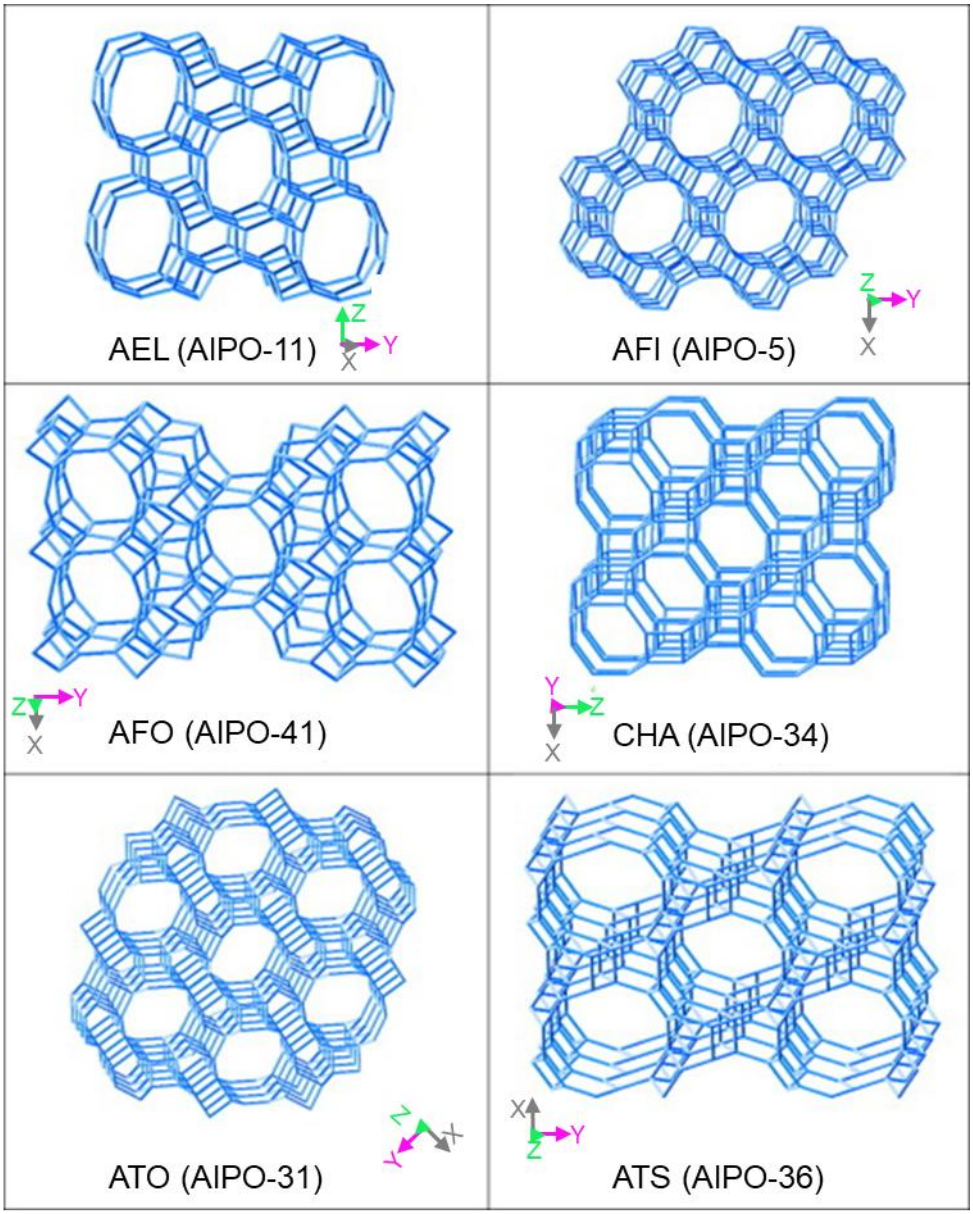

Figure 2.7 Some AlPO materials with three topological codes (IZA, 2024)

In AlPO, the framework is neutral due to the alternate arrangement of AlO_4^- and PO_4^+ PBUs. However, replacing one P atom with one Si atom will cause the framework to become negatively charged silicoaluminophosphates (SAPO) whereby the anionic surface is neutralized by a counter-cation, *viz.* H^+. So far, 41 types of SAPO have been made known and synthesized (Figure 2.8) (Baerlocher & McCusker, 2017). Some

examples of SAPO materials are SAPO-5 (AFI), SAPO-41 (AFO), SAPO-46 (AFX), SAPO-11 (AEL), SAPO-18 (AEI) and SAPO-34 (CHA).

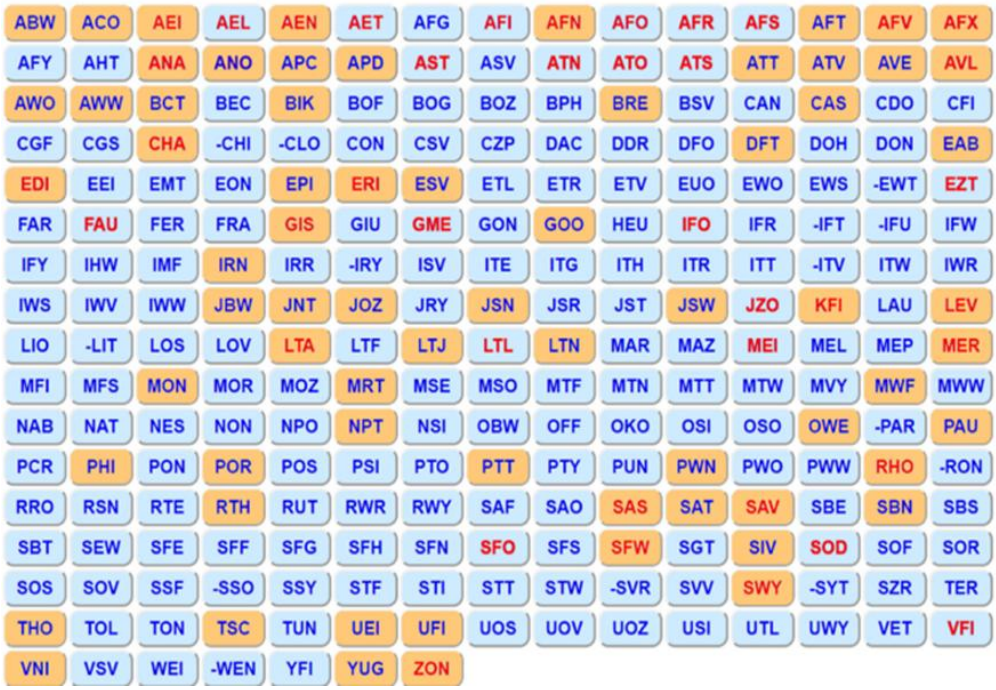

Figure 2.8 Topological codes of zeolite materials. The small-pore zeolites are marked with orange background and SAPOs are marked with red letters (Su et al., 2023)

2.5.1 SAPO-34

SAPO-34 is the most studied SAPO zeolite. The structure of SAPO-34 has a three-dimensional (3D) eight-membered ring (8MR) channel with an open size of 3.8 Å and a CHA topology. SAPO-34 is widely used for light gas separation due to its uniform, small pore size and high thermochemical stability. The combination of these characteristics, along with its tendency to selectively adsorb certain gases, has generated growing interest in the application of SAPO-34 membranes for gas separation (Xu et al., 2021). SAPO-34 can be synthesized using numerous organic structures directing agents (OSDAs), such as morpholine, diethylamine, dipropylamine, trimethylamine, tetraethylammonium hydroxide and trimethylamine (Doan et al., 2019).

The selection of OSDAs plays a crucial role in the synthesis of SAPO-34. This is because the nucleation and crystallization rates are greatly influenced by the type of OSDAs used since this species takes part actively in interacting with inorganic precursor species. As a result, the selection of templates has a direct impact on the crystal morphology of SAPO-34. For example, Liu et al. (2012) discovered that SAPO-34 zeolite, when templated with morpholine, had a size of roughly 10 μm. However, the crystal zeolite of SAPO-34 was reduced to about 2 μm when templated with triethylamine. In addition, an increase of template content leads to the generation of large amount of nuclei in the precursor medium, resulting in the formation of SAPO-34 with reduced crystal sizes (Wang et al., 2016).

In addition, the concentration of OSDAs has a significant effect on the crystal morphology of SAPO-34. Lee et al. (2007) discovered that by increasing the concentration of tetraethylammonium hydroxide (TEAOH) in the precursor solution, the shape of SAPO-34 crystals changes from rhombohedral to spherical aggregates, while the crystal size decreases from approximately 5−20 μm to submicrons of around 1 μm. Furthermore, Ye et al. (2011) found that reducing the TEAOH content increases the diameter of cubical SAPO-34 crystals. In addition, the utilization of mixed templates has been known to result in the formation of smaller SAPO-34 crystals compared to those synthesized using a single template (Wang et al., 2012).

2.5.2 SAPO-5

SAPO-5 is a zeotype material with an AFI topology. The AFI framework is made up of a one-dimensional (1D) channel system and a 12MR pore opening (7.3 Å) (Figure 2.9) (Meng & Xiao, 2014). SAPO-5 exhibits a large pore structure and offers mild acidity. These characteristics make SAPO-5 a promising material for catalytic applications (Li & Yu, 2021).

SAPO-5 molecular sieves can be synthesized using various organic templates (Kumar et al., 2005). However, the selection of template and its concentration during the synthesis can affect the physicochemical properties of SAPO-5 and other crystalline phases. SAPO-5 can be synthesized using more than 25 templates (Hu et al., 2010), including tetraethylammonium hydroxide (TEAOH), dipropylamine (DPA), diethylamine (DEA), morpholine and triethylamine (TEA). Among these, TEAOH is the most frequently employed template. Figure 2.10 illustrates some SDAs used to synthesize SAPO-5.

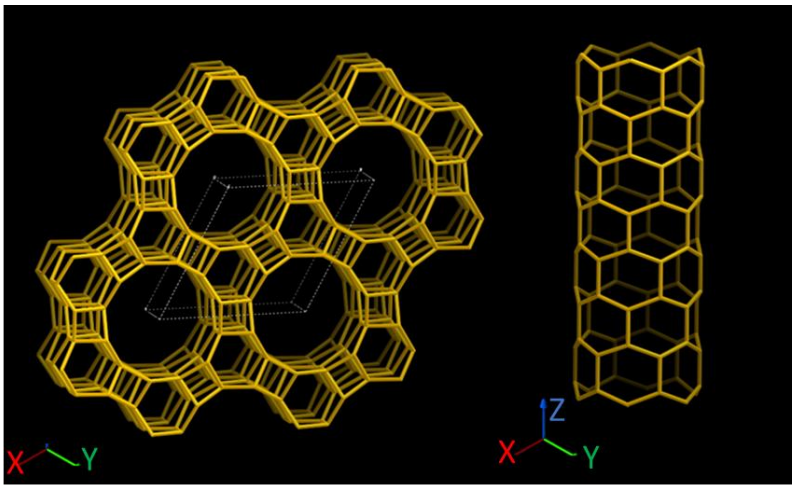

Figure 2.9 The AFI framework of SAPO-5 made up of 4, 6 and 12 rings (Baerlocher & McCusker, 2017)

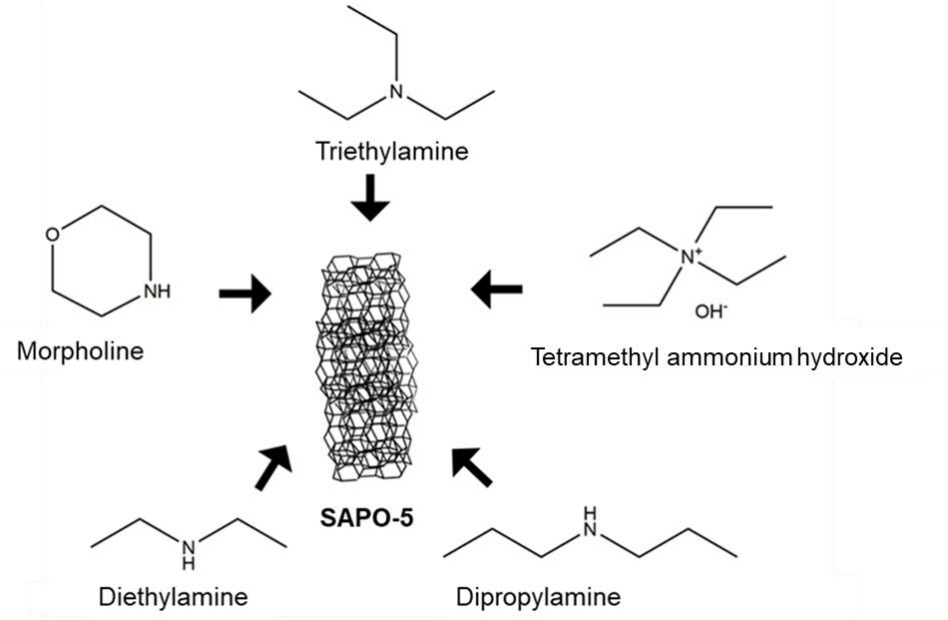

Figure 2.10 Some organic SDAs used to synthesize SAPO-5

The morphology and size of SAPO-5 crystals are significantly affected by the SDAs used. These morphological characteristics are crucial in catalytic reactions as they influence the diffusion pathlengths (Ahmad et al., 2020). SAPO-5 crystals often exhibit hexagonal shape. Numerous studies have demonstrated the potential to modify the morphology of SAPO-5 into various shapes by utilizing different SDAs. For example, SAPO-5 with hexagonal prism (Ahmed & Sakthivel, 2019), plate-like (Chen et al., 2015) and hexagonal rod-like (Utchariyajit & Wongkasemjit, 2010) morphologies can be produced utilizing triethylamine, tetraethylammonium bromide, and tripropylamine templates either through hydrothermal or microwave heating methods.

Additionally, the morphology of SAPO-5 is sensitive to the synthesis conditions since it largely depends on various reaction conditions like type and concentration of reactants, temperature, time, pressure, pH, type of SDA, aging, mixing nature and sequence (Askari et al., 2016). Figure 2.11 displays SAPO-5 crystals with various morphologies, which were obtained through utilizing different starting materials or pH levels.

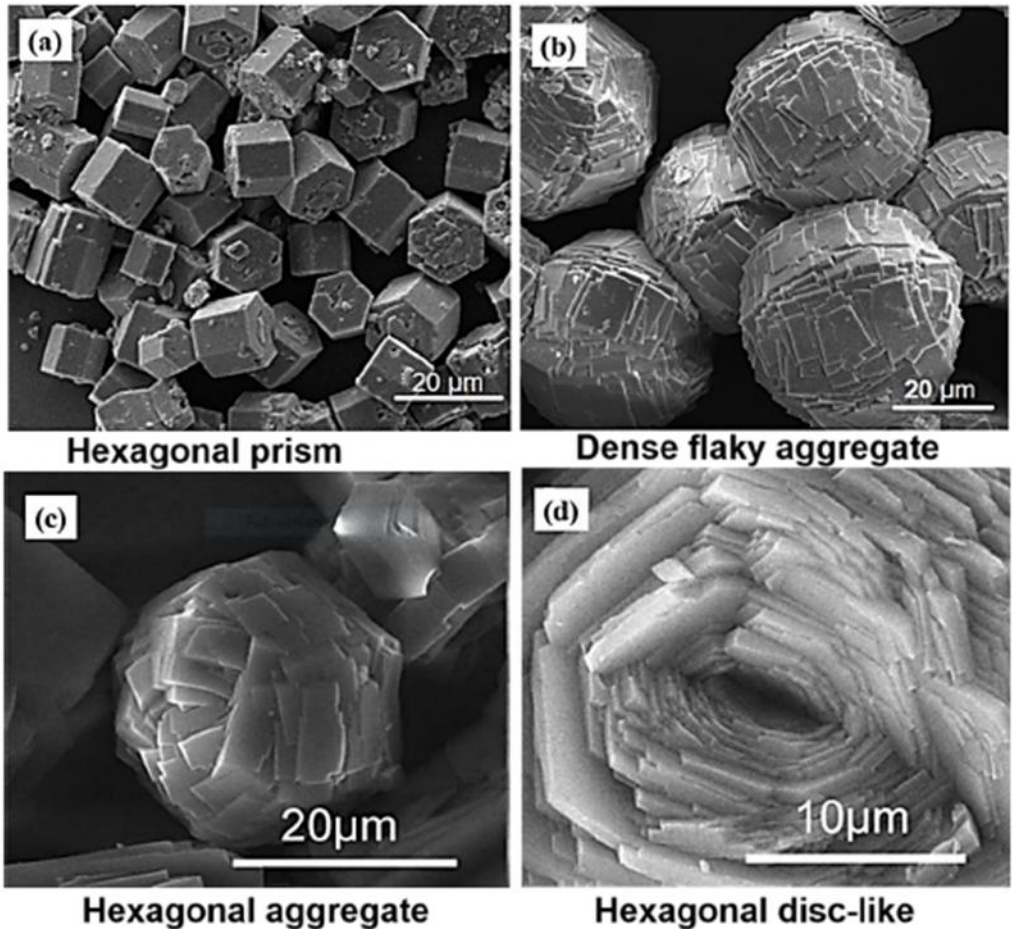

Figure 2.11 SAPO-5 crystals synthesized using different Al sources: (a) aluminum isopropoxide and (b) pseudo boehmite (Geng et al., 2018), and those synthesized at different pH using aluminum isopropoxide as Al source: (c) pH 9 and (d) pH 7 (Li et al., 2012)

Besides hydrothermal method, the synthesis of SAPO-5 using microwave-assisted hydrothermal technique is also reported. Zhao et al. (2015) reported the synthesis of SAPO-5 molecular sieve using microwave-assisted ionothermal method in a eutectic mixture solvent. Their findings demonstrate that the mesopore volume in SAPO-5 can be effectively tuned by adjusting the degree of supersaturation, besides selecting different types of mineralizers, or partially substituting succinic acid with sebacic acid. The study found that a low degree of supersaturation, along with the use of ammonium fluoride as a mineralizer, increases the mesopore volume in SAPO-5. Additionally, the introduction of sebacic acid can develop a three-level hierarchical

structure within the material, which is beneficial for catalytic alkylation of benzene with benzyl alcohol.

2.5.3 SAPO-11

SAPO-11 is a zeolite-like microporous solid having AEL topology. It has pores of different sizes made up of 4, 6 and 10 rings. The SAPO-11 has a unidimensional structure, mild acidity and elliptical 10-membered pore opening (0.4 × 0.65 nm^2) enabling molecular sieve action (Figure 2.12). Such properties are appeciated in applications needed for molecular shape discrimination.

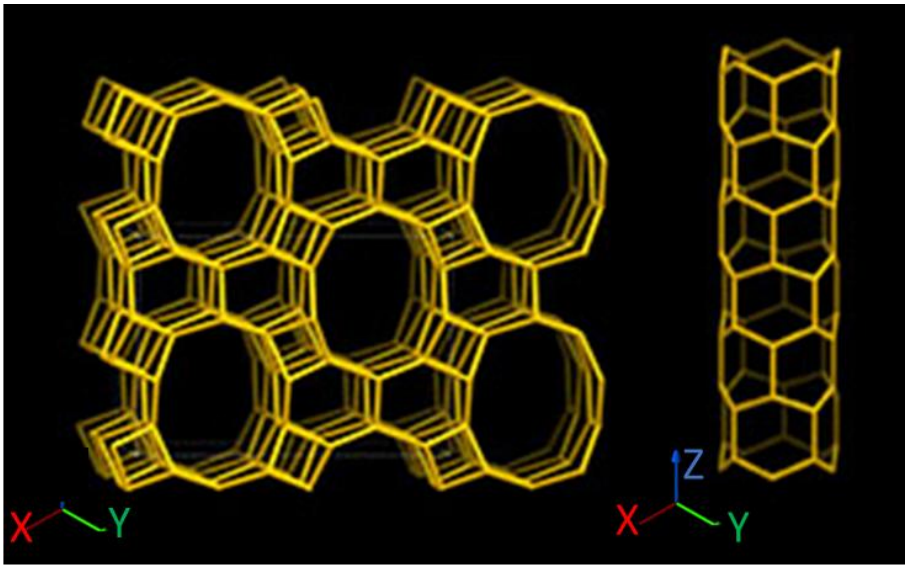

Figure 2.12 The AEL framework of SAPO-11 made up of 4, 6 and 10 rings (Baerlocher & McCusker, 2017)

Recently, Yang et al. (2019) synthesized SAPO-11 using two distinct templates, namely di-n-butylamine (DBA) and di-n-propylamine (DPA). The SAPO-11 synthesized with DBA exhibited significant difference in morphology and lower amount of Brønsted acid sites when compared to the SAPO-11 synthesized with DPA. The SAPO-11 samples were impregnated with Pd as bifunctional catalysts for n-decane hydroisomerization to branched decanes. The results showed that Pd/SAPO-11 prepared with DBA has better catalytic performance and stability than Pd/SAPO-11

prepared with DPA due to the higher dispersion of Pd metal particles on surface and fewer blockages of micropore openings.

The concentration of template solution has an impact on the crystallinity and acidity of SAPO-11. This was proven by Liu et al. (2008) where SAPO-11 was prepared using a combination of DPA and di-iso-propylamine (DIPA) as templates. They observed that by modifying the pH of precursor gels, the mechanism of silicon substitution can be altered, which in turn affecting the acidity of zeolites. It is also shown that the SAPO-11 synthesized using large amount of templates showed better catalytic activity in hydroisomerization of n-tetradecane as compared to those prepared using low amount of templates, and this is due to its high crystallinity that contributes to high surface acidity. Furthermore, the SAPO-11 prepared with a mixed template of DPA and DIPA showed no phase impurities compared to that synthesized with single template.

2.6 Mechanism of Si insertion

The replacement of either P or Al, or both, with silicon in AlPO results in the formation of the SAPO zeotypes framework through isomorphous substitution. There are three hypothesized substitution mechanisms (SM) for incorporating Si into the AlPO framework. These mechanisms are substituting Si for Al (SM1), substituting Si for P (SM2), and substituting two Si atoms for a pair of Al and P (SM3) which are shown in Figure 2.13 (Yang et al., 2020).

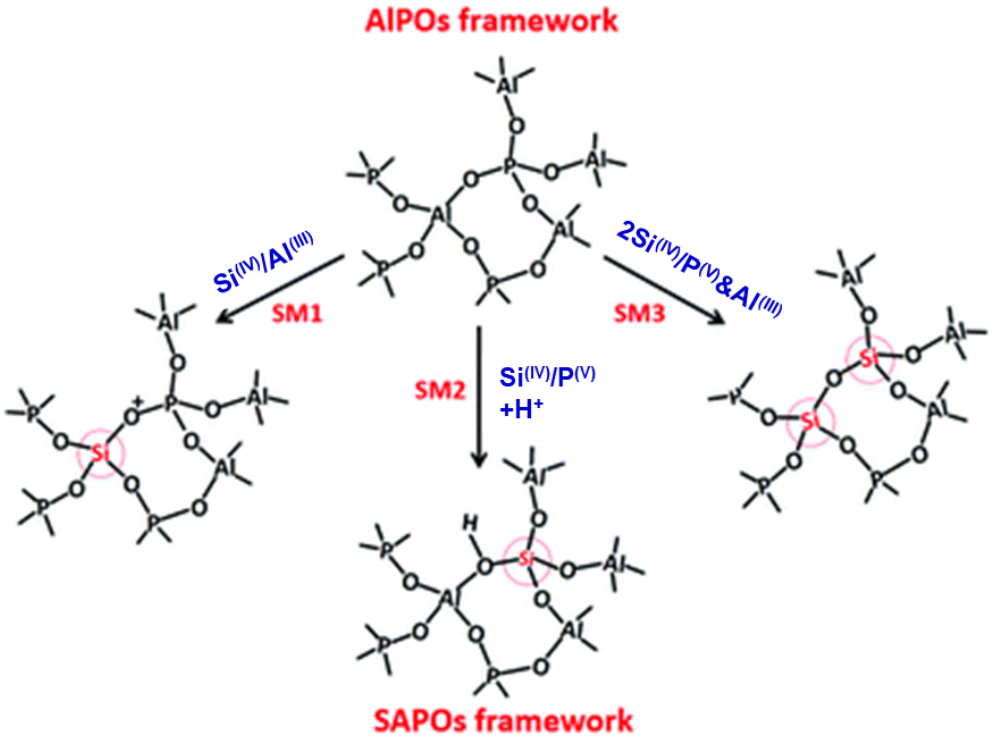

Figure 2.13 Three substitution mechanisms of Si atom into an AlPO framework (Paul et al., 2018)

The replacement of Al with Si (SM1) results in the formation of P-O-Si bonds which is thermodynamically unfavorable (Liu et al., 2020). Usually, the isomorphous substitution of Si occurs by a combination of SM2 and SM3. Replacing P with Si (SM2) in the neutral AlPO framework results in a net negative charge on the SAPO zeotype framework. This charge leads to the creation of Brønsted acid sites and the ability of SAPO materials to exchange ions. In addition, the replacement of a pair of P and Al with two Si atoms results in the formation of unstable Si-O-P bonds *via* the SM3 mechanism. Therefore, the SM3 mechanism is frequently followed by the SM2 mechanism, in which the immediate neighbors of Si atoms are either other Si atoms or Al atoms. The process produces islands composed primarily of Si-O-Si and Si-O-Al connections.

Meanwhile, the utilization of organic SDAs during the synthesis of SAPO zeotype materials has an impact on the incorporation of Si. Besides serving as template, the organic SDAs with cation charge are also used to compensate the charges by limiting the surface charge introduced during the Si substitution (Pastore et al., 2005).

2.7 Crystallization models of SAPO zeolites

Zeolites are normally synthesized in a batch system, where solutions containing aluminate, phosphate and silicate are blended together, forming a precursor mixture in the form of a gel or suspension. The appearance of precursor mixture can vary significantly, ranging from clear colloidal suspensions to opaque gel-like pastes, depending on the starting sources used and the mixing protocols (Figure 2.14). The suspensions composed of silicate and alumina derived from different sources have the ability to dissolve either fully or partially, leading to the formation of mixtures with diverse visual characteristics (Grand et al., 2016).

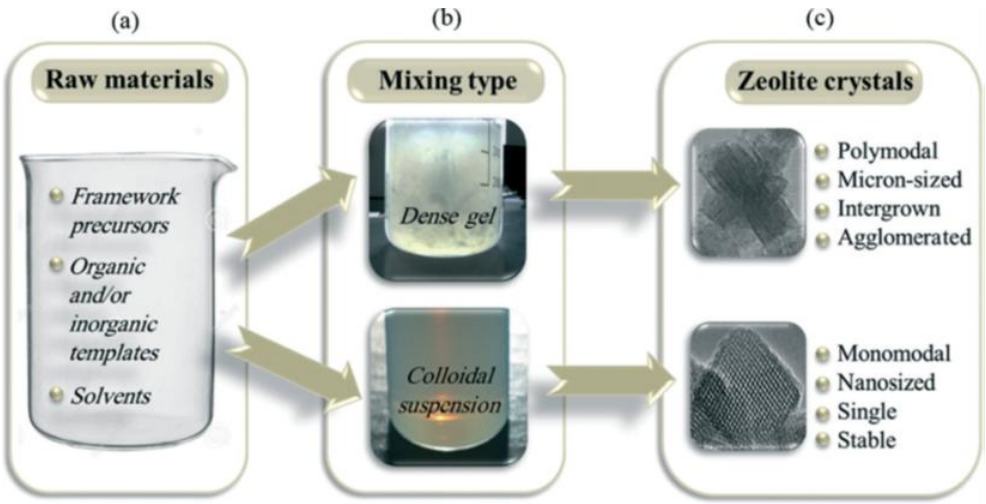

Figure 2.14 Zeolite synthesis: (a) selection of raw materials, (b) preparation of dense gel and colloidal suspensions determined by the type of raw materials and conditions of preparation, and (c) crystallization of zeolites from gels and suspensions with the corresponding properties

After preparation of hydrogels, the next process involves oligomerization of Si, Al and P inorganic monomers (primary building units), dimers and trimers to form more reactive amorphous intermediates. During this stage the organic templates start to interact with the oligomers by counter balancing the anionic inorganic intermediates. The oligomers further react with each other producing longer SAPO polymeric chain where the second building units start to form. At this stage, nucleation takes place when very tiny zeolite particles (<5 nm) are formed.

Discrete zeolite nanoparticles of silicalite-1 zeolite with sizes ranging from 1 to 6 nm have been reported by Fan et al. (2007). It is reported that the sub-nanocrystals of approximately 4.5 nm in diameter play a critical role during the nucleation process, whereby it undergoes evolution through various intermediate stages before evolving into fully formed zeolite crystals. In a related study, Fedeyko et al. (2004) describe these nanoparticles as having a core-shell structure, with a silica core surrounded by an organic shell, composed of structure-directing agents (or organic templates). The particle size remains consistent at around 4.5 nm, with pH and electrostatic forces significantly influencing their stability and growth.

The next step after nucleation is crystal growth where the nucleation sites will consume nutrients from mother liquor, leading to the transformation of amorphous entities to crystalline body. The zeolite nanocrystals are becoming bigger until all amorphous nutrients are consumed. In this stage, the thermodynamical equilibrium is achieved. Since the zeolite synthesis system is metastable, further supplying energy *via* heating to the synthesis system will lead to phase transformation (also called Ostwald ripening) where it is always experienced by large-pore zeolites due to their less thermodynamical stability, forming less pore-opening zeolites (more thermodynamic stable) (Deneyer et al., 2020).

2.8 Synthesis of SAPO zeolites

2.8.1 Hydrothermal method

The term "hydrothermal" was first coined in the field of geology in the mid-19th century (Bougault et al., 2019). The hydrothermal approach involves utilizing an aqueous solution as a reaction medium within a closed reaction vessel to generate high pressure reaction environment by the application of heat (Figure 2.15). Under this autogenic pressure condition (1 to 50 bar), the dissolution of reactants and subsequent crystallization of zeolite materials occurs. Figure 2.16 shows the general procedures involved in the hydrothermal synthesis of zeolites (Yang & Park, 2019).

During the hydrothermal synthesis of zeolites, the initial stage involves mixing of a water-based solution containing alumina, phosphate and silica in the presence of a SDA. Next, the hydrogel mixture is transferred into a Teflon container and sealed inside a stainless-steel autoclave. Afterwards, the hydrogel reaction is exposed to heat treatment in an oven for a duration ranging from a few hours to a few days, at temperatures ranging from 80 to 250 °C (Barrer, 1982). When conducting the synthesis at temperatures below 100 °C, it is possible to utilize polypropylene or Teflon plastic bottles since no pressure is produced below the boiling point of water. Following the hydrothermal procedure, the crystals undergo separation and are subsequently rinsed with distilled water to eliminate any unreacted chemicals. They are then subjected to oven drying and calcination to remove the organic SDAs.

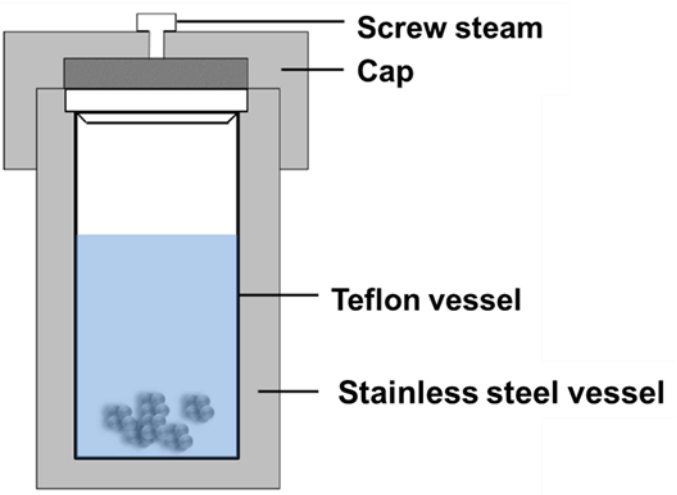

Figure 2.15 Schematic of hydrothermal synthesis method (Ijaola et al., 2020)

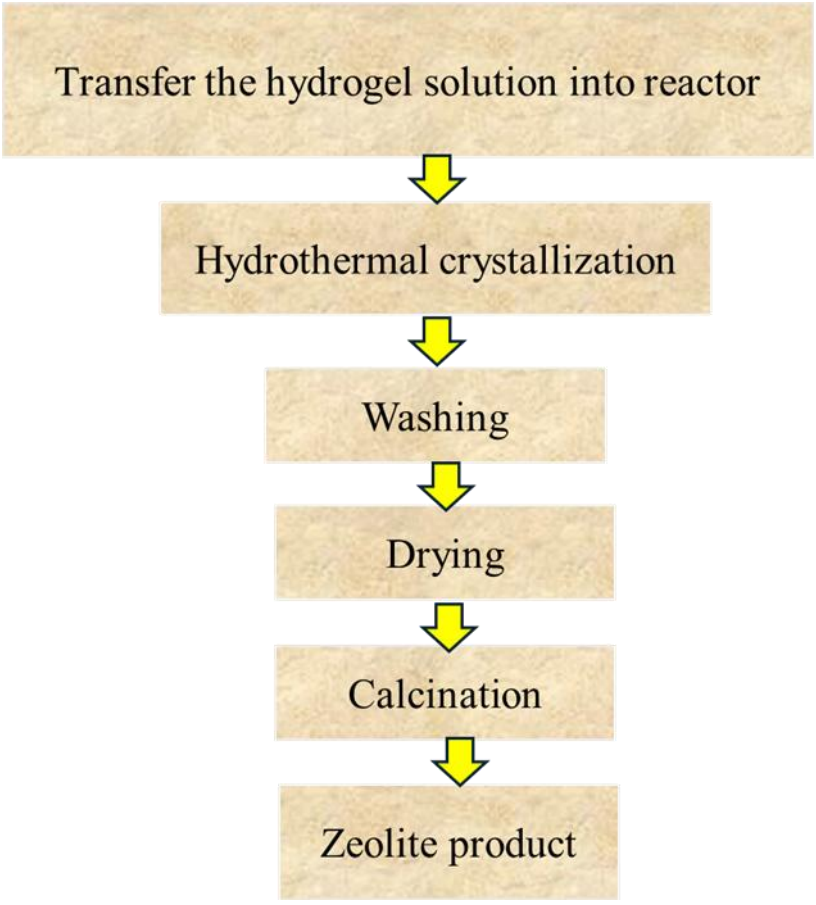

Figure 2.16 General steps of hydrothermal preparation of zeolites

2.8.2 Ionothermal method

The ionothermal synthesis method was initially proposed in 2004, where ionic liquids or deep eutectic solvents serve as solvents instead of water (Figure 2.17) (Cooper et al., 2004). Ionic liquids consist of an organic cation and an inorganic or organic anion. Due to their structural asymmetry, these ionic liquids typically remain in liquid state below 100 °C or even at ambient temperature. In most cases, imidazolium based ionic liquids are used in the ionothermal synthesis of zeolites due to their availability, straightforward synthesis method, and interesting physicochemical characteristics (Kumar et al., 2023). On the other hand, deep eutectic solvents are also a promising substitute for ionic liquids. They are prepared by combining two or more compounds having a melting point lower than the original compounds. These solvents exhibit similar characteristics to ionic liquids (Han et al., 2021).

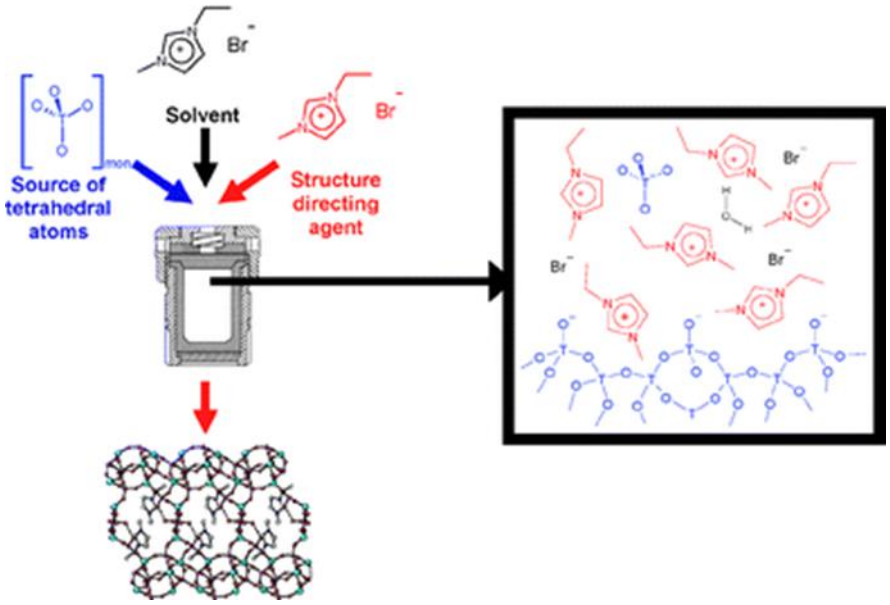

Figure 2.17 Schematic representations of the synthesis of a zeolite material under ionothermal conditions (Morris, 2009)

Due to their low volatility, ionic liquids can be used as solvents in ionothermal synthesis of zeolite materials even under ambient pressure. Furthermore, the organic cations present in ionic liquids can also serve as structure directing agents (SDAs)

because of their chemical similarity to the organic amines, which are commonly used as SDAs in hydrothermal synthesis. Hence, modifying the cation and anion pairing in ionic liquids or the composition of deep eutectic solvents can result in the formation of molecular sieves with distinct pore structures dan morphologies (Parnham et al., 2006). Table 2.2 shows the type of ionic liquids used for crystallizing SAPO zeolites under ionothermal conditions.

Table 2.2 Ionothermal synthesis of SAPO zeolites using various types of ionic liquids

Type of ionic liquid	Synthesis recipe	T (°C)	t (h)	Product	Ref.
1-Butyl-3-methyl-imidazolium bromide ([emim]Br)	$1Al_2O_3:1P_2O_5:0.6SiO_2:80$[emim]Br$:3H_2O$	180	10	SAPO-LTA	(Lin et al., 2019)
1-Ethyl-3-methyl imidazolium chloride ([EMI]Cl)	$1Al_2O_3:3P_2O_5:0.3SiO_2:39EMI:0.73H_2O$	150	72	SAPO-34	(Sánchez-Sánchez et al., 2017)
1-Methyl-3-ethylimidazolium bromide ([emim]Br)	$1Al_2O_3:3P_2O_5:64$[emim]Br$:0.8H_2O$	100	4	SAPO-11	(Cai et al., 2008)
Pentaerythritol/choline chloride eutectic mixture (EU)	$1Al_2O_3:1.5P_2O_5:0.4SiO_2$:54EU$:1H_2O$	180	1	SAPO-5	(Zhao et al., 2012)
1-Propylpyridinium hydroxide ([PPy]OH)	$1Al_2O_3:2.33P_2O_5:0.87SiO_2:6.68$[PPy]OH$:148H_2O$	200	21	SAPO-35	(Ma et al., 2022)

2.8.3 Microwave heating method

Microwave is an electromagnetic radiation falls within the wavelength range of 1 mm to 1 m (Figure 2.18). This corresponds to a frequency range of 300 MHz (λ = 1 m) to 300 GHz (λ = 1 mm). Microwave is widely utilized in commercial and military applications, particularly in cellular, internet, satellite communications and radar technologies. Additionally, they are employed in the food industry for heating and drying processes (Wojnarowicz et al., 2020).

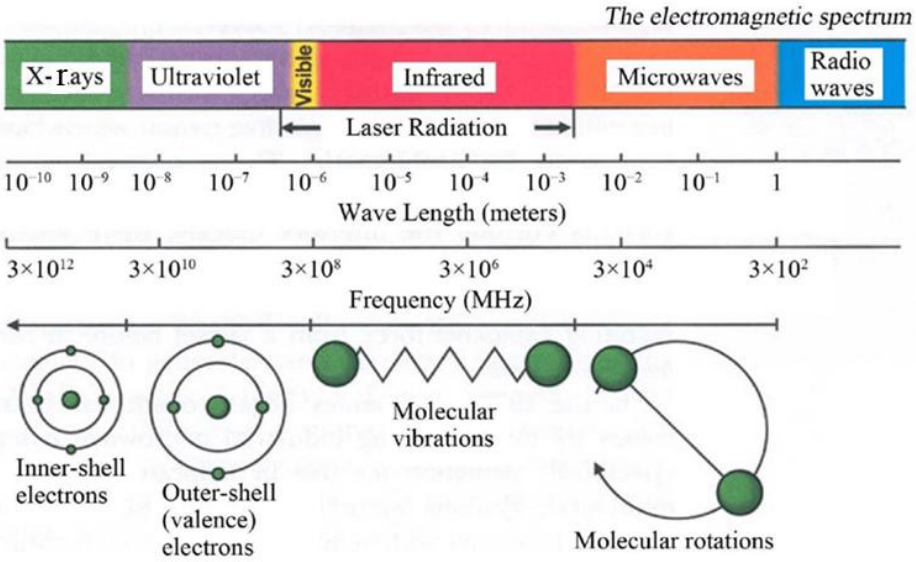

Figure 2.18 The electromagnetic spectrum showing characteristics of microwaves (Rana & Rana, 2014)

Microwave heating is a promising technique that can effeciently decrease the synthesis time while ensuring the heating uniformity, and improving the solubilization of precursors (Li & Yang, 2008). Unlike conventional convection heating, which transfers heat from an external source, microwave heating generates heat directly within the material. This occurs when microwave radiation interacts with polar molecules, causing them to oscillate rapidly, which in turn produces heat (Mishra et al., 2016). Microwave heating can be caused by the pertubation of electric component

of electromagnetic radiation through four mechanisms, namely dipolar polarization, ionic polarization, atomic polarization, and surface polarization (Falciglia et al., 2018).

In zeolite synthesis, microwave heating is appreciated by its fast heating rate and high homogeneity of crystal sizes (Ren et al., 2022). Besides that, the morphology and crystal size of zeolites can be manipulated by using microwave heating method thanks to its unique heating mechanism (Zeng et al., 2021). Numerous papers have been published on the microwave-assisted crystallization of SAPO zeolites. For instance, Yang et al. (2012) synthesized a micro/mesoporous SAPO-34 using microwave heating. The prepared zeolite had a reduced particle size and a unique pore shape that combined both micropores and mesopores. The microwave-synthesized hierarchical SAPO-34 performed more superior than the standard SAPO-34 in the methanol to olefins (MTO) reaction with reduced rates of catalytic deactivation thanks to its mesoporosity and smaller crystal size.

Utchariyajit and Wongkasemjit (2010) used alumatrane and silatrane to synthesize SAPO-5 under microwave conditions. They studied and optimized the reaction conditions, *viz.* aging time, reaction time and temperature. The study found that the SAPO-5 zeotype exhibited an AFI-type structure with a hexagonal outer surface morphology and an average pore diameter of 2–5 nm. When the reaction time was increased to 1 h, SAPO-5 crystals were formed. Extending the reaction time beyond 1 h led to secondary growth of SAPO-5 crystals, resulting in non-uniformity. Therefore, a 1-hour reaction time was selected for further investigations. In addition, the reaction gels could accommodate up to a 0.8 mol ratio of SiO_2 to Al_2O_3, resulting in highly crystalline SAPO-5.

Gharibeh and co-workers (2008) studied the impact of microwave heating on the nucleation and growth of SAPO-11 zeolite. It was shown that the time required to reach a reaction temperature of 175 °C using microwave heating is only 1 min, but it took 90 min with traditional hydrothermal heating. As a result, the accelerated heating ramp leads to an increase in the rates of nucleation and crystallization. In addition, the use of microwave heating leads to the formation of crystals with uniform shape and narrower particle size distribution. The utilization of microwave heating in this work provides substantial energy efficiency, while its high-speed synthesis also enables the possibility of continuous processing, with a synthesis time of just a few minutes instead of hours.

2.8.4 Interzeolite conversion (IZC)

The interzeolite conversion (IZC) is a method of synthesizing zeolites by using a crystalline zeolite source (as parent) to facilitate the crystallization of another zeolite (as daughter) (Figure 2.19) (Dusselier & Davis, 2018). Usually, this process is carried out using a traditional hydrothermal method in a batch mode (Deneyer et al., 2020). IZC provides exceptional control over the factors influencing the zeolite kinetics, besides allowing the formation of zeolites with distinct properties as compared to the hydrothermal ones. This is made possible by adjusting the input liquid and crystallization conditions.

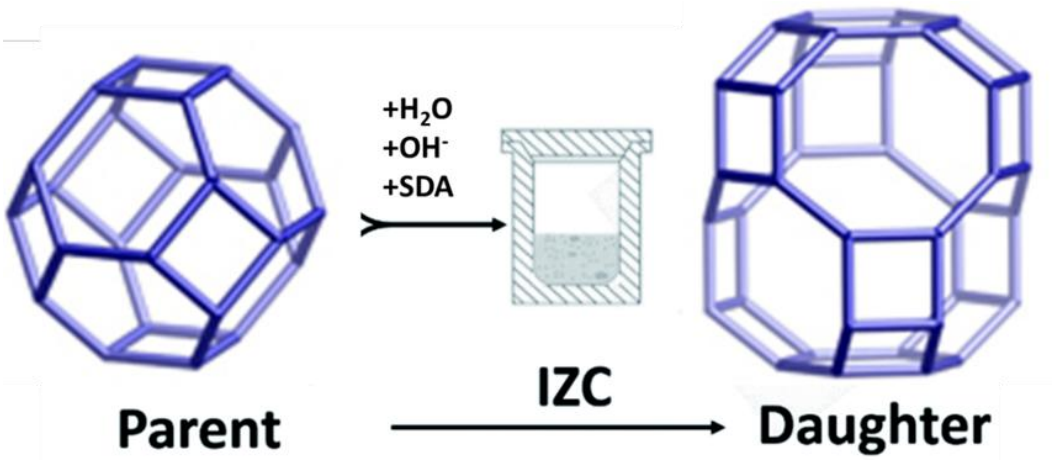

Figure 2.19 Schematic representation of interzeolite conversion (IZC) from a parent zeolite (FAU) to daughter zeolite (CHA) occurring in an autoclave containing water, hydroxide mineralizer and organic structure-directing agent (SDA) (Ijaola et al., 2020)

Ge et al. (2022) synthesized SAPO-11 from AlPO-8 *via* IZC method by controlling its kinetics and topology. By employing various characterization approaches, the formation mechanism of SAPO-11 is elucidated. The crucial factor for achieving success is that AlPO-8, *viz.* a less metastable phase tends to transform into a more metastable SAPO-11 phase with better diffusion and acid properties.

Itakura et al. (2011) investigated the transformation of SAPO-37 zeolite into SAPO-34 zeolite under different synthesis conditions through interzeolite conversion using benzyltrimethylammonium hydroxide as a structure directing agent. The procedure formed pure and highly crystalline SAPO-34 with a diverse range of Si/Al ratios. By introducing seed crystals and Na^+ cations, they also found that the crystallization time and crystal size were dramatically decreased.

Umehara et al. (2013) utilized the same technique to produce a SAPO zeolite with LTL structure from SAPO-37 (FAU topology) in the presence of KOH and tetramethylammonium hydroxide (TMAOH) at (170°C, 24 h). They found that using FAU zeolite as a starting material is more efficient than using amorphous hydrogel for crystallizing LTL-SAPO zeolite. The successful synthesis of LTL-SAPO zeolite could

be attributed to the release of double-6-ring (D6R) secondary building units from SAPO-37 into the precursor and functioned as the building units for LTL-SAPO, which in turn promotes nucleation and crystal growth of the zeolite.

2.8.5 Steam-assisted crystallization

The steam-assisted conversion (SAC) method is a kind of seeding technique to crystallize zeolites with high reproducibility (Figure 2.20). In this method, only water undergoes vaporization while the structure directing agent is mixed within the semi-solid gel. The crystallization then occurs in the amorphous gel under steaming. This method offers several advantages over conventional hydrothermal method. First, the crystallization process is much faster. Second, the amount of SDAs required for crystallization is lesser. Furthermore, this method only generates water vapor as byproduct (Feliczak-Guzik, 2018).

Liu and his colleagues (2014) synthesized superfine SAPO-11 zeolite using this technique in the presence of fluoride ions. They found that the SAPO-11 synthesized without fluoride ions in the initial gel has rod-shape morphology with a particle size distribution ranging from 1.5−4.6 μm. However, introducing fluoride ions produces superfine and uniform SAPO-11 crystals with a particle size of 0.4−1.0 μm.

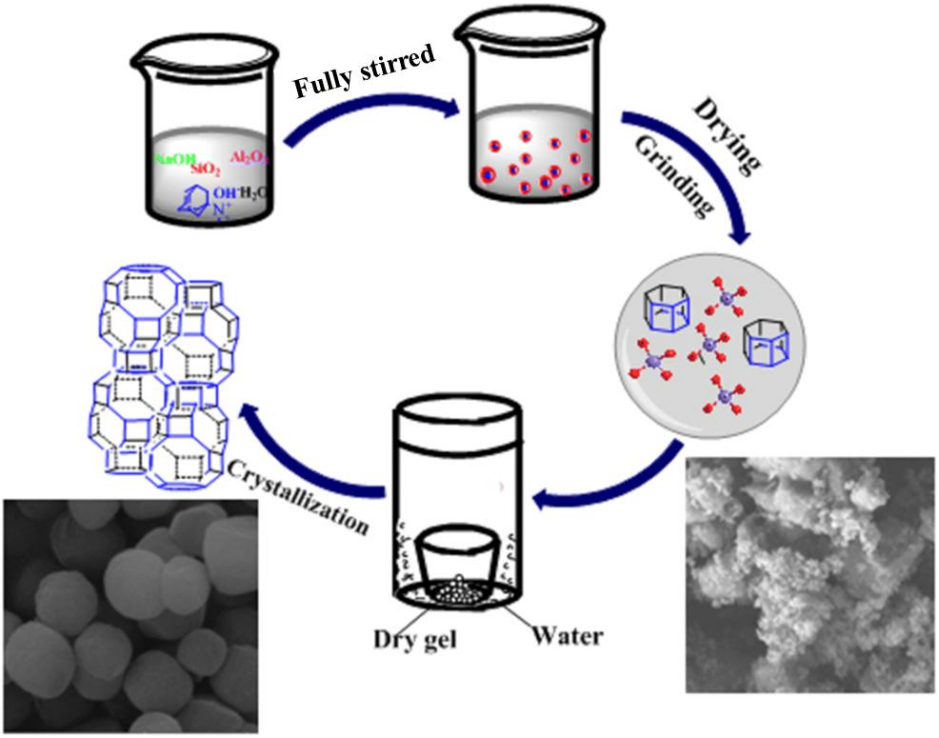

Figure 2.20 Steam-assisted crystallization of high silica SSZ-13 zeolite (Li et al., 2019)

Di et al. (2017) used the same technique to synthesize SAPO-34 using triethylamine template. At 170 °C for 48 h, plate-like nanocrystals of SAPO-34 were successfully prepared after adding 30 wt% of SAPO-34 seeds. Nevertheless, SAPO-34 crystals with a size range of 5–10 µm were formed when seeds were not present.

In addition, tetraethylammonium hydroxide (TEAOH) was also used as the SDA in the formation of nanosized SAPO-34 under SAC conditions (Hirota et al., 2010; Shamanaeva et al., 2022). In the study, the effects of type of alumina and duration of SAC (5 and 24 h) on crystal size, textural and acidic properties were studied. The SAPO-34 nanocrystals produced had a large micropore volume (0.22–0.24 $cm^3\ g^{-1}$) and high specific surface area (651–695 $m^2\ g^{-1}$). Extending the crystallization period to 24 h resulted in the formation of a SAPO-18 structure, although the micropore and mesopore volumes remained largely unchanged.

2.8.6 Solvent-free synthesis

The solvent-free technique was developed to tackle the issue of excessive water consumption during the zeolite crystallization process. The success of solvent-free method suggests that the crystallization of zeolite does not require a solvent (Mei et al., 2021).

Xiao et al. (2012) successfully synthesized several industrially significant zeolites using this method, including MFI, MOR, FAU, SOD and BEA typed zeolites. In this method, zeolite seeds can be used to replace organic SDA to crystallize zeolites without the need of water solvent (Figure 2.21). This solvent-free method hence eliminates the use of costly and harmful organic SDAs and excessive solvents, which in turn reducing the expenses of zeolite production besides minimizing the environmental pollution caused by organic templates and wastewater discharge.

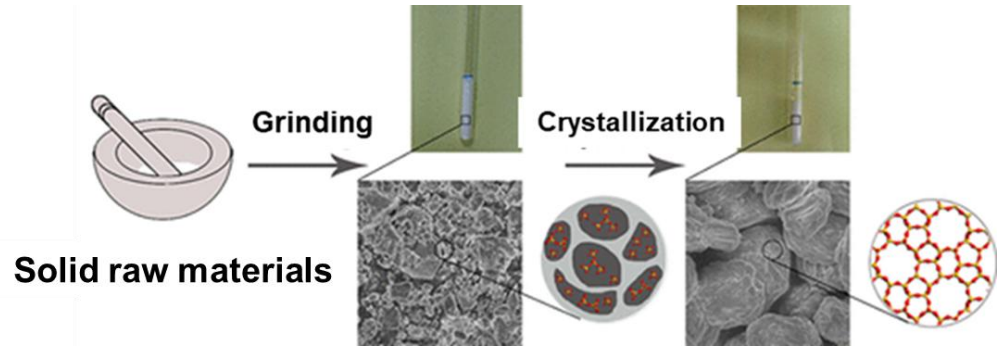

Figure 2.21 Solvent-free synthesis of zeolite (Wu et al., 2018)

Chen et al. (2015) synthesized SAPO-5 crystals in the presence of cetyltrimethylammonium bromide (CTAB) surfactant without solvent. The XRD and SEM analyses indicated that the samples exhibited a high degree of crystallinity and a well-regulated plate-like structure, showing the role of surfactant in manipulating the zeolite morphology.

Du et al. (2018) utilized the solvent-free technique to synthesize SAPO-11 zeolite. They observed that an addition of CTAB has a notable impact on the

development of uniform spherical aggregates during the synthesis process. In addition, hierarchical porous structure in SAPO-11 was also formed whereby this secondary porosity is appreciated in catalytic n-hexadecane hydroisomerization reaction, giving >96% conversion and 80% isomer yield which is higher than the normal SAPO-11.

2.8.7 Mechanochemical synthesis (MCS)

Mechanochemistry, which refers to the use of mechanical force to enable chemical synthesis, has long been recognized in the fields of metallurgy and mineral processing (Baláž, 2021). However, it has undergone a restoration period in recent decades in the areas of catalysis, inorganic chemistry and pharmaceutical synthesis (Takacs, 2013). The fundamental concept underlying this synthesis technique is to enhance chemical reactions by mechanically milling or grinding the initial substances of solid with minimal quantity of solvents or even in the absence of solvents (Tanaka, 2020). Figure 2.22 summarizes the synthesis of zeolites from fly ash by using mechanochemical synthesis method.

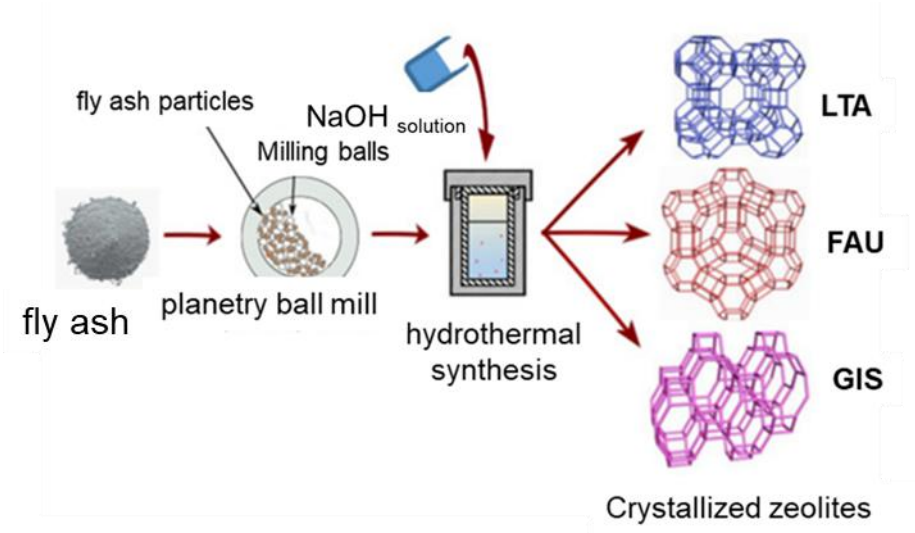

Figure 2.22 Some zeolite products formed by mechanochemical synthesis method from fly ash (Grabias-Blicharz et al., 2022)

Gordina et al. (2003) used MCS method to synthesize NaA zeolite using aluminum and sodium hydroxides, silica gel and sodium silicate. By using this method, the activation stage for zeolites during synthesis can be eliminated, thereby enhancing their reactivity. The study found that the synthesized NaA zeolite exhibited structural defects, as indicated by its lower crystallinity and lower thermal stability compared to the commercial zeolite NaA.

Zhang et al. (2022) documented the mechanical transformation of micrometer-sized SAPO-34 into nanometer-sized SAPO-34 particles using the straightforward bead-milling process. By adding poly(diallyldimethylammonium chloride) as a porogen during recrystallization, the formation of secondary crystals is surpressed. At the same time, it allows the control of crystallinity, acidity and porosity, leading to the formation of small and well defined crystallites (100−200 nm) that can enhance the mass transportation. The work also reveals that the SAPO-34 nanocatalyst synthesized using porogen-assisted bead milling recrystallization method exhibits superior performance in methanol to olefins (MTO) reaction compared to both the original SAPO-34 catalyst and the SAPO-34 catalyst recrystallized without porogen. In addition, a longer catalyst lifespan and a higher selectivity towards propylene are also observed.

2.9 Chemical reactants and synthesis conditions of SAPO zeolites

2.9.1 Aluminum source

Zeolites can be synthesized from many sources whereby each source has distinct chemical composition, reactivity and physicochemical properties (Kuwahara et al., 2010). Aluminum is one of the important components in zeolite framework as it imparts a negative charge to the zeolite framework (Fletcher, 2019). The presence of aluminum also affects the acidity of zeolites (Ravi et al., 2020). Typical aluminum

sources used for zeolite syntheses are aluminum hydroxide ($Al(OH)_3$), aluminum sulfate ($Al_2(SO_4)_3$) (Ates, 2019), sodium aluminate ($NaAlO_2$) (Krachuamram et al., 2021), alumina (Al_2O_3) (Klunk et al., 2020), aluminum nitrate ($Al(NO_3)_3$) (Abbasizadeh & Karimzadeh, 2018), and aluminum isopropoxide ($Al(OC_3H_7)_7$) (Bing et al., 2020).

Recently, SAPO-11 has been crystallized using various aluminum sources such as alumina (Walendziewski & Pniak, 2003), pseudoboehmite (Zhang et al., 2018), and aluminum hydroxide (Sánchez-Contador et al., 2018). These sources significantly affect the crystal size, pore distribution and acidity of SAPO-11. For instance, the choice of aluminum source can lead to variations in the uniformity and connectivity of the pore structure, which in turn influences the catalytic performance and stability of SAPO-11 zeolites. Additionally, the presence of different aluminum precursors also alters the rate of crystallization and the overall morphology of zeolite crystals (Silva et al., 2016).

Valizadeh and co-workers (2014) used aluminum isopropoxide to prepare SAPO-5, demonstrating it as an efficient aluminum source. Furthermore, pseudoboehmite has been utilized as a reactive aluminum source to synthesize hierarchical SAPO-5 (Ali et al., 2020). The effects of various aluminum sources on SAPO-5 zeolite synthesis have also been investigated (Kumar et al., 2005), whereby aluminum sulfate, sodium aluminate, aluminum oxide and pseudoboehmite were studied. The findings indicate that the type of aluminum source can lead to significant differences in the physical properties and catalytic behavior of SAPO-5. For instance, pseudoboehmite results in enhanced hierarchical structures, which improve the accessibility of active sites and the overall catalytic efficiency of the zeolite catalyst. In another study, aluminum sulfate and sodium aluminate are also being studied and

found that these aluminum sources can affect the acidity and thermal stability of SAPO-5, which affect the SAPO-5 performance in methanol to olefins (MTO) catalytic reaction (Yadav & Singh, 2021).

2.9.2 Phosphorus source

Phosphorus (P) is an essential component in SAPO zeolites, where the selection of the phosphorus source in SAPO synthesis can significantly impact their characteristics (Simancas et al., 2021). Typically, phosphorus sources are added in the form of acidic phosphorus compounds (e.g. H_3PO_4, H_3PO_3, etc.), which alter the pH of hydrogel, thereby influence the entire crystallization process and final properties of SAPO zeolites (Wang et al., 2014).

Guangyu et al. (2012) investigated the effect of H_3PO_4 content on the synthesis of SAPO-34 where diethylamine was used as a template. It was shown that an increase in P_2O_5 content leads to a noticeable decrease in pH values (acidity increased) both before and after crystallization. This decrease in pH indicates that high concentration of H_3PO_4 was unfavorable for SAPO-34 crystallization.

Similarly, Sedighi et al. (2014) examined the effects of P content and water levels in the starting gel on crystallinity, number of acid sites, and crystal size of SAPO-34. The findings showed that increasing the P_2O_5/Al_2O_3 molar ratio to 1 enhanced both crystallinity and crystal size, but also acidity. However, excessive P content in the initial gel reduced the crystallinity and surface smoothness, suggesting that increased P content can enhance crystallinity and crystal size, but there is a threshold beyond which these properties begin to deteriorate.

Recently, SAPO-11 has been synthesized using phosphorous acid (H_3PO_3) or a combination of H_3PO_3 and H_3PO_4, in the presence of a dipropylamine template (Ma et al., 2006). The study revealed that using these P sources and template could fine tune the pore structure and acidity of SAPO-11, leading to improved catalytic performance. Furthermore, a solvent-free synthesis of hierarchical SAPO-11 using dipropylamine phosphate ($DPA{\cdot}H_3PO_4$) as a phosphorus source has been reported, which eliminates the need for mesoporous organic templates (Sheng et al., 2020). This method hence results in an environmentally friendly synthesis process since no solvent is applied.

In another recent study, Zhao et al. (2022) successfully synthesized SAPO-34 nanosheets, which is different from the classical cubical SAPO-34 crystals, by using pyrophosphoric acid ($H_4P_2O_7$) as a new P source. The SAPO-34 nanosheets possess a shell that is rich in silica and a core that is rich in P, resulting in exceptional catalytic performance in the methanol to olefin process (MTO) (100%). Hence, the selection of P source is important in the synthesis of SAPO zeolites as it influences the structural, physical and catalytic properties of zeolites.

2.9.3 Sillicon source

Silicon (Si) is another important element in SAPO zeolite frameworks. When Si is introduced into AlPO structures, SAPO zeolites containing acidic sites are produced. Theoretically, an increase in Si incorporation in the framework leads to an increase in the number of acid sites. However, reducing the Si concentration during the crystallization process is advantageous for minimizing the formation of Si islands. Furthermore, the incorporation of Si is strongly influenced by the Si sources used. For instance, the SAPO zeolites synthesized using tetraethyl orthosilicate (TEOS) as the Si source exhibits better Si distribution compared to those synthesized using fumed

silica and colloidal silica (Roldán et al., 2007). Thus, when comparing the acidity of the SAPO samples, it is important to note that the distribution of Si in the framework is more significant than the amount of Si present for generating surface acidity (Yang et al., 2017).

Bértolo and colleagues (2017) investigated the effects of different Si sources, namely tetraethyl orthosilicate, Ludox AS-40, and Aerosil (A380), on the SAPO-11 synthesis. The results showed that the selection of Si source had a substantial impact on the textural characteristics and acidity of SAPO-11. Reactive sources such as tetraethyl orthosilicate and A380 resulted in SAPO-11 with a high concentration of Brønsted acid sites, while the less reactive Ludox AS-40 produced SAPO-11 with lower acidity.

Danilina and her colleagues (2011) explored the use of different Si sources, such as fumed silica, tetraethyl orthosilicate, Ludox AS-40 and sodium silicate, to synthesize hierarchical SAPO-5. They varied the Si source and its concentration, as well as the amount of ([3-(trimethoxysilyl)propyl]hexadecyl dimethylammonium chloride, *viz.* a mesopore-directing agent. The study found that the Si source significantly affected the hierarchical structure and acidity of SAPO-5. Specifically, tetraethyl orthosilicate and sodium silicate resulted in better mesopore formation and higher acidity compared to other Si sources. Additionally, the hierarchical SAPO-5 synthesized with tetraethyl orthosilicate exhibited superior performance in the alkylation of benzene and cyclohexylbenzene with benzyl alcohol, demonstrating its superior catalytic activity and selectivity.

2.9.4 Structure-directing agent (SDA)

Structure-directing agents (SDAs) or organic templates are crucial components in the synthesis of zeolites (Kerstens et al., 2020). These additives are sometimes essential for crystallizing unique zeolites, particularly pure silicalite, high silicate, or SAPO zeolites (Yu, 2007). An organic SDA aids in forming microporous zeolites by promoting their nucleation and crystallization rates. Conversely, organic compounds that cannot independently stimulate zeolite crystallization are called pore fillers (Sakai et al., 2022).

SDAs not only facilitate the formation of specific SAPO zeolite structures and serve as charge-balancing ions but also stabilize the zeolite pores through encapsulation. Initially, inorganic cations such as Na^{+}, Ca^{2+}, or K^{+} are used as inorganic SDAs in zeolite synthesis. However, the most notable advancement in zeolite research is the use of organic SDAs (OSDAs), primarily consisting of amines and quaternary ammonium cations (Gómez-Hortigüela & Bernardo-Maestro, 2018). In most cases, the OSDAs facilitate the formation of framework structures that mimic their own shapes (Rey et al., 2017). Linear OSDAs often promote one-dimensional (1D) crystalline structures, branched OSDAs facilitate two-dimensional (2D) and three-dimensional (3D) interconnected structures, and bulky OSDAs promote structures with cages and cavities (Kulprathipanja, 2010). Meanwhile, the reduced charge density of OSDAs compared to alkaline and alkaline earth cations allows the formation of frameworks with lower overall charge, enabling the production of zeolite materials with higher Si/Al ratios and stronger surface acidity (Zones, 2011).

In SAPO zeolites, the primary function of the template is to induce the molecular packing effect, where the template molecule is enclosed within the pore channel of zeolites to stabilize and form a certain pore structure. The non-bonding

interaction between the template and inorganic framework affects the replacement of Si within the framework, resulting in SAPO zeolites with varying acidities. Additionally, a mixed or dual templates can also be used to crystallize SAPO zeolites where the resulting crystals show different physicochemical properties (e.g. morphologies, porosity and acidity) from those prepared using single templates (Liu et al., 2008).

2.9.5 Water content

Water plays a crucial role in the zeolite synthesis, which significantly affects the crystallization process and properties of the materials. During the synthesis, water serves as a solvent for mixing of reagents. In addition, it allows the contact of reagents to enable chemical reactions by assisting in the breakdown of molecules through hydrolysis of Al–O, P–O and Si–O bonds besides helping in polycondensation and polymerization of TO_4 species (T = Si, Al or P) (Resasco et al., 2021).

Water is also important in nucleation process whereby it controls the supersaturation level of the precursor solution. As a result, it directly affects the physicochemical properties of final zeolite products (Boltz, 2014). Water also plays a role as a "catalyst" during the process of zeolite crystallization. It participates in the hydration of silica species and water is regenerated during the subsequent condensation of the hydrated silica species (Meng & Xiao, 2014). Hence, the participation of water in the zeolite synthesis goes beyond its function as a solvent; it actively influences the morphological structure and impacts the properties of final zeolite products (Stanciakova & Weckhuysen, 2021).

Dai et al. (2022) utilized a concentrated gel method to synthesize a series of SAPO-11 molecular sieves. The synthesis process involved pre-crystallizing the initial gel at 120 °C for 12 h, followed by crystallization at 190 °C for 24 h. The findings demonstrated that lowering the water content not only promoted the formation of more mesoporous structures within the SAPO-11 molecular sieve but also increased the overall acidity, particularly the concentration of medium and strong Brønsted acid sites.

2.9.6 Crystallization time and temperature

Heating time is one of the most important parameters in zeolite synthesis. By increasing the heating time, it allows the formation of zeolites crystals through conversion of amorphous solid into crystalline material (Tao et al., 2017). It is known that an optimal heating time is important in the production of highly pure zeolite crystals (Meldrum & O'Shaughnessy, 2020). This optimal time ensures that crystallization is essentially completed within the specified time frame. If not, Ostwald ripening will occur upon prolonging the crystallization time, which promotes phase transformation into more denser zeolites.

Meanwhile, the crystallization temperature is another crucial parameter where it provides necessary heat energy to the synthesis system to initiate condensation, polymerization, nucleation and crystallization processes. Generally, there is a specific temperature range where a zeolite is favorably formed, namely from 90−220 °C. As the temperature rises, the crystallization rate is enhanced, causing the formation of zeolites with high degree of crystallinity and larger crystals. When the temperature above the upper limit of the suitable range, an impurity phase, such as tridymite or crystobalite, tends to co-crystallize with the main zeolite phase (Shalmani et al., 2013).

Thus, the selection of proper crystallization temperature and duration is essential to ensure pure zeolite phase is produced.

2.10 Charactarization of zeolite

To better understand the properties, morphology, and structure of various SAPO zeolite samples, researchers have employed a range of spectroscopic and quantitative analytical techniques. This section outlines some of the most commonly used methods, such XRD, SEM, FTIR, NMR, TGA, and TPD-NH_3.

2.10.1 X-ray powder diffraction (XRD)

X-ray powder diffraction (XRD) is the most important characterization technique in zeolite research. It provides vital information that can be used to determine the purity, crystallinity, crystal size, orientation of a zeolite sample (Waseda et al., 2011). The basis of X-ray diffraction is the constructive interference of a crystalline sample with monochromatic X-rays. A cathode ray tube produces these X-rays, which are then collimated to concentrate them, filtered to produce monochromatic radiation, and directed towards the sample. A diffracted ray and constructive interference are produced when the incident rays interact with the sample. Subsequently, these diffracted X-rays are located, examined and tallied (Dowsett et al., 2021).

The International Zeolite Association (IZA) has compiled a database that lists out all the XRD patterns of zeolites discovered so far (Baerlocher & McCusker, 2017). Since each zeolite structure has a unique set of diffraction peaks, it is easy to identify the structure of unknown zeolites by comparing the observed XRD diffraction patterns (peak intensity and position) with the database reference in the 2θ range between $5°–40°$.

2.10.2 Filed emission scanning elctron microscopy coupled with energy dispersive X-ray spectroscopy (FESEM/EDX)

Field emission scanning electron microscopy (FESEM) is widely used in various scientific and industrial applications due to its exceptional imaging capabilities. Using a finely focused electron beam generated by a field emission electron source, FESEM scans specimens, providing high-resolution images that reveal detailed topography and morphology at the micro- and nanometer scales. The sample preparation for FESEM is simple, involving the placement of a small amount of powder on a double-sided carbon tape before a thin coat of platinum or gold is applied before FESEM examination (Wightman, 2022).

The integration of FESEM with Energy Dispersive X-ray Spectroscopy (EDX) has becoming a very powerful analytical instrument, offering comprehensive analysis on the composition and morphology of materials. EDX usually is used for the rapid determination of elemental composition of solids where the X-rays generated from a sample (during high-energy electron bombardment) are detected and analyzed to identify and quantify the elemental abundance (Yu et al., 2018).

2.10.3 Fourier transform infrared (FTIR) spectroscopy

FTIR spectroscopy is a rapid, sensitive and user-friendly technique for identifying the functional groups present in a material. The method involves the measurement of absorption of infrared radiation by the sample, which allows the identification of functional groups based on their characteristic vibrational frequencies (Dutta, 2017). In zeolite research, the IR fingerprint region of 400−1400 cm^{-1} is the most important region as it offers details on the lattice vibration of zeolites. Each type of zeolite displays distinct spectrum at this region due to the internal vibration of tetrahedral units of different framework structures (Byrappa & Kumar, 2007). Therefore, the zeolite identity can be confirmed by comparing the IR spectrum of a

zeolite sample with that of a reference. Table 2.3 shows some important vibrational wavenumbers and their corresponding vibrational bonds assignments.

Table 2.3 The possible vibration bands of zeolites in the IR fingerprint region (T = Si, Al or P) (Lesthaeghe et al., 2008)

Internal tetrahedral	**Wavenumber (cm^{-1})**	**External linkages**	**Wavenumber (cm^{-1})**
Asymmetric stretching	1250-950	Asymmetric stretching	1050–1150
Symmetric stretching	720-650	Symmetric stretching	750–820
T-O bending	420-500	Double ring (D4R, D6R)	500–650
		Pore opening	300–420

2.10.4 Nuclear magnetic resonance (NMR) spectroscopy

Nuclear magnetic resonance (NMR) spectroscopy is a very useful instrument in studying the molecular structure of substances. The fundamental operational principles of NMR involve measuring elements based on the abundance of nuclei, with particular attention given to nuclei possessing an odd atomic number (e.g. ^{1}H, ^{13}C, ^{27}Al and ^{31}P) (Pradhan et al., 2017). This technique exploits the magnetic properties of certain atomic nuclei when exposed to a strong external magnetic field and radiofrequency radiation. By analyzing the resulting NMR spectrum, detailed insights into the arrangement and interactions of atoms within a molecule or a substance can be obtained, making NMR a powerful tool in the field of structural elucidation.

NMR spectroscopy can be applied to both liquid and solid states where tetramethylsilane (TMS) is employed as a reference standard. In liquid-state NMR, molecules can move freely, leading to a sharp and narrow chemical shift in the spectrum (Salvatella, 2017). On the other hand, solid-state NMR is utilized when dealing with crystalline or amorphous solids. The resulting NMR peaks are usually broad because the molecules in solid are more constrained in movement due to their fixed positions within the solid lattice (Dudek et al., 2018).

The NMR chemical shift of a signal is associated with the local environment of the atomic nuclei being observed. The shifting can be affected by several factors such as the electronegativity of nearby atoms or functional groups, the presence of hydrogen bonding, steric hindrance, and solvent effects (Mora et al., 2020). Thus, understanding these factors is crucial for the accurate interpretation of NMR data, which gives valuable insights into the molecular structure.

2.10.5 CHN elemental analysis

CHN elemental analysis is an important analytical instrument for both qualitative and quantitative studies. This technique is particularly valuable for determining the elemental composition and stoichiometry of organic compounds where the relative proportions of carbon, hydrogen, nitrogen and oxygen present in a sample can be known.

CHN elemental analysis is initiated by combusting an organic sample in the presence of excess oxygen. During combustion, the carbon, hydrogen and nitrogen atoms in the sample are respectively converted into carbon dioxide, water and nitrogen oxides. These molecules will be separated, detected and quantified using specific detectors. The measured quantities of carbon dioxide, water and nitrogen oxides are then used to calculate the elemental composition of the sample (Dalal et al., 2023).

2.10.6 X-ray fluorescence (XRF)

X-ray fluorescence (XRF) is a widely employed analytical technique in materials science and zeolite research for determining the elemental composition of solid samples. It is particularly valued for its non-destructive nature, high sensitivity, and broad elemental coverage, enabling the detection of both major and trace elements (West et al., 2016). The principle of XRF is based on the excitation of atoms within a sample by an incident beam of primary X-rays. When inner-shell electrons are ejected, electrons from higher energy levels fall into the lower energy state, emitting secondary (fluorescent) X-rays characteristic of specific elements.

The emitted X-ray energies are then measured and used to identify and quantify the elements present in the sample. Due to its minimal sample preparation requirements and rapid analysis capabilities, XRF is often used to complement techniques like XRD by providing insight into the elemental framework that underpins the crystalline structure (Hodges et al., 2017). In zeolite research, XRF can confirm the Si/Al ratio and detect the presence of extra-framework elements or metal ions introduced during synthesis or ion-exchange processes.

2.10.7 Thermogravimetric-differential thermogravimetric analysis (TGA/DTG)

Thermogravimetric analysis has been identified as a simple, reliable, and cost-effective tool for investigating the thermal stability and composition of materials (e.g., zeolites) as a function of temperature. In TGA, a sample is subjected to a controlled temperature program. The key parameter monitored during TGA is the weight of the sample, which is continuously recorded as it undergoes heating or cooling (Parameshwaran et al., 2018). As the temperature increases, the sample experiences physical and chemical changes (e.g. decomposition, oxidation, dehydration, and volatilization) that can lead to weight loss or gain.

Differential thermogravimetric analysis (DTG) is a complementary technique to TGA. While TGA measures the weight change of a sample as a function of temperature, DTG provides additional information by analyzing the rate of change of the weight. DTG can be particularly useful in identifying reactions occurring within a temperature range which provides a more detailed analysis of complex thermal processes (Díaz et al., 2021).

2.10.8 Nitrogen (N_2) adsorption-desorption analysis

N_2 gas adsorption is a widely used technique for characterizing the surface area and porosity of materials where the sample is exposed to N_2 gas at various pressures. The gas molecules adsorb onto the solid surface at −196 °C, and the amount of N_2 adsorbed is measured as a function of pressure. The resulting isotherm, which shows the relationship between the quantity of gas adsorbed and the pressure, is then used to calculate important properties such as specific surface area, micropore surface area, external surface area, total pore volume, micropore volume, pore diameter and pore size distribution by using the Brunauer-Emmett-Teller (BET), t-plot and non-localized density functional theory (NLDFT) models, respectively.

The International Union of Pure and Applied Chemistry (IUPAC) has established six standard isotherms that describe the adsorption behavior of gases on solid surfaces (Figure 2.23) (Kumar et al., 2019). Microporous materials (pore size < 2 nm) are typically characterized by a Type I adsorption isotherm. Types II and III isotherms display monolayer-multilayer adsorption, and they are exhibited by non-porous solids (pore size >50 nm) with strong and weak adsorbent-adsorbate interaction, respectively. The mesoporous solids (pore diameter 2–50 nm) are linked to Type IV isotherm with a hysteresis loop at high P/P_o. Type V isotherm is similar to Type IV but with weak adsorbent-adsorbate interaction at low P/P_o. When stepwise multilayer adsorption

occurs, uniform nonporous substances display the Type VI isotherm.

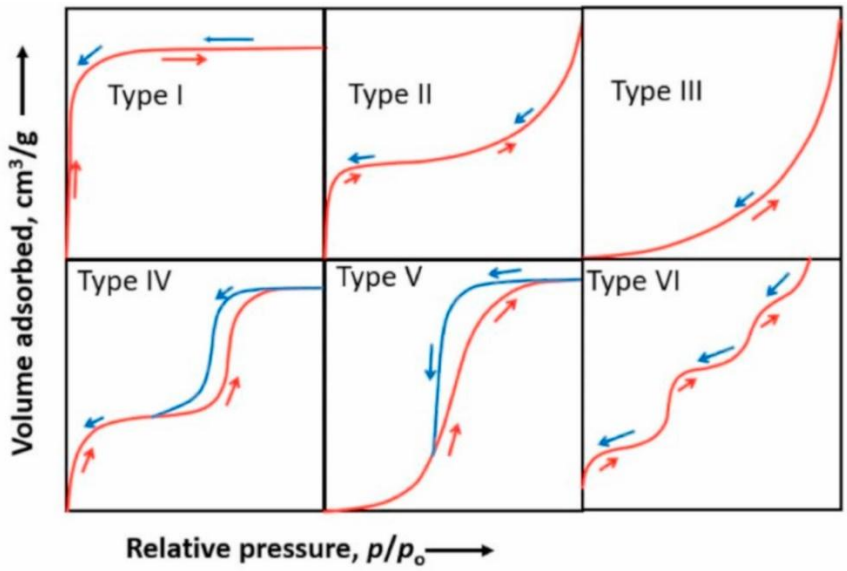

Figure 2.23 Types of adsorption isotherms classified by IUPAC (Donohue & Aranovich, 1998)

2.10.9 Temperature-programmed desorption of ammonia (TPD-NH_3)

TPD-NH_3 is a widely used technique to evaluate the acidic properties of solid catalysts. The method involves adsorbing a basic probe molecule, usually is ammonia (NH_3), onto the surface of a catalyst at a low temperature, followed by a controlled increase in temperature. As the temperature rises, NH_3 desorbs from the acid sites of catalyst, and the amount of NH_3 released is recorded using a thermal conductivity detector. This desorption profile provides key information regarding the strength and distribution of acid sites on the catalyst surface (Panczyk et al., 2006).

The results from TPD-NH_3 experiments can be interpreted to differentiate the weak, moderate and strong acid sites based on the temperatures at which NH_3 desorbs. Lower desorption temperatures correspond to weaker acid sites, while higher temperatures indicate stronger acid sites. The total quantity of desorbed NH_3 reveals the overall acid site density. This characterization is very crucial in understanding how the acidity of a catalyst relates to its catalytic performance.

2.11 Levulinic acid (LA) and ethyl levulinate (EL) ester

LA is a type of carboxylic acid that has been chosen as one of the top 12 platform compounds by the U.S. Department of Energy (Table 2.4) (Serrano-Ruiz & Dumesic, 2011). The LA generated products encompass resins, animal feed, food additives, perfumes, textile colours, fuels, antimicrobial agents and herbicides. LA possesses a carbonyl group, a carboxyl group and α-hydrogen, making it a valuable source for producing numerous chemical products through various chemical processes, including esterification, halogenation, hydrogenation, oxidative dehydrogenation, condensation and many more (Figure 2.24) (Xu et al., 2021). Furthermore, the LA molecule contains a four different group carbon atoms that exhibit asymmetry and can undergo reactions involving chirality, resulting in the formation of diverse chiral compounds (Yan et al., 2015).

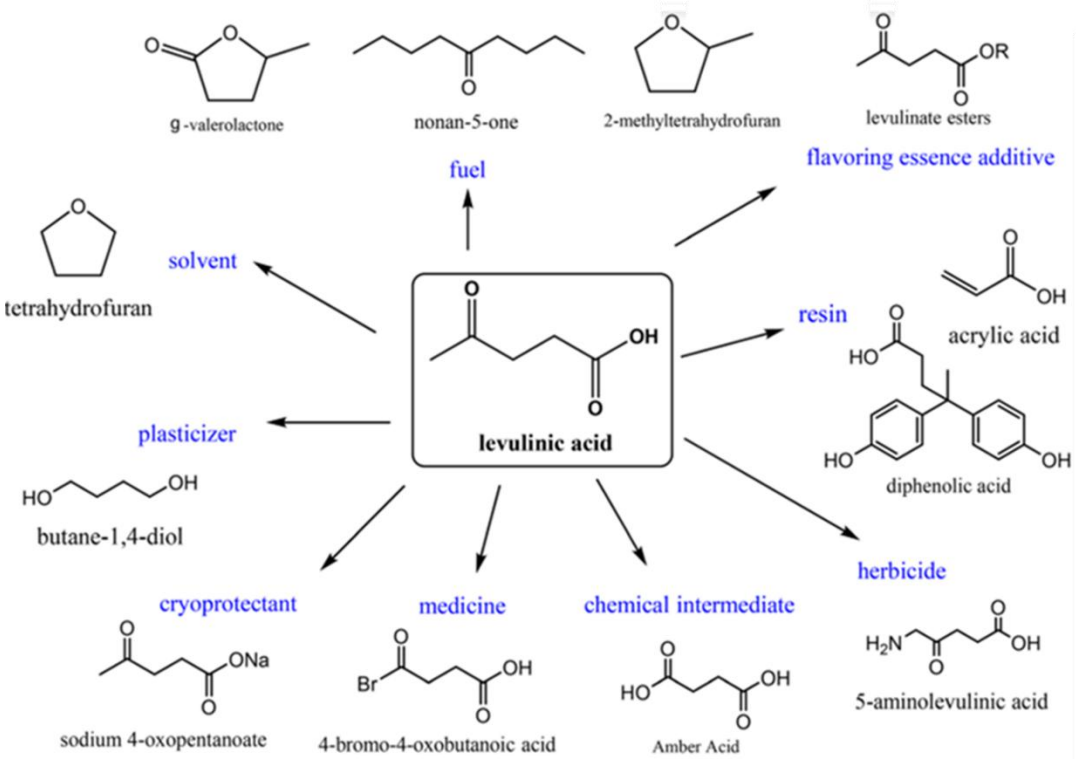

Figure 2.24 Some derivatives of LA (Xu et al., 2021)

Table 2.3 Properties of LA (Santos et al., 2021)

Properties	Values
Molar mass (g mol^{-1})	116.12
Density (kg m^{-3})	1136
Melting point (°C)	33
Solubilty	Soluble in water
Boiling point (°C)	245
Color	White
Flash point (°C)	98

EL is a useful diesel additive and recently it has received significant interest because it can be produced in large amount from low cost raw materials (Ahmad et al., 2016). When EL is added to fuels, it enhances engine efficiency and prolongs the lifespan of the engine. Additionally, it also decreases the emission of carbon monoxide and NO_x upon engine combustion (Silva et al., 2018).

EL can be synthesized using esterification reaction of LA acid and EtOH. Since the esterification reaction is a reversible reaction, several steps need to be taken in order to achieve significant levels of conversion (forward reaction). This can be accomplished by either eliminating water during the reaction, or by promoting the forward reaction through the use of an excess of EtOH (Lei et al., 2013). Typically, the esterification can be catalyzed in the presence of a catalyst (Unlu et al., 2016). In the past, homogeneous catalysts (e.g. HCl, H_3PO_4, and H_2SO_4) were used in esterification reactions. However, they possess significant drawbacks such as low reusability, hazardous, not eco-friendly, hard to separate, hard to handle and corrosive to equipment (Pileidis et al., 2014). Hence, in order to ensure the commercial feasibility of EL manufacturing, it is crucial to discover a catalyst that is efficient, eco-friendly and cost effective. In this case, SAPO zeolites can be the promising catalysts.

Ma et al. (2022) employed SAPO-34 as a catalyst for the esterification of LA to yield EL. The SAPO-34 exhibited remarkable catalytic efficacy (93.4% conversion) under non-microwave instant heating conditions (190 °C, 20 min), and its performance is better than classical SAPO-34 and comparable as HCl and H_2SO_4 homogeneous catalysts. At the same time, they also utilized SAPO-35 as a catalyst to convert LA into EL with 96.3% conversion and 100% selectivity towards EL were achieved under non-microwave immediate heating conditions (190 °C, 20 min) (Ma et al., 2022).

2.12 Lactic acid (LcA) and ethyl lactate (ELc) ester

ELc is an organic liquid that has both hydrophilic and lipophilic properties. ELc has been used in many applications, such as food additive, fragrance, flavouring agent, solvent, coating, etc. (Fraga-Corral et al., 2021); (Lamberti et al., 2021). Besides that, it is exceptionally efficient as a paint stripper and graffiti remover. Furthermore, it is utilized in the formulation of magnetic tape coatings as an alternative to

deleterious airborne pollutants such as methyl ethyl ketone, methyl isobutyl ketone, and toluene (Guzman Barrera, 2018).

ELc can be synthesized using esterification of LAc with EtOH in the presence of an acid catalyst (Komesu et al., 2017). In order to ensure high conversion, water, which is produced as a byproduct of the esterification reaction, has to be removed to prevent its hinderance on the conversion of LcA into ELc. In addition, an excess of EtOH is added during the reaction so as to promote the forward reaction.

Delgado et al. (2010) investigated the synthesis of ELc from LcA catalyzed by commercial acid resin Amberlyst 15 using a batch reactor coupled with a pervaporation unit. Their findings showed that >90% conversion of LcA into ELc can be achieved by interuppting the thermodynamic equilibrium through selectively removing water from the reaction mixture using a membrane. They also investigated the effect of initial concentrations of LcA aqueous solutions (ranging from 20 to 81 wt.%) on esterification reaction. They found that increasing the concentration of LcA in the esterification process with EtOH, combined with pervaporation, leads to a higher initial water content in the reactor. This increases the water permeation flux through the membrane, enhancing water removal and driving the reaction beyond the thermodynamic equilibrium, which results in a higher ELc yield.

CHAPTER 3

EXPERIMENTAL

3.1 Chemicals and materials

Analytical grade chemicals, such as pyridine (99%, Acros Organics), 1-bromopropane (99%, Acros Organics), aluminum isopropoxide (98%, Sigma Aldrich), phosphoric acid (85%, Sigma-Aldrich), tetraethyl orthosilicate (98%, Sigma Aldrich), 5-ethyl-2-methylpyridine (99.5%, Merck), Amberlite® IRN-78 OH^- ion-exchange resin (Acros Organic), deionized water, colloidal silica (HS-40, Sigma-Aldrich), pyrophosphoric acid (Sigma-Aldrich), levulinic acid (98%, Acros Organic) and ethanol (99.7%, Qrec), lactic acid (98%, Acros Organic) and toluene (98%, Merck).

3.2 Synthesis of 1-propylpyridinium bromide, [PPy]Br

The synthesis procedure of 1-propylpyridinium bromide ([PPy]Br) is as follows (Figure 3.1): Typically, pyridine (94.846 g, 99%, Acros Organics) and 1-bromopropane (221.20 g, 99%, Acros Organics) were mixed in a 500-mL round bottom flask. The mixture was magnetically stirred and refluxed at 70 °C for 20 h. The mixture was subjected to rotary evaporation (100 rpm) at 60 °C under vacuum (50 mbar) to remove the nonreacted 1-bromopropane. The obtained yellowish solid was then soaked in acetone (200 mL, 4 h) for 4 times before it was dried in an oven at 105 °C overnight to obtain the [PPy]Br ionic salt.

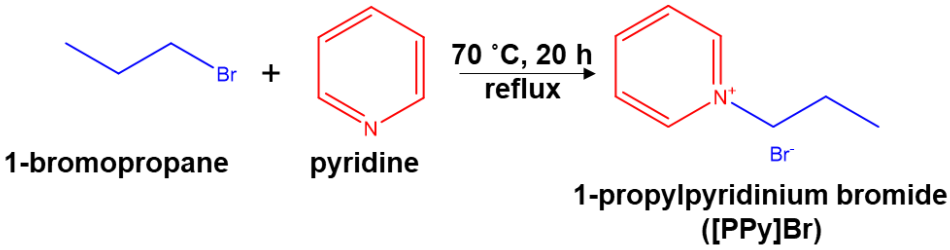

Figure 3.1 Synthesis of 1-propylpyridinium bromide ([PPy]Br)

3.3 Ionothermal synthesis of silicoaluminophosphate number 11 (SAPO-11)

Initially, aluminum isopropoxide (0.192 g, 98%, Sigma Aldrich) was placed into a Teflon-lined stainless-steel autoclave. Next, the [PPy]Br ionic liquid (7.000 g), phosphoric acid (0.192 g, 85%, Sigma-Aldrich) and tetraethyl orthosilicate (0.056 g, 98%, Sigma Aldrich) were subsequently added. The final chemical composition had a molar ratio of 1.0Al: 1.8P: 0.3Si: 38[PPy]Br. The autoclave was capped and placed in an oven at 150 °C for various crystallization times (110–200 h). The solid product was recovered using high-speed centrifugation (10000 rpm, 5 min). The process of dispersion and purification with distilled water was repeated thrice before the final solid product was dried at 90 °C overnight. The resulting as-synthesized SAPO-11 was calcined at 580 °C for 6 h at a ramping rate of 1.5 °C min^{-1} under air atmosphere.

For the study of the effects of synthesis variables (heating temperature, phosphorous content, silicon amount and [PPy]Br concentration), a similar synthesis procedure was applied wherein the resulting ionogel with a chemical composition of 1.0Al: xP: ySi: z[PPy]Br (x = 1.2–2.4, y = 0–0.3, z = 30–54) was heated at 130–160 °C for 133 h as summarized in Table 3.1.

Table 3.1 The chemical composition of ionogel, crystallization time, heating temperature and phase products obtained for the synthesis parameters effect study

Sample	Variable parameter	Ionogel molar composition				T (°C)	t (h)	Products*
		Al	P	Si	[PPy]Br			
E-1	Crystallization time, t	1.0	1.8	0.3	38	150	110	Amorphous
E-2							120	Amorphous>AEL
E-3							133	AEL
E-4							200	AEL>AFI
E-5	Heating temperature, T	1.0	1.8	0.3	38	130	133	Amorphous
E-6						140		Amorphous>AEL
E-3						150		AEL
E-7						160		Berlinite>AEL
E-8	P	1.0	1.2	0.3	38	150	133	Amorphous
E-3			1.8					AEL
E-9			2.1					AEL>Berlinite
E-10			2.4					AEL=Berlinite>AFI
E-11	Si	1.0	1.8	0	38	150	133	AEL=Berlinite
E-12				0.1				AEL=Tridymite>AFI
E-3				0.2				AEL>Tridymite
E-13				0.3				AEL
E-14	[PPy]Br	1.0	1.8	0.3	14	150	133	Tridymite>>AEL>AFI
E-15					22			Tridymite=AEL
E-16					30			AEL>>Tridymite
E-3					38			AEL

3.4 Preparation of 5-ethyl-2-methyl-1-propylpyridinium hydroxide ([empy]OH) template solution

5-Ethyl-2-methyl-1-propylpyridinium hydroxide ([empy]OH) was prepared as in Figure 3.2. Initially, 5-ethyl-2-methylpyridine (2.955 g, 99.5%, Merck) and 1-bromopropane (3.590 g, 99%, Merck) in a molar ratio of 1:1.2 were reacted in a Monowave 50 reactor (Anton Paar) at 160 °C for 20 min (800 rpm). After the reaction, the non-reacted 1-bromopropane was eliminated by rotary evaporation at 90 °C. The resulting 5-ethyl-2-methyl-1-propylpyridinium bromide ([empy]Br) ionic liquid was

soaked with acetone (Qrec, 20 mL, 4 h) for 5 times, followed by drying at 100 °C overnight. The ionic liquid was then dissolved again in hot EtOH and subjected to recrystallization in cold EtOH for further purification process.

To obtain [empy]OH, the following procedure was used. First, a mixture of [empy]Br (30.000 g), Amberlite® IRN-78 OH^- ion-exchange resin (30.000 g, Acros Organic) and deionized water (75.000 g) was stirred (200 rpm, 16 h) in a 500-mL polypropylene bottle. After ion exchange process, the resin was separated from the template solution through vacuum filtration. The %OH^- exchange was determined by titrating 1.0 mL of filtrate with 0.05 M HCl. The ion exchange, filtration and titration were repeated for another three cycles before the template solution was concentrated using vacuum rotary evaporation (80 °C). The final template solution of 38.5 wt% of [empy]OH with 90.7% OH^- exchanged was obtained.

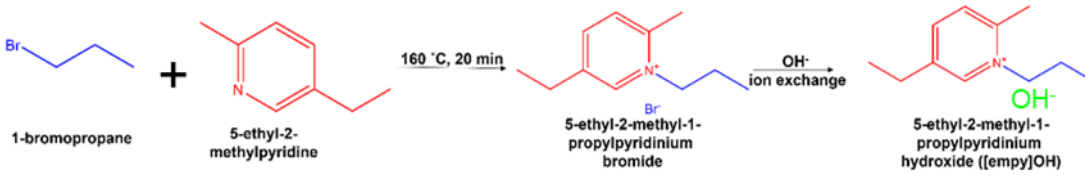

Figure 3.2 Synthesis route of 5-ethyl-2-methyl-1-propylpyridinium hydroxide ([empy]OH)

3.5 Synthesis of SAPO-5 zeolite

3.5.1 Synthesis of SAPO-5 by using phosphoric acid (H_3PO_4) as P source (PA-n)

Aluminum isopropoxide (0.847 g, 98%, Acros Organics) was stirred (500 rpm) with [empy]OH template solution (6.250 g) where the dissolution took about 30 min. H_3PO_4 (1.999 g, 85%, QRec) was slowly added in a dropwise manner where stirring (500 rpm); the adding process took about 25 min to complete. The mixture was then mixed with water (1.980 g) and colloidal silica (0.184 g, HS-40, Sigma-Aldrich) to produce a precursor with a composition of

$1Al_2O_3$:$4.27P_2O_5$:6.33[empy]OH:$0.60SiO_2$:$170H_2O$. The mixture was further stirred for another 5 min before being transferred into a 15-mL PTFE stainless-steel autoclave for crystallization at 180 °C at various times (0, 0.2, 0.5, 1.0, 3.0 and 5.0 h). The obtained solid products were purified with water using centrifugation (10000 rpm × 4 tubes of 50 mL × 6 times, 8 min) prior drying in a conventional oven (80 °C) and calcination (600 °C, 6 h, 1 °C min^{-1}). The samples crystallized using H_3PO_4 as the P source at different times were denoted as PA-*n*, where *n* represented the crystallization period in h.

3.5.2 Synthesis of SAPO-5 by using pyrophosphoric acid ($H_4P_2O_7$) as P source (PyP-n)

The synthesis protocol of SAPO-5 with $H_4P_2O_7$ (mixing, addition of P source, hydrothermal crystallization, washing, drying and calcination) is similar to that of using H_3PO_4 (Section 3.5.1) except the additional step of 85% $H_4P_2O_7$ aqueous solution whereby it was prepared by dissolving $H_4P_2O_7$ (1.820 g, Sigma-Aldrich) into distilled water (0.331 g). The solids crystallized at different time (0, 0.2, 0.5, 1.0, 3.0 and 5.0 h) were labelled as PyP-*n*, where *n* indicated the crystallization time in h.

3.6 Characterization

3.6.1 X-ray powder diffraction (XRD)

In this work, the crystallization process and crystalline phase of solid samples were studied using a Bruker D8 AVANCE diffractometer operated at a scanning rate of 0.2° min^{-1}, 40 kV and 10 mA with the copper Kα radiation source (λ = 1.5406 Å).

3.6.2 Field emission scanning electron microscopy coupled with energy-dispersive X-ray spectroscopy (FESEM/EDX)

In this research, the crystal size and morphology of solids were analyzed using a HITACHI Regulus 8220 FESEM (Tokyo, Japan) at low acceleration voltage (5 kV). Prior analysis, a small amount of sample was placed on a double-sided carbon tape.

3.6.3 Fourier transform infrared (FTIR) spectroscopy

In this research, the functional groups of a ionic liquid and zeolite samples were confirmed using a Perkin Elmer's System 2000 infrared spectrometer (resolution 4 cm^{-1}, 16 scans) where the KBr pellet technique was applied (KBr:sample mass ratio = 60:1).

3.6.4 Nuclear magnetic resonance (NMR) spectroscopy

In this work, liquid ^{1}H and ^{13}C NMR spectra were recorded with a Bruker Advance 500 MHz spectrometer operated at 500 and 126 MHz, respectively, using a single pulse excitation with $\pi/2$ (3 μs) pulse where deuterium oxide (D_2O) was used as a solvent. In both analyses, and tetramethylsilane (TMS) was used as an internal standard. Meanwhile, the NMR spectra of ^{27}Al and ^{31}P nuclei were recorded with single pulse experiments on a Bruker Avance 500 MHz (11.7 T) spectrometer at ^{27}Al and ^{31}P Larmor resonance frequencies of 130.30 and 202.42 MHz, respectively. 3.2 mm zirconia rotors were used and the spinning rate was fixed to 14 kHz. ^{27}Al MAS NMR spectra were acquired using a pulse width of 1.75 μs ($\pi/6$), where 4096 scans were made for all samples with a recycle delay of 1 s. The ^{31}P MAS NMR spectra were recorded using a pulse width of 5 μs ($\pi/2$), where 256 scans were acquired with 20 s of recycle delay. The chemical shifts were calibrated with H_3PO_4 and 0.1M $Al(NO_3)_3$ aqueous solution (as reference) for ^{31}P and ^{27}Al NMR spectra, respectively.

3.6.5 CHN elemental analysis

In this work, the elemental constituents of the [PPy]Br and [empy]Br ionic liquids were determined using a Perkin Elmer 2400 Series II CHNS/O analyzer. The sample mass (ca. 5 mg) was first measured before it was placed into a combustion chamber. The measurement was then initiated with combustion and elemental composition analysis.

3.6.6 X-ray Fluorescence (XRF)

In this work, the elemental composition of the solid samples was analyzed using a Malvern Panalytical Zetium X-ray fluorescence (XRF) spectrometer. The instrument is equipped with a Rh anode X-ray tube and was operated under vacuum conditions at 60 kV and 50 mA.

3.6.7 Thermogravimetric-differential thermogravimetric analysis (TGA/DTG)

In this work, the thermal stability and composition of samples (0.030 g) were measured using a Perkin Elmer's TGA 4000 thermogravimeter equipment, where the samples were heated from 30 °C until 800 °C at a rate of 20 °C min^{-1} under air flow rate of 100 mL min^{-1}.

3.6.8 Nitrogen (N_2) adsorption-desorption analysis

In this work, the porous properties of solid samples were studied using a Micromeritics ASAP 2010 analyzer where the sample (ca. 80 mg) was first degassed at 250 °C for 10 h before subjecting to N_2 adsorption at −196 °C. The specific surface area was determined by the BET method, while the micropore surface area and external surface area were computed using the t-plot model. The total pore volume was calculated using the total N_2 uptake at P/P_o = 0.998. On the other hand, the pore size distribution (micropores, mesopores and macropores) was determined using the non-local

density functional theory (NLDFT) model.

3.6.9 Temperature-programmed desorption of ammonia (TPD-NH3)

In this work, the surface acidity of SAPO samples was determined using AutoChem II 2920 TPD analyzer probed with NH_3. The samples were first pretreated (400 °C, 30 min) under He flow (30 cm^3 min^{-1}). After cooling down to 50 °C, the sample was saturated with NH_3 gas for 30 min. The physisorbed NH_3 was removed by purging with He before heating to 600 °C at a rate of 10 °C min^{-1} for NH_3 desorption.

3.6.10 Gas chromatography flame ionization detector (GC-FID)

GC is an important analytical technique for separating and analyzing volatile compounds in a mixture (Okejiri, 2021). It is based on the principles of migration and partitioning of components between a stationary phase and a mobile phase. Typically, a microsyringe is used to inject the liquid sample (<1 µL) into the heated injector to allow evaporation before the vaporized compounds are carried into the GC column (stationary phase) by an inert gas (mobile phase) (Falaki, 2019). The analytes in the mixtures are then separated based on polarity, chirality, boiling point and molecular mass of the compounds (Santos & Schug, 2017). The peak retention and peak intensity produced by the compound can then be used to identify and quantify each compound in the mixture.

In this research, Agilent 7890A gas chromatograph was used for qualitative and quantitative analyses for catalytic reactions where 0.2 µL of sample was injected and toluene was used as an internal standard. Table 3.3 lists the operating requirements for the GC analysis.

Table 3.2 GC and GCMS measurement conditions

Parameter	Condition
Mobile phase	Nitrogen
Column	Equity-5
Inlet temperature (°C)	250
Splitting ratio	1:100
Column flow rate (mL min^{-1})	25
Initial temperature (°C)	40
Hold time (min)	0
Heating rate (°C min^{-1})	15
Final temperature (°C)	250
Final hold time (min)	1
Detector temperature (°C)	250

3.6.11 Gas chromatography-mass spectrometry (GC-MS)

GC-MS is a powerful analytical technique that combines the separation capability of GC with the mass analysis capability of MS. This hybrid technique allows for the identification and quantification of individual compounds in a mixture, making it a widely used tool in various scientific and industrial applications (Hussain & Maqbool, 2014).

As the separated compounds exit the GC column, they enter the mass spectrometer. The compounds are ionized before the fragmented ions are accelerated and separated by a strong magnetic field according to the mass-to-charge ratio (m/z) of the ions. Since each substance has a distinct mass spectrum pattern, it is possible to identify the compounds by comparing them to the mass spectra of known substances (Skoog et al., 2017).

In this research, the identification of organic compounds in catalytic reaction was performed on an Agilent 7000 Series Triple Quad GC-MS equipment where 0.2 µL of sample was injected into the instrument. Table 3.3 lists the operating requirements for the GCMS analysis.

3.7 Catalytic reaction

3.7.1 Esterification of levulinic acid and ethanol over SAPO-11 catalyst

The esterification of LA and EtOH into EL over an E-3 sample (hereafter referred to as SAPO-11) was performed under non-microwave instant heating conditions that mimic rapid microwave heating. Initially, the calcined SAPO-11 (0.100 g) was activated at 300 °C for 3 h before it was mixed with LA (0.040 g, 0.34 mmol, 98%, Acros Organic) and EtOH (0.202 g, 4.38 mmol, 99.7%, Qrec) in a 15-mL glass vial. The mixture was capped and heated in an Anton Paar's Monowave 50 non-microwave instant heating reactor at 150–180 °C for 0–60 min under magnetic stirring (800 rpm). The catalyst was separated using centrifugation (10,000 rpm, 10 min). The reaction liquid (1 µL) was withdrawn and injected into a GC-MS (Agilent 7000 Series Triple Quad, Santa Clara, CA, USA) and a GC-FID (Agilent's HP6890 GC, Santa Clara, CA, USA) for qualitative and quantitative analyses, respectively; toluene (98%, Merck) was used as an internal standard. Each experiment was repeated thrice, and the error bars were plotted based on the three replicate experiments. The LA conversion and product selectivity were calculated using Equations 3.1 and 3.2:

$$\text{Conversion (\%)} = \frac{\left(\frac{A_{LA}}{A_{Toluene}}\right)_{t0} - \left(\frac{A_{LA}}{A_{Toluene}}\right)_{ti}}{\left(\frac{A_{LA}}{A_{Toluene}}\right)_{t0}} \times 100\% \quad (3.1)$$

$$\text{Selectivity (\%)} = \frac{A_{EL}}{A_{Total}} \times 100\% \quad (3.2)$$

where A_{LA} and $A_{Toluene}$ were the peak area of the LA and toluene (internal standard), respectively. t_0 and t_i were the reaction times at 0 h and i h, respectively, A_{EL} was the

peak area of the product (EL) and A_{Total} was the total peak area of products obtained.

The effects of other catalytic reaction parameters were also investigated such as the molar ratio of LA to EtOH (1:11), the reaction temperature (150–180 °C), the reaction duration (0–60 min), the mass of solid catalyst (0–1.25 g), the heating mode (autoclave, reflux, non-microwave immediate heating), and the types of catalyst (HCl, H_2SO_4, CH_3COOH, p-toluenesulfonic acid). The catalytic reaction process is comparable for all catalyst types when utilising the same amount of SAPO-11 catalyst (0.100 g, or 17.98 μmol) but with various catalysts.

3.7.2 Esterification of lactic acid and ethanol over SAPO-5 catalysts

ELc was produced *via* esterification of LcA and EtOH under non microwave instant heating conditions. Typically, the calcined SAPO-5 (0.100 g) prepared from pyrophosphoric acid and phosphoric acid as a phosphorus source was first activated (300 °C, 3 h) before it was transferred into a 15-mL glass vial. EtOH (0.483 g, 612 mmol, 99.7%, Qrec) and LcA (0.093 g, 77 mmol, 98%, Acros Organic) were then added. The mixture was sealed and heated for 0–60 min at 120–160 °C with magnetic stirring (800 rpm) in an Anton Paar's Monowave 50 non-microwave instant heating reactor. After reaction, the reaction liquid was isolated from the catalyst solid via centrifugation (8000 rpm, 10 min) before it was injected into a GC-MS (Agilent 7000 Series Triple Quad) and a GC-FID (Agilent HP6890) for qualitative and quantitative analyses, respectively; toluene was used as an internal standard (98%, Merck). All the experiment was run thrice and the averaged values with standard deviations (as error bars) were reported. The LcA conversion and product selectivity were calculated using Equations 3.3 and 3.4:

$$\text{Conversion (\%)} = \frac{\left(\frac{A_{LcA}}{A_{Toluene}}\right)_{t0} - \left(\frac{A_{LcA}}{A_{Toluene}}\right)_{ti}}{\left(\frac{A_{LcA}}{A_{Toluene}}\right)_{t0}} \times 100\% \qquad (3.3)$$

$$\text{Selectivity (\%)} = \frac{A_{ELc}}{A_{Total}} \times 100\% \quad (3.4)$$

where A_{LcA} and $A_{Toluene}$ were the peak area of the LcA and toluene (internal standard), respectively. t_0 and t_i were the reaction times at 0 h and i h, respectively, A_{ELc} was the peak area of the product (ELc) and A_{Total} was the total peak area of products obtained. the turnover number (TON) and turnover frequency (TOF) were calculated by using the Equations (3.5) and (3.6):

$$\text{TON} = \frac{(\%\ \text{Conversion})(\text{Number of moles of substrate})}{\text{Number of moles of catalyst}} \quad (3.5)$$

$$\text{TOF (min}^{-1}\text{)} = \frac{\text{TON}}{\text{Time (min)}} \quad (3.6)$$

In addition, the effects of other catalytic reaction parameters were also examined. For example, reaction temperature (120−160 °C), reaction time (0− 60 min), mass of solid catalyst (0−1.25 g), molar ratio of LcA:EtOH (1:3, 1:5, 1:10, 1:15, 1:20), heating mode (autoclave, reflux, non-microwave instant heating), types of catalyst (HCl, H_2SO_4, CH_3COOH, *p*-toluenesulfonic acid, H_3PO_4, SAPO-11) and type of alcohols (methanol, 1-propanol, 2-propanol, 1-butanol, 2-butanol). For the effect of types of catalyst, the catalytic reaction procedure is similar but using different catalysts with same amount of SAPO-5 catalyst (0.100 g equivalent to 17.98 μmol).

3.7.3 Catalyst reusability study

After the esterification reactions, the used catalyst was cleaned with diethyl ether (10 mL, 4 times) and then dried (60 °C, 2 h). The catalyst was activated again (300 °C, 4 h) before it was mixed with the reactants where the number of reactants for producing the best results was used. The reaction was carried out in the Monowave-50 reactor using the optimum reaction time and temperature. Similar procedure was used for the subsequent runs of reaction.

CHAPTER 4

IONOTHERMAL SYNTHESIS OF SAPO-11 USING 1-PROPYL PYRIDINIUM BROMIDE

4.1 Characterization of 1-propylpyridinium bromide, [PPy]Br

The FTIR spectrum of [PPy]Br is shown in Figure 4.1. The O-H stretching of the adsorbed water was recorded at 3420 cm^{-1}. The absorption bands at 2877 and 2975 cm^{-1} are due to the Csp^3-H stretching and the Csp^2-H stretching is observed at 3054 cm^{-1}. The stretching modes of C-N and C=N were found at 1173 and 1486 cm^{-1}, respectively, whereas the absorption band at 1637 cm^{-1} was dedicated to the aromatic C=C stretching vibration. The absorption bands at 683 and 772 cm^{-1} were attributed to the bending vibrations of CH_2 and CH_3 groups, respectively (Bruice, 2017).

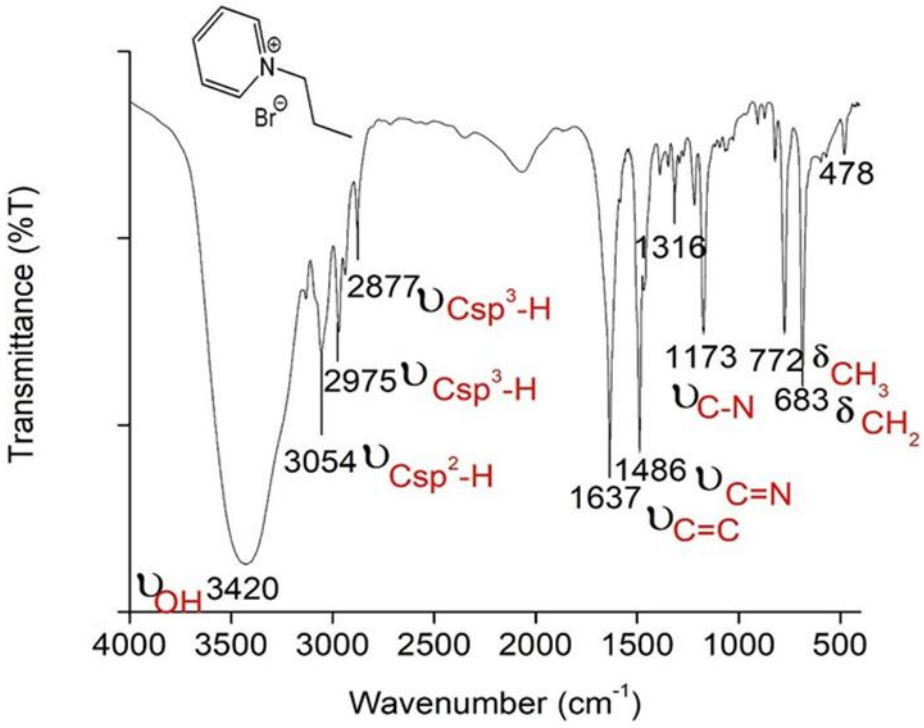

Figure 4.1 FTIR spectrum of [PPy]Br

The [PPy]Br ionic salt was further subjected to ^{1}H NMR spectroscopy characterization (Figure 4.2). The hydrogen atoms (H1) attached to the methyl carbon (marked as Carbon 1) show a triplet at 1.03 ppm. A multiplet (H2) observed at 2.13 ppm was due to the CH_2 group attached to the Carbon 2. Furthermore, since Carbon 3 was located next to Carbon 2 and N atom, the deshielded hydrogen (H3) showed a triplet at 4.71 ppm. The H4, H5 and H6 are bonded to the aromatic ring. Thus, their nuclei are more deshielded which causes their resonance occurs downfield. Among these three protons, H4 was the most deshieded and it resonated at 8.98 ppm as a doublet. The other two protons resonated at 8.19 ppm (H5, triplet) and 8.66 ppm (H6, triplet). NMR peaks were observed showing high impurity of [PPy]Br prepared.

The C, H and N elemental analysis of [PPy]Br was performed, and the results were shown in Table 4.1. As can be seen, the experimental values for the three elements were almost similar to the theoretical ones. Thus, it confirmed the purity of the ionic salt.

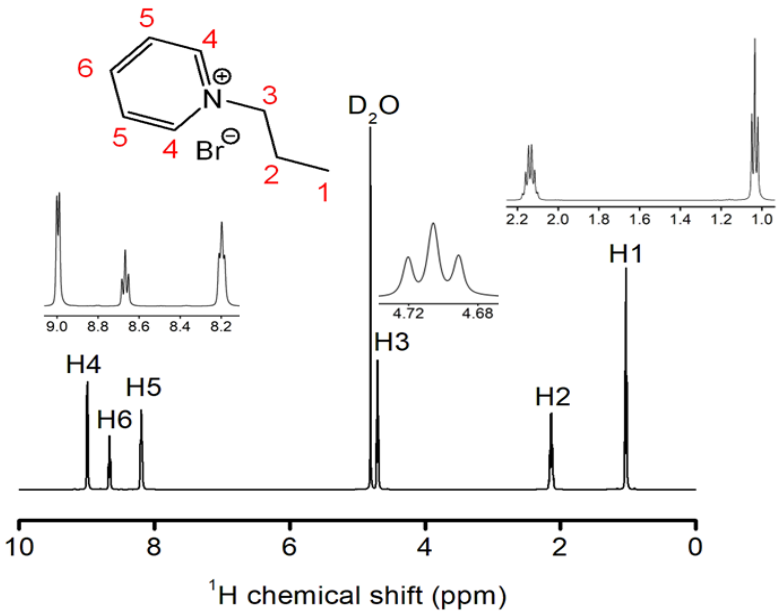

Figure 4.2 ^{1}H NMR spectrum of [PPy]Br

Table 4.1 Elemental composition of [PPy]Br

Elements	Experimental values (%)	Theoretical values (%)
Carbon	46.81	47.55
Hydrogen	5.85	5.94
Nitrogen	6.83	6.93

4.2 Time dependent study of ionothermal crystallization of SAPO-11

In this work, SAPO-11 was crystallized under ionothermal conditions (150 °C) using 1-propylpyridinium bromide ([PPy]Br) as both structure-directing agent and solvent, which is different from the hydrothermal technique applied in the classical zeolite synthesis system. At 50 h, no solid product was recovered upon centrifugation, indicating the complete dissolution and participation of inorganic reactants in the ionic liquid. At 110 h, a small amount of amorphous nanoparticles (140 nm) was formed and sedimented, indicating that the polymerization of inorganic Si, Al and P oligomers into a heavier solid had taken place (E-1, Figure 4.3a). A semicrystalline SAPO-11 product, consisting of spherical amorphous nanoparticles (ca. 270 nm) and broomstick-like particles (ca. 1.9 μm), starts to form at 120 h revealing the occurrence of nucleation (E-2, Figure 4.3b).

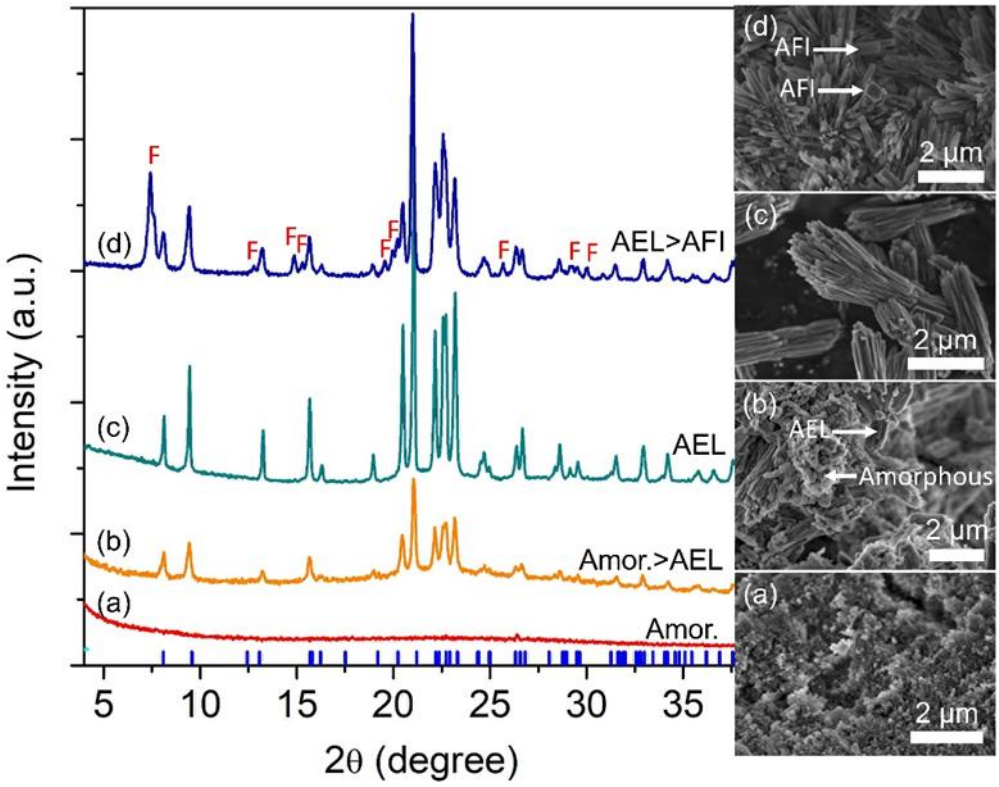

Figure 4.3 XRD patterns and FESEM images of (a) E-1, (b) E-2, (c) E-3 and (d) E-4 samples ionothermally heated at 150 °C for 110 h, 120 h, 133 h and 200 h, respectively. F denotes the presence of AFI crystalline phase. The theoretical XRD peak positions of the AEL phase are shown as vertical blue lines

The XRD amorphous hump completely disappears after 133 h of ionothermal heating, and the XRD pattern of the E-3 solid displays intense peaks which can perfectly match with the simulated XRD pattern of AEL-type zeolite (E-3, Figure 4.3c). Meanwhile, the FESEM confirms that all the amorphous nanoparticles were consumed as nutrients for the growth of SAPO-11 (Figure 4.3c). As a result, large and well-defined broomstick crystals (ca. 2.3 μm) are formed, which are completely different from those crystallized in other systems (screw-like (Tiuliukova et al., 2018), nanoaggregate (Chen et al., 2017), and columnar (Xu et al., 2013)). However, after 200 h of heating, the XRD analysis shows co-crystallization of SAPO-11 with SAPO-5 (AFI topology) (2θ = 7.43°, 20.97° and 22.38°) as a minor phase in the E-4 sample, thus revealing the metastability of SAPO-11 zeolite. This metastability implies that SAPO-11 is a kinetically favored phase that can gradually transform into a more

thermodynamically stable structure, such as SAPO-5, under extended thermal treatment (Deneyer et al., 2020).

The entire SAPO-11 crystallization process was studied using IR spectroscopy. Three IR bands are seen at 1116, 685 and 469 cm^{-1} at 110 h, respectively, which correspond to asymmetric, symmetric O-P-O stretchings and AlO_4 (Zhang et al., 2007) (Figure 4.4a). Extending the heating duration to 120 h results in a more resolved spectral pattern, particularly below 800 cm^{-1}, where three distinct IR bands are observed in this region (Figure 4.4b). The IR band due to double-6-ring vibration, which is the secondary building unit for the SAPO-11, is detected at 715 cm^{-1}. This data is consistent with the XRD results that the SAPO-11 nuclei has formed in the midst of amorphous entities after 120 h. Additionally, the bending modes of PO_4 and AlO_4 are confirmed based on the bands at 553 and 467 cm^{-1}, respectively.

When fully crystalline SAPO-11 is formed at 133 h, these three signals become stronger and blue-shifted (Figure 4.4c). Additionally, three IR bands are seen at 732, 554, and 466 cm^{-1} which are due to P-O-Al stretching, asymmetric O-P-O stretching, and P-O stretching modes, respectively. The peak shifting from 715 to 732 cm^{-1} is observed due to the change of framework skeleton (T-O-T bonds become shorter) with prolonging the crystallization time. At 466 cm^{-1}, a weak shoulder band due to Al-O bending vibration is also observed.

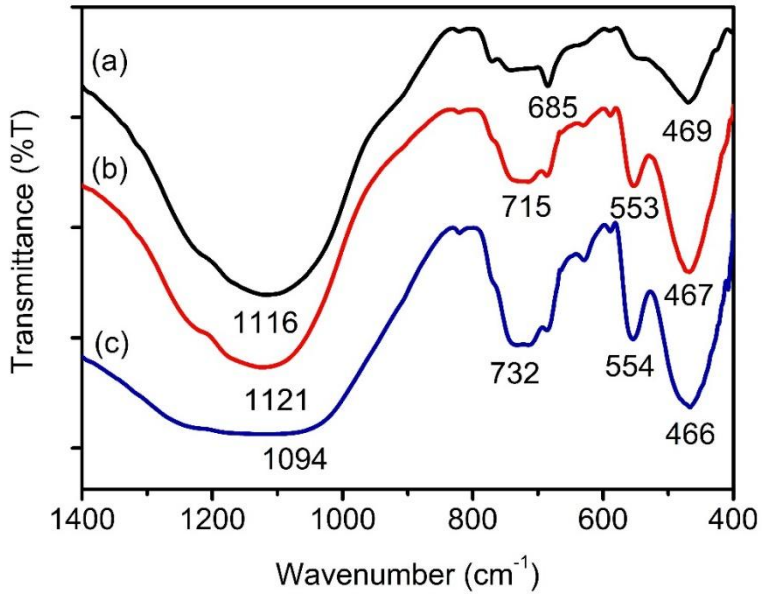

Figure 4.4 IR spectra of samples after (a) 110 h (amorphous), (b) 120 h (amorphous + SAPO-11), (c) 133 h (SAPO-11)

4.3 Effect of synthesis conditions

4.3.1 Effect of heating temperature

The heating temperature is very important for chemical processes as it provides energy to initiate the reactions (Choo et al., 2019). Hence, the ionothermal synthesis of SAPO-11 was performed by heating the ionogel of 1.0Al: 1.8P: 0.3Si: 38[PPy]Br at 130 °C, 140 °C, 150 °C and 160 °C (denoted as E-5, E-6, E-3 and E-7, respectively) for 133 h to study its influence on the crystallization profile of SAPO-11. A low temperature seems to be insufficient to promote crystallization: the E-5 is produced as an amorphous nanospherical solid (ca. 20 nm) while E-6 contains rarely stick-like SAPO-11 crystals (ca. 940 nm) in the amorphous solids (Figure 4.5a,b). Only several XRD peaks due to SAPO-11 are shown (2θ = 9.36° [020], 20.41° [310], 21.11° [002], 22.23° [231], 22.68° [141] and 23.13° [240]). The XRD peaks are broadened, revealing small SAPO-11 crystallites, as also confirmed by the FESEM data (Wong et al., 2017). By providing more energy through increasing the temperature to 150 °C, it is possible

to see the full crystallization of SAPO-11 zeolite which results in the emergence of typical AEL X-ray diffraction peaks (E-3, Figure 4.5c). As shown, the SAPO-11 exhibits broomstick-like features, while the morphological structure strongly depends on the synthesis technique (e.g., hydrothermal, ionothermal, dry gel conversion, microwave heating, etc.), hydrophilicity and type of ionic liquid used (Chen et al., 2022). Supplying excessive energy by raising the temperature to 160 °C leads to the activation and crystallization of a more stable crystalline phase, where a partial transformation of SAPO-11 into berlinite metasomatic phosphate (a nonporous crystalline dense phase) occurs (E-7, Figure 4.5d). Hence, 150 °C is the optimum temperature for crystallizing SAPO-11 in an ionothermal environment.

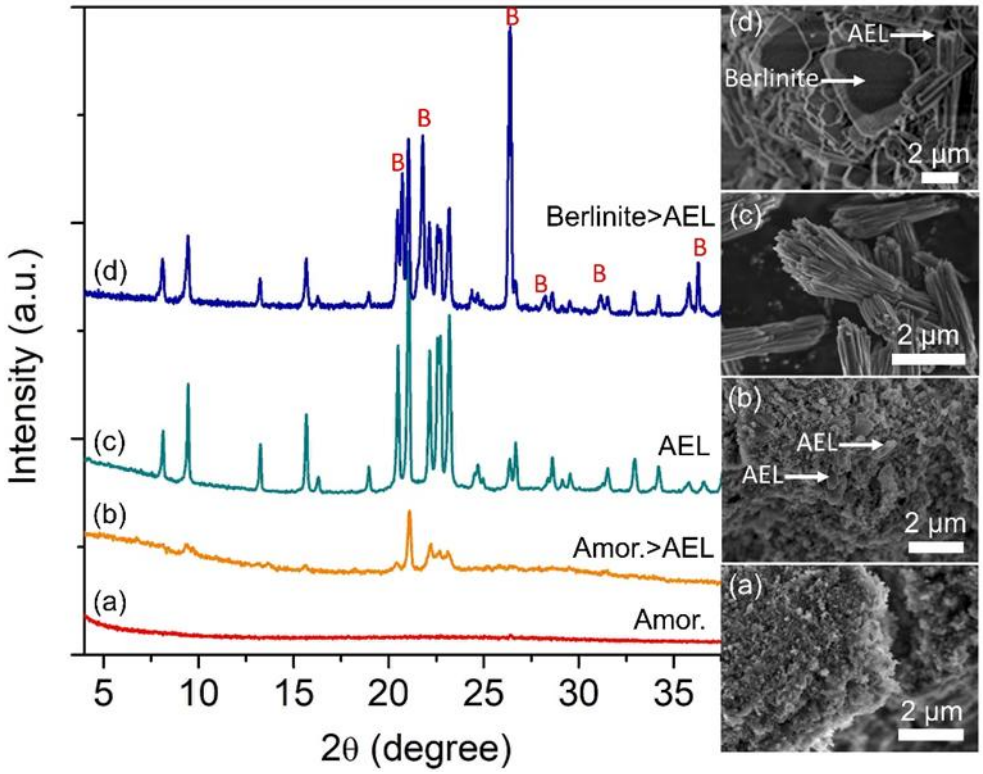

Figure 4.5 XRD patterns and FESEM micrographs of (a) E-5, (b) E-6, (c) E-3 and (d) E-7 samples prepared using the ionogel of 1.0Al: 1.8P: 0.3Si: 38[PPy]Br and heated at 130 °C, 140 °C, 150 °C and 160 °C for 133 h, respectively

4.3.2 Effect of P/Al molar ratio

The amount of phosphorus added (in H_3PO_4 form) to the ionogel plays a very important role in the crystallization process, because phosphorus is one of the main components of SAPO-11 zeolite besides aluminum and silicon. In addition, H_3PO_4 also modulates the pH of the ionogel, which can alter the entire crystallization environment of zeolites (Wang et al., 2014). Thus, the amount of H_3PO_4 (presented in P/Al molar ratio) is studied by heating the ionogel of 1.0Al: xP: 0.3Si: 38[PPy]Br (x = 1.2: E-8, x = 1.8: E-3, x = 2.1: E-9, x = 2.4: E-10) at 150 °C for 133 h. When x = 1.2, an amorphous solid with irregular shape, as proven by the broad XRD hump at 2θ = 20°–33°, is observed (Figure 4.6a). Increasing P content to x = 1.8, we witness the complete conversion of the amorphous solid into SAPO-11. This reveals the importance of H_3PO_4 in providing an adequate pH environment for the promotion of nucleation and crystal growth (Han et al., 2021). However, further increasing the x values to 2.1 and 2.4 produces a more acidic ionogel that favorably crystallizes berlinite dense phase and AFI-type zeolite, and this observation is in line with the work reported by (Khoo et al., 2013).

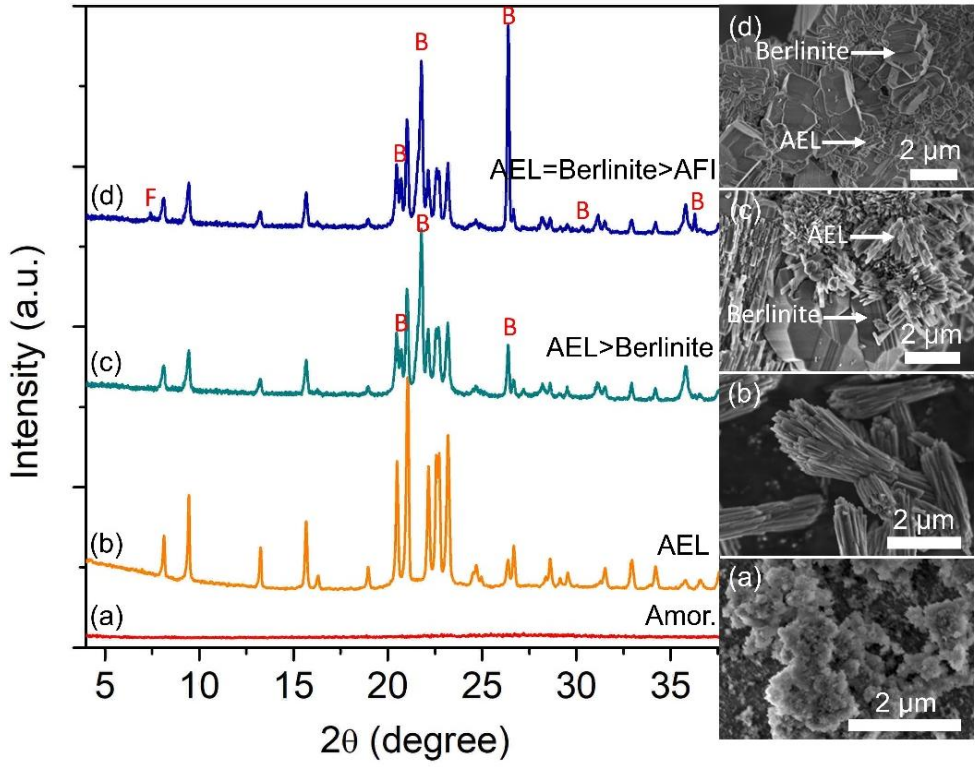

Figure 4.6 XRD patterns and FESEM images of (a) E-8 (x = 1.2), (b) E-3 (x = 1.8), (c) E-9 (x = 2.1) and (d) E-10 (x = 2.4) samples. The samples were prepared using the ionogel of 1.0Al: xP: 0.3Si: 38[PPy]Br heated at 150 °C for 133 h. F and B denote the presence of AFI and berlinite crystalline phases, respectively

4.3.3 Effect of Si content

The element Si is another primary building unit component of the SAPO-11 zeolite framework that controls the crystallization process (Ma et al., 2022). In addition, the isomorphous substitution of Si^{4+} into the SAPO-11 framework may result in variable physiochemical attributes (e.g., creating acid sites) which are highly demanding in heterogeneous catalysis (Wen et al., 2019). Hence, the amount of Si content in ionogels of 1.0Al: 1.8P: ySi: 38[PPy]Br was varied (y = 0, 0.4, 0.9 and 1.3) to study its effects on the crystallization of SAPO-11. When no Si (y = 0) is added, tridymite (2 θ = 21.6° [112] and 21.8° [−404]) as a competing phase is formed together with SAPO-11 (E-11, Figure 4.7a). The results from the FESEM micrograph also agree with the XRD data showing that bulk SAPO-11 crystals with stick-like shape (14 μm) are cocrystallized with hexagonal tridymite crystals. When y = 0.4, both

phases remain dominant, with a small amount of SAPO-5 (AFI topology) phase (2θ = 7.42° [100]) detected (E-12, Figure 4.7b). In SEM, the SAPO-5 zeolite can be characterized by its hexagonal rod morphology, which is commonly reported for AFI-type molecular sieves (Basina et al., 2018). SAPO-11 is formed at the expense of tridymite as the Si content increases until fully pure SAPO-11 is obtained at y = 1.3 (E-3, Figure 4.7d). Hence, the results show that varying the Si content has a considerable effect on phase selectivity during the ionothermal process (Wang et al., 2016).

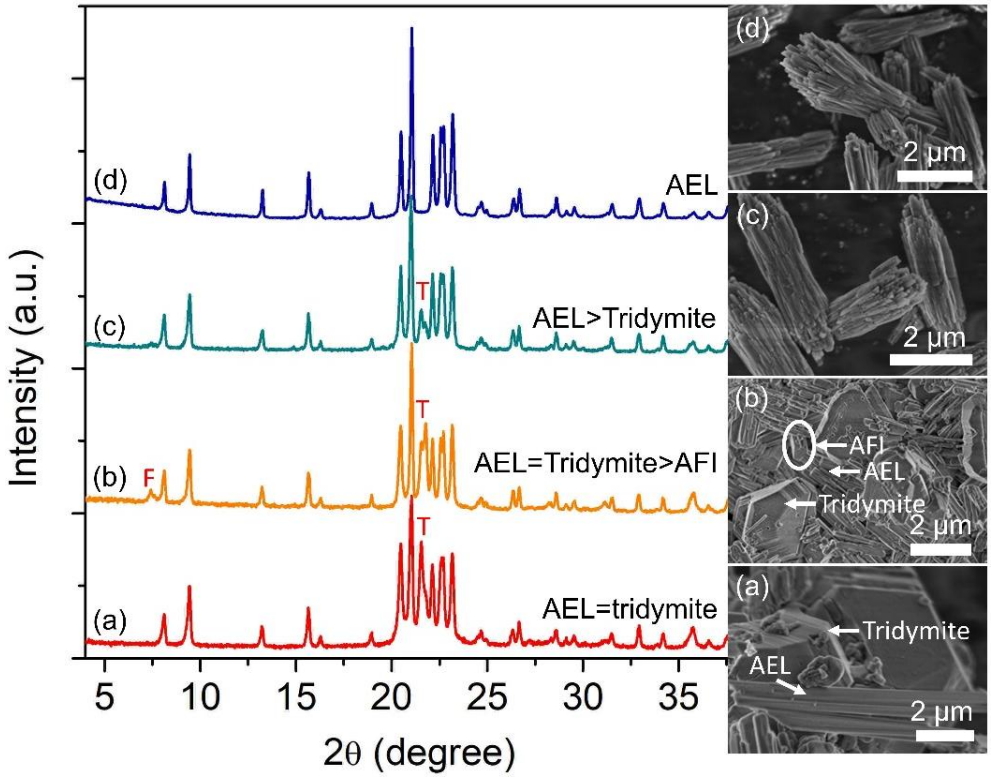

Figure 4.7 XRD patterns and FESEM micrographs of (a) E-11 (y = 0), (b) E-12 (y = 0.4), (c) E-13 (y = 0.9) and (d) E-3 (y = 1.3) samples. The samples were prepared using the ionogel of 1.0Al: 1.8P: ySi: 38[PPy]Br heated at 150 °C for 133 h. F and T denote the presence of AFI and tridymite crystalline phases, respectively

4.3.4 Effect of [PPy]Br content

An ionic liquid is essential for controlling the concentration of raw chemicals besides serving as a solvent for the ionothermal synthesis of zeolite (Morris, 2009). Simultaneously, it also acts as a potent structure-directing agent in the formation of zeolites. Hence, the precursor mixture of 1.0Al: 1.8P: 0.3Si: z[PPy]Br (z = 14, 22, 30

and 38) was heated at 150 °C for 133 h in order to investigate the effects of [PPy]Br on the crystal evolution of SAPO-11. When z = 14, the tridymite dense phase tends to be crystallized as the major crystalline product with SAPO-5 (AFI) and SAPO-11 (AEL) as minor phases (E-14, Figure 4.8a). According to Basina et al., an insufficient amount of ionic liquid may cause slow and inefficient dissolution of inorganic reactants, affecting the equilibrium concentration for initiating the nucleation of zeolite crystals (Basina et al., 2018). If the [PPy]Br content is increased to z = 22 or 30, it allows better dissolution of reactants, resulting in the favored crystallization of SAPO-11 over tridymite (E-14, Figure 4.8b,c). The optimum [PPy]Br content is found to be z = 38, when pure SAPO-11 solid is obtained. Hence, besides serving as solvent, [PPy]Br also plays a structure-directing role and a charge-balancing role in stabilizing the micropore channel system of SAPO-11 (Oh et al., 2018).

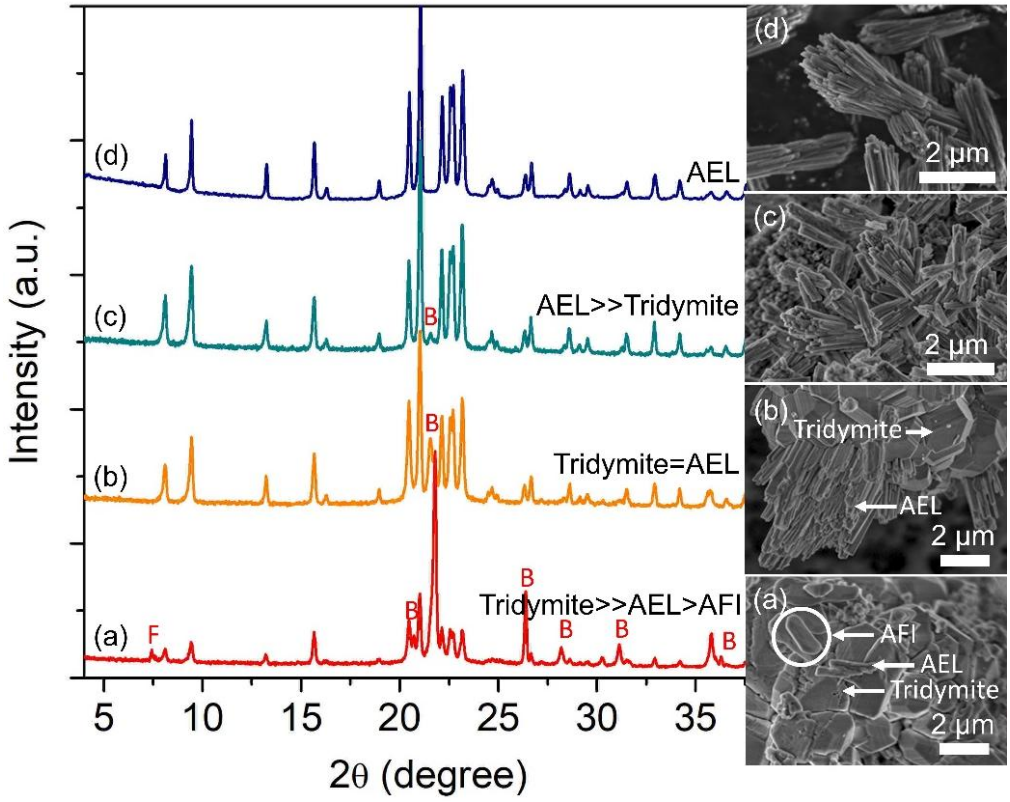

Figure 4.8 XRD patterns and FESEM micrographs of (a) E-14 (z = 14), (b) E-15 (z = 22), (c) E-16 (z = 30) and (d) E-3 (z = 38) samples. The samples were prepared using the ionogel of 1.0Al: 1.8P: 0.3Si: z[PPy]Br heated at 150 °C for 133 h. F and B denote the presence of AFI and berlinite crystalline phases, respectively

4.4 Pore stabilization and confinement roles of [PPy]Br in SAPO-11

Thermogravimetry analysis can reveal the roles of [PPy]Br in stabilizing the AEL framework and the strength of this supramolecule's interaction with the SAPO-11 pore channel system.

In this regard, TGA/DTG data of pure [PPy]Br ionic salt and as-synthesized SAPO-11 (E-3) that contains occluded [PPy]Br were recorded. The free [PPy]Br exhibits one-step weight loss (96.5%) at 190–300 °C due to the decomposition of ionic liquid (Figure 4.9a) (Maton et al., 2013). In contrast, the non-calcined SAPO-11 displays three steps of weight loss. The first weight-loss step (0.6%), at <170 °C, is due to the desorption of water from the surface of SAPO-11 (Tosheva et al., 2008). Whereas the second (3.0%, 170–320 °C) and third (3.8%, 320–450 °C) steps of weight

loss are attributed to the decomposition of the ionic liquid molecules (Soulard et al., 1991). As calculated, the $[PPy]^+/TO_2$ (T = Si, Al or P) molar ratio of as-synthesized SAPO-11 is 0.036, which corresponds to ca. 28 TO_2 primary building units enfolding one $[PPy]^+$ organic cation in a three-dimensional manner. In addition, the weight loss of organic moiety occurs at a higher temperature due to strong interaction and confinement effects of the [PPy]Br molecule in the micropores. As a result, the trapped [PPy]Br requires a longer time and higher temperature to escape from the SAPO-11 pore channels (Ng et al., 2009). Hence, it is revealed that the encapsulation of $[PPy]^+$ follows the "ship in a bottle" approach, whereby TO_2 primary building units form oligomers and then polymers around the $[PPy]^+$ (4.33 Å× 7.93 Å× 2.54 Å) (Ishii et al., 2011). before the organic cation is tightly wrapped and confined in the pores forming a pore size diameter of 4.63 Å.

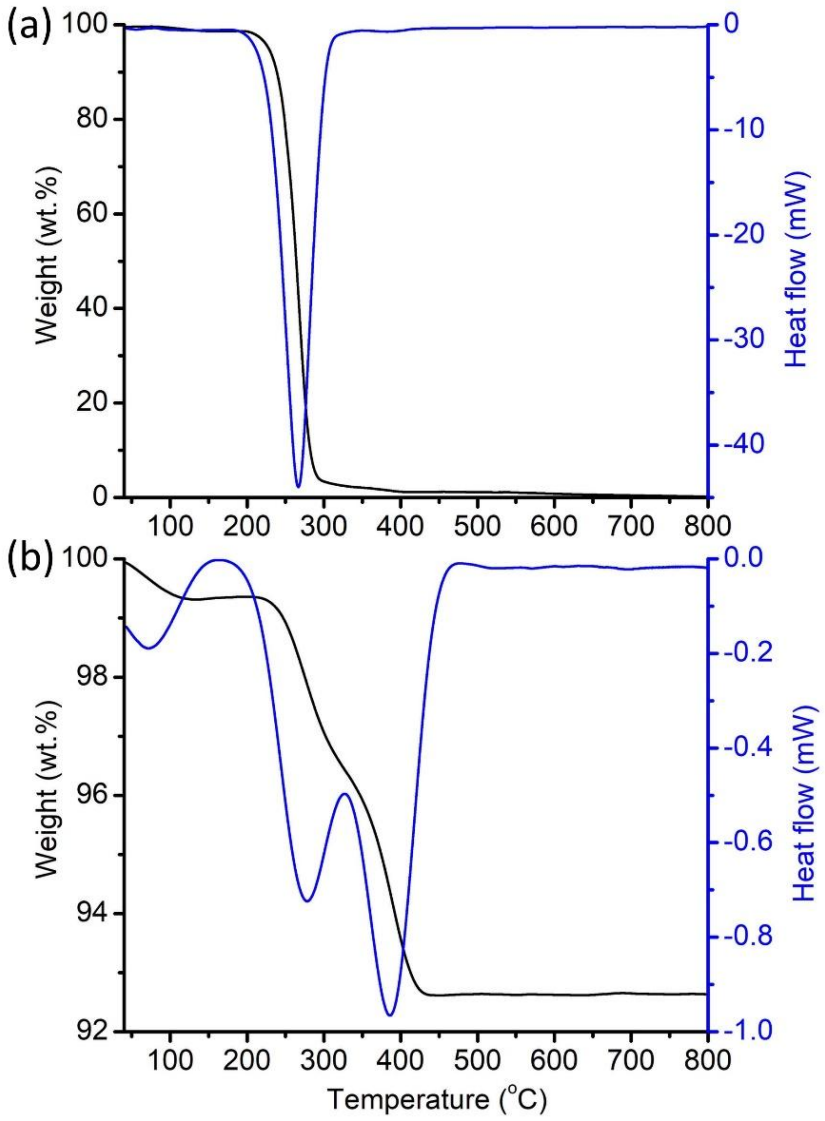

Figure 4.9 TGA/DTG curves of (a) free [PPy]Br ionic salt and (b) as–synthesized SAPO-11 (E-3)

The ^{13}C NMR spectroscopy also shows that the [PPy]Br is intact after being trapped inside the SAPO-11 micropores; all NMR peaks due to [PPy]Br molecules are shown in the as-synthesized SAPO-11 (Figure 4.10b). In this sample, the NMR peaks of ionic liquid molecules (especially C1, C3 and C6) also experience chemical shifts compared with their free counterpart (Figure 4.10a). Furthermore, their resonance bands are also broadened, indicating strong molecule-wall interaction and geometric constraints in confined space that disallow molecular movement inside SAPO-11 micropores (Adam et al., 2013). Thus, the thermogravimetry and NMR data further

confirm the stabilizing and pore-filling effect roles of [PPy]Br during the crystallization of SAPO-11.

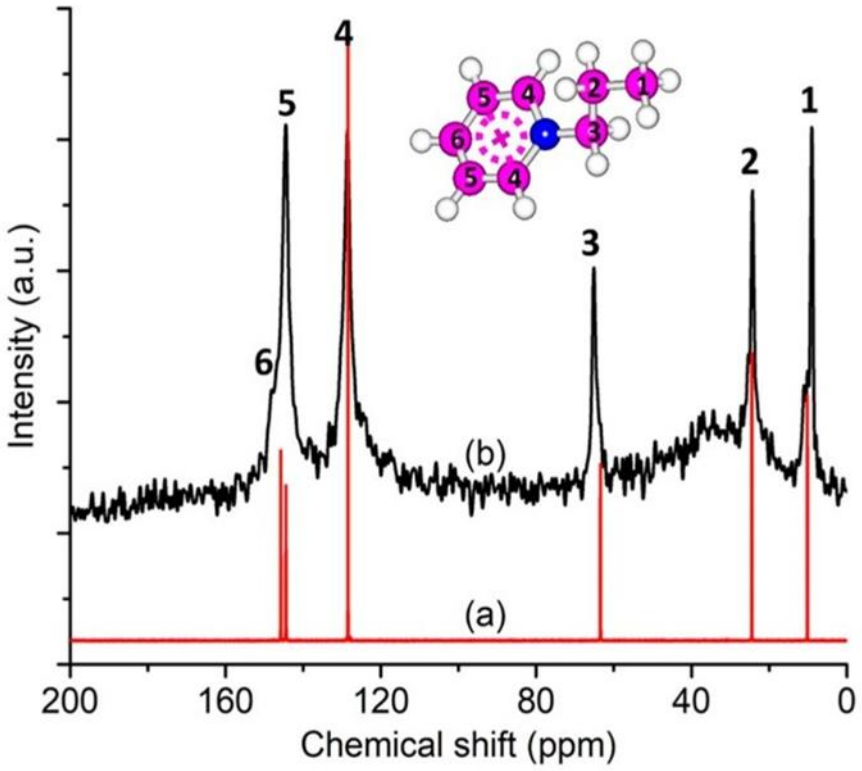

Figure 4.10 (a) Liquid state NMR spectrum of [PPy]Br ionic molten salt, and (b) solid state MAS NMR spectrum of as-synthesized SAPO-11 (E-3)

4.5 Porous and acid properties of [PPy]Br synthesized SAPO-11

The purity, crystallinity and catalytic performance of SAPO-11 are directly related to its porous properties, and hence, nitrogen adsorption–desorption analysis was performed on the calcined SAPO-11 at -196 °C. The N_2 adsorption–desorption curves of SAPO-11 display type I adsorption isotherm due to its high microporous characteristics (S_{Mic} = 110 m^2 g^{-1}) with some N_2 uptake at high P/P_o, confirming its secondary textural mesoporosity (Table 4.2, Figure 4.11 and inset) (Sing, 1985). The sample also shows a considerably high surface area (S_{BET} = 149 m^2 g^{-1}, S_{Mic} = 110 m^2 g^{-1}), high total pore volume (V_{tot} = 0.24 cm^3 g^{-1}) and large average pore diameter (d_p = 29.5 nm) where primary micropores and secondary textural mesopores are considered, whereby its porosity is comparable with the SAPO-11 synthesized using

dipropylamine under hydrothermal conditions (S_{BET} = 100 m^2 g^{-1}, S_{Mic} = 50 m^2 g^{-1}, V_{tot} = 0.15 cm^3 g^{-1}) (Lima et al., 2021).

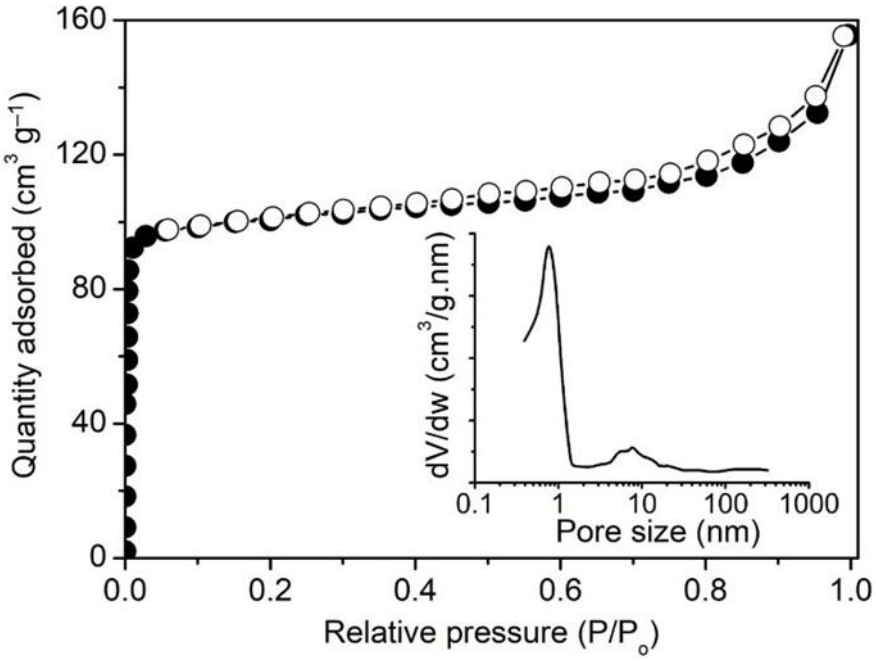

Figure 4.11 Nitrogen adsorption (close symbols) and desorption (open symbols) isotherms and (inset) pore size distribution of calcined SAPO-11 (E-3) sample at -196 °C

Table 4.2 Surface acidity of SAPO-11 calculated using pyridine-IR spectroscopy method. B = Brønsted acid sites and L = Lewis acid sites

Sample	Total acidity (150 °C) (μmol g^{-1})			Medium to strong acidity (300 °C) (μmol g^{-1})		
	B	L	B+L	B	L	B+L
SAPO-11	136	158	294	61	40	101

FTIR spectroscopy investigation of pyridine adsorption is one of the most popular methods for characterizing the surface acidity. The study of the framework acidity (type, amount and strength) is based on the bonding strength of the N nucleophile group of pyridine to the acid sites of SAPO-11 (Si species) (Choo et al., 2020). The FTIR spectra of pyridine adsorbed SAPO-11 after desorption at 150 and 300 °C are shown (Figure 4.12). In general, the SAPO-11 contains both Lewis and

Brønsted acidities, based on the IR bands at 1455 and 1545 cm^{-1}, respectively. The Lewis acid sites (158 µmol g^{-1}), which come from structural defects after calcination, are higher than the Brønsted acid sites (136 µmol g^{-1}) (Table 4.2, Figure 4.12) (Shuit et al., 2015). The quantity of acidity of SAPO-11 at 300 °C is also determined where it can distinguish the strength of acid sites. It can be seen that some IR bands are still retained, indicating the presence of medium-to-strong Lewis (40 µmol g^{-1}) and Brønsted (61 µmol g^{-1}) acid sites in the solid. Hence, the results show that the synthesized SAPO-11 is a mild-to-strong acid solid catalyst with a total acidity slightly higher than that of the conventional SAPO-11 (Alfonzo et al., 1995).

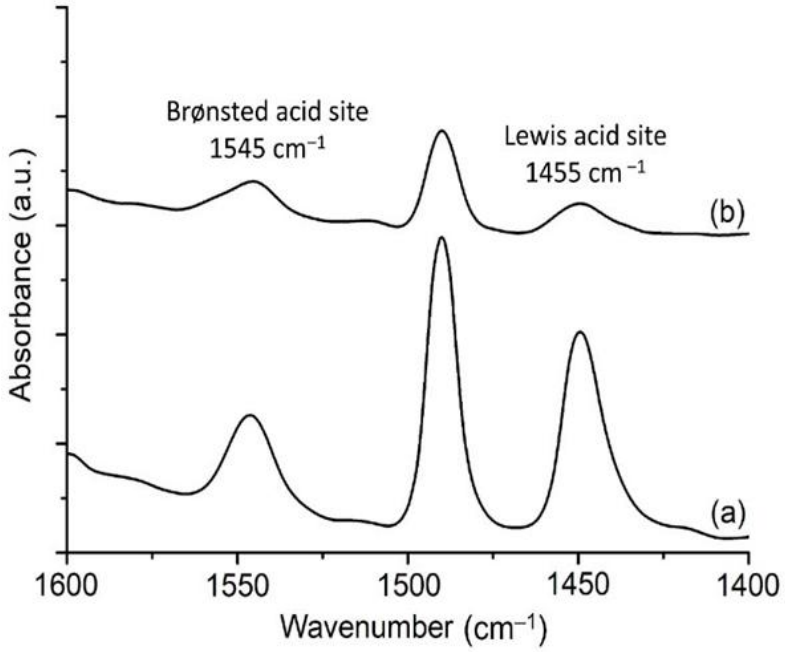

Figure 4.12 IR spectra of pyridine adsorption after desorption at (a) 150 °C and (b) 300 °C

CHAPTER 5

FORMATION MECHANISM OF PYRIDINIUM-TEMPLATED SAPO-5 ZEOLITES USING DIFFERENT PHOSPHORUS SOURCES

5.1 Characterization of 5-ethyl-2-methyl-1-propylpyridinium salts

The FTIR spectrum of [empy]Br is first characterized with several techniques prior converting into [empy]OH. First the [empy]Br is analyzed with IR spectroscopy (Figure 5.1). The absorption bands at 712 and 776 cm^{-1} are attributed to the bending rocking of aromatic C-H and vibrations of CH_3 groups, respectively. The stretching of C-N and the aromatic C-N of pyridine ring are respectively found at 1213 and 1307 cm^{-1}, respectively. The absorption bands at 1396 and 1446 cm^{-1} are dedicated to C-H bending vibrations whereas the C=N and C=C stretching can be confirmed by the bands at 1534 and 1641 cm^{-1}, respectively. Furthermore, the absorption band at 2872 and 2970 cm^{-1} are due to the Csp^3-H and Csp^2-H stretching modes. The O-H stretching of the adsorbed water molecules is recorded at 3410 cm^{-1}.

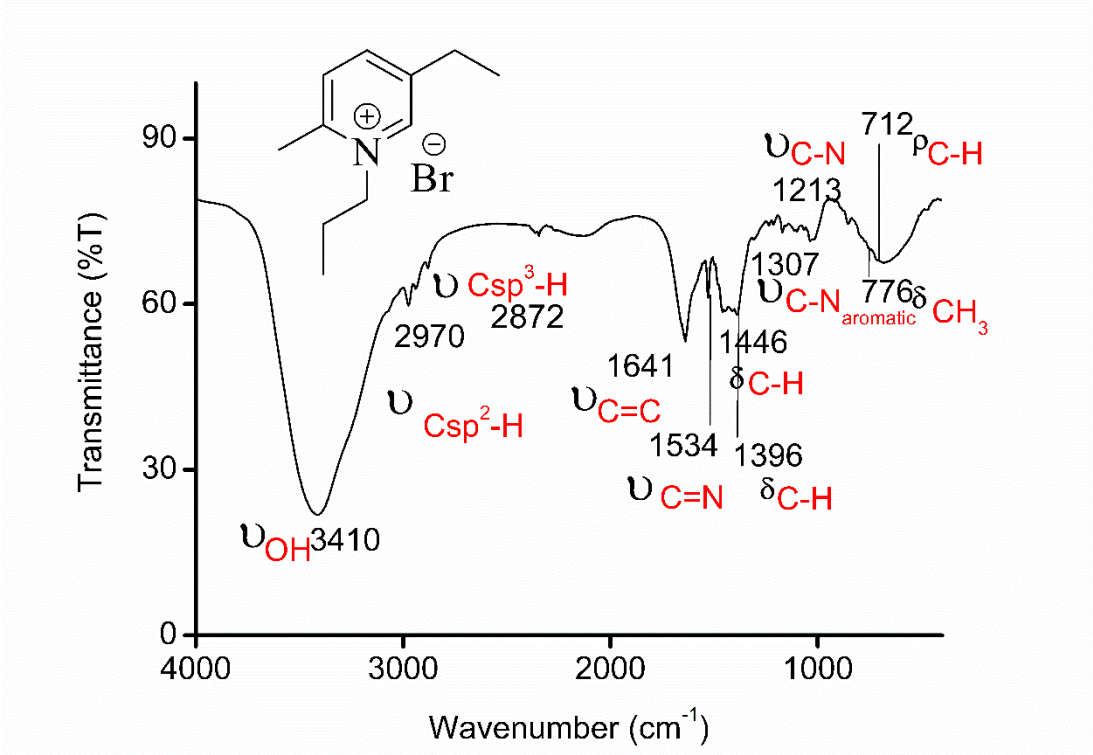

Figure 5.1 FT-IR spectrum of [empy]Br

Second, the [empy]Br ionic salt is analyzed with ^{1}H NMR spectroscopy to verify its purity. Figure 5.2 shows a total of nine peaks in the ^{1}H NMR spectrum which correspond to distinct types of hydrogens present in the ionic compound: δ = 0.95 triplet (3H, Pyridine N-CH_2-CH_2-CH_3), 1.22 triplet (3H, Pyridine N-CH_2-C-CH_3), 1.92 multiplet (2H, Pyridine N-CH_2-CH_2), 2.69 singlet (2H, Pyridine N-CH-C-CH_2), 2.97 singlet (3H, Pyridine N-C-CH_3), 4.46 triplet (2H, Pyridine N-CH_2), 7.82 duplet (1H, Pyridine N-C-CH-CH), 8.22 triplet (1H, Pyridine N-C-CH), 8.64 triplet (1H, Pyridine N-CH). The spectrum is free from the contamination of other compounds, proving that the [empy]Br has very high purity.

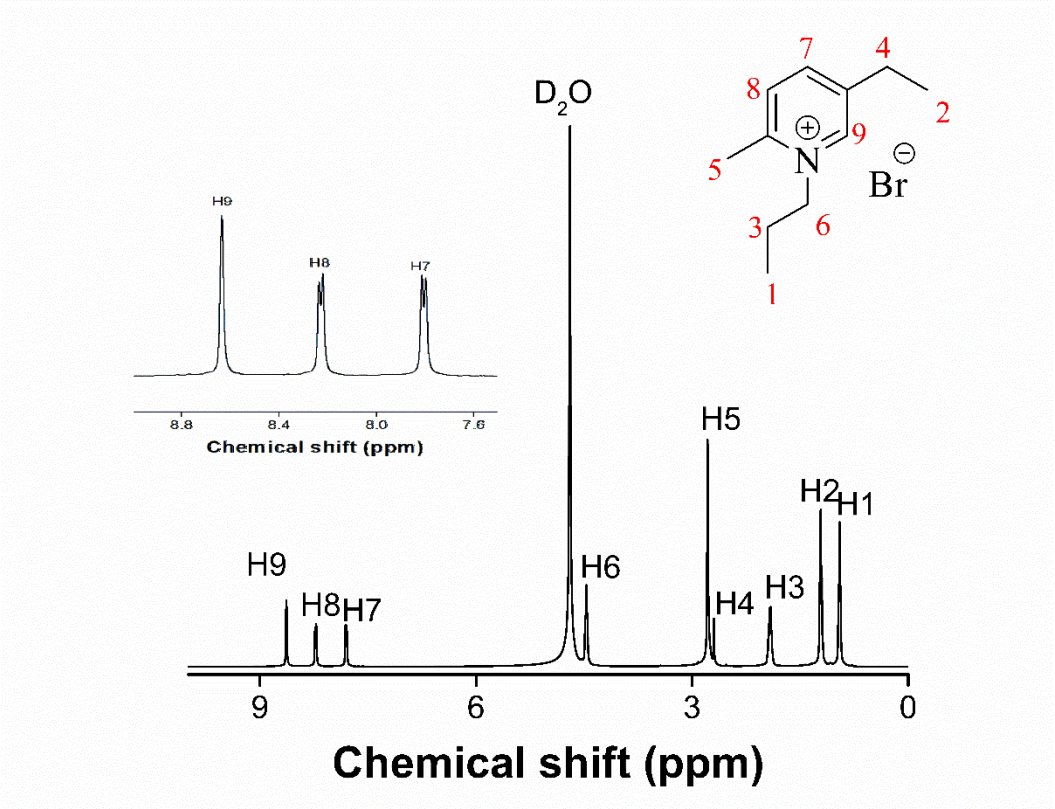

Figure 5.2 ^{1}H NMR spectrum of [empy]Br

After the IR and ^{1}H NMR spectroscopy characterizations, the pure [empy]Br is converted into [empy]OH *via* OH^- ion exchange technique using the protocol mentioned in Section 3.4. The resulting [empy]OH template solution is then used to prepare SAPO-5 where H_3PO_4 and $H_4P_2O_7$ are used as the phosphorus sources. Both SAPO-5 samples at different time intervals (H_3PO_4: PA-*n*; $H_4P_2O_7$: PyP-*n* where *n* is heating time in hour) are withdrawn and characterized according to the analyses mentioned in Section 3.6.

5.2 Crystallization study of SAPO-5

The crystallization of SAPO-5 using different P sources, namely H_3PO_4 and $H_4P_2O_7$, in the presence of [empy]OH template is performed since the P source plays very important roles not only in controlling the product purity, but also alters the crystallization kinetics, crystallinity, morphology, porosity, etc. (Kadja et al., 2017; Lodrijeh et al., 2021; Wong et al., 2017). First, visual observation on initial precursors

is carried out since the physical state of the precursor can give a preliminary information on the ultimate products formed. White suspension containing solid precipitate (pH 5.09) with strong release of air bubbles is observed during the addition of H_3PO_4 indicating the occurrence of hydrolysis of aluminum isopropoxide (Figure 5.3). In contrast, a clear precursor solution (pH 5.39) with no bubble release is obtained upon adding $H_4P_2O_7$ indicating slow hydrolysis rate. Both precursors are then subjected to hydrothermal treatment where the PA-n precursor forms a mixture containing precipitate solids and cloudy upper layer. The separation of both zeolite solid and liquid layers becomes more significant with time and the pH of the mixture gradually decreases from 5.08 to 4.21 (Figure 5.3a). In contrast, the clear PyP-n precursor solution slowly transforms into a colloidally stable white suspension and the pH of the colloidal suspension also reduces from 5.36 to 4.60 after 5 h, signifying that nanoparticles have been formed (Figure 5.3b).

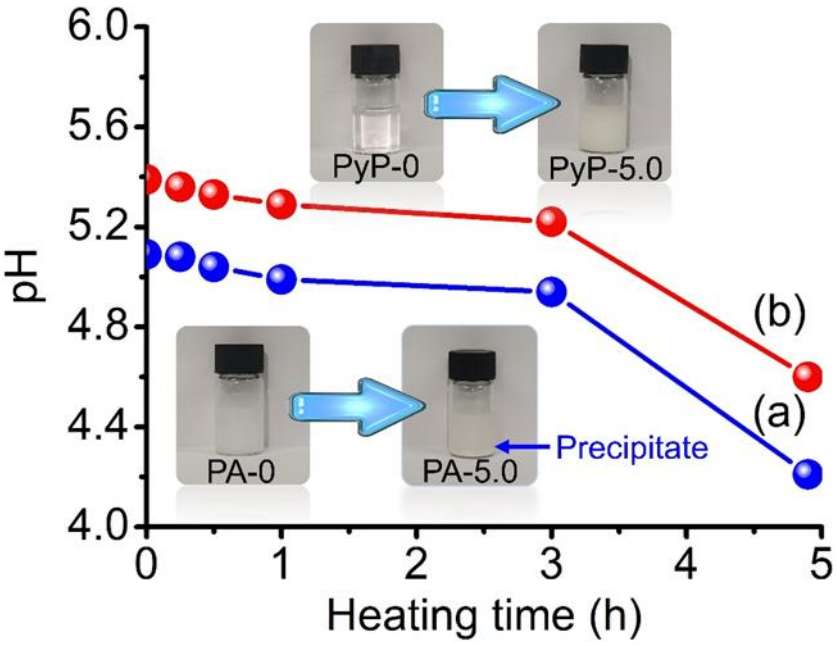

Figure 5.3 pH evolution as a function of time and photographs of precursor mixtures of samples (a) PA-0 to PA-5.0 and (b) PyP-0 to PyP-5.0

The XRD patterns of both PA-*n* and PyP-*n* samples are presented in Figures 5.4a and 5.4b, respectively. Amorphous materials are first formed within 0.2 h and SAPO-5 starts to crystallize with different rates under increasing the heating time (Figure 5.4c). For instance, PA-0.5 achieves 53% of crystallinity and its crystallization rate is faster than that of PyP-0.5 (23% of crystallinity). Upon further heating to 5 h, PA-5.0 achieves 100% of crystallinity while PyP-5.0 has 87% crystallinity. Thus, the XRD data suggests that the H_3PO_4 produces more reactive hydrogel that leads to fast crystallization as compared to $H_4P_2O_7$. Meanwhile, no other crystalline phase is formed together with SAPO-5, indicating that [empy]OH is very selective in crystallizing SAPO-5 molecular sieves. With further increasing the crystallization time to 6 h, dense tridymite phase starts to co-crystallize with SAPO-5 synthesized using H_3PO_4 (Figure 5.5). Meanwhile, dense crystalline phase is also formed after 5 h of hydrothermal synthesis when no [empy]OH template is added indicating the essential impact of [empy]OH in directing the formation of SAPO-5 (Figure 5.6).

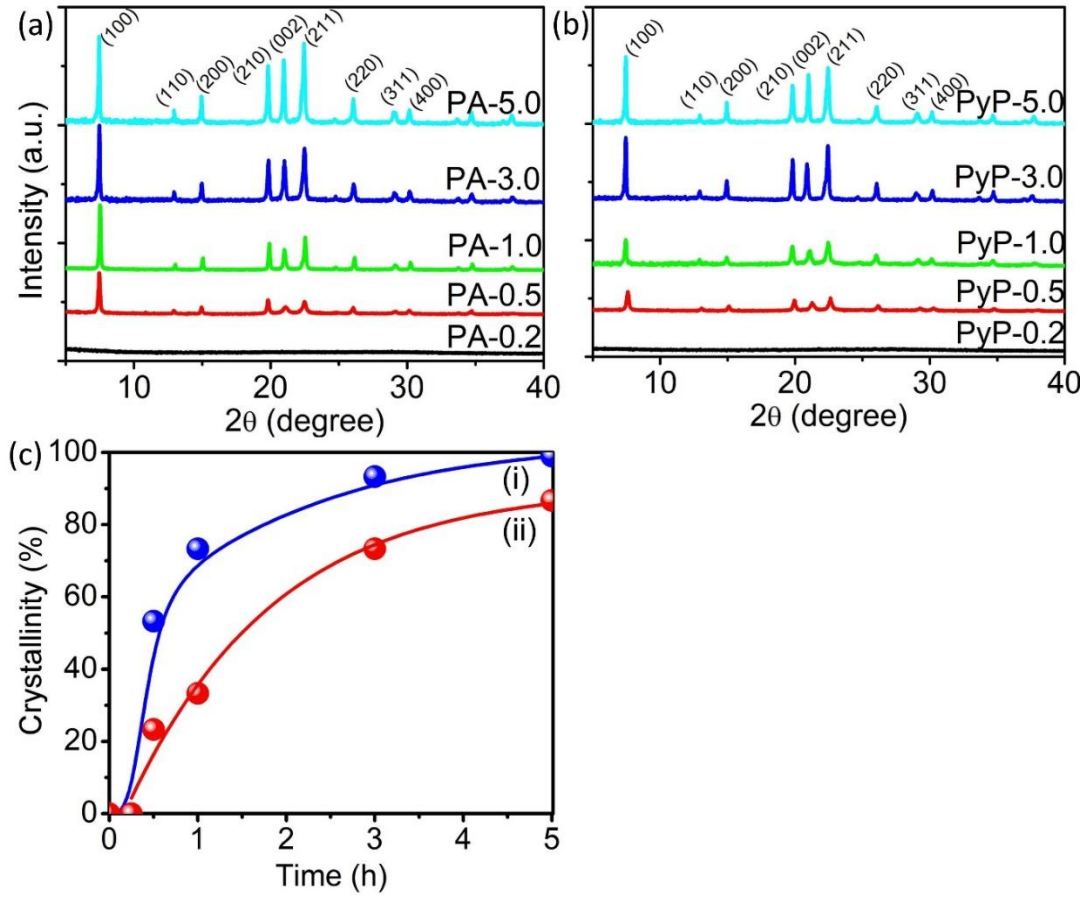

Figure 5.4 A series of XRD patterns of SAPO-5 samples prepared using (a) H_3PO_4 and (b) $H_4P_2O_7$ after various hours of hydrothermal treatment while (c) shows the sigmoidal plots of crystallinity versus heating time of samples prepared using (i) H_3PO_4 and (ii) $H_4P_2O_7$

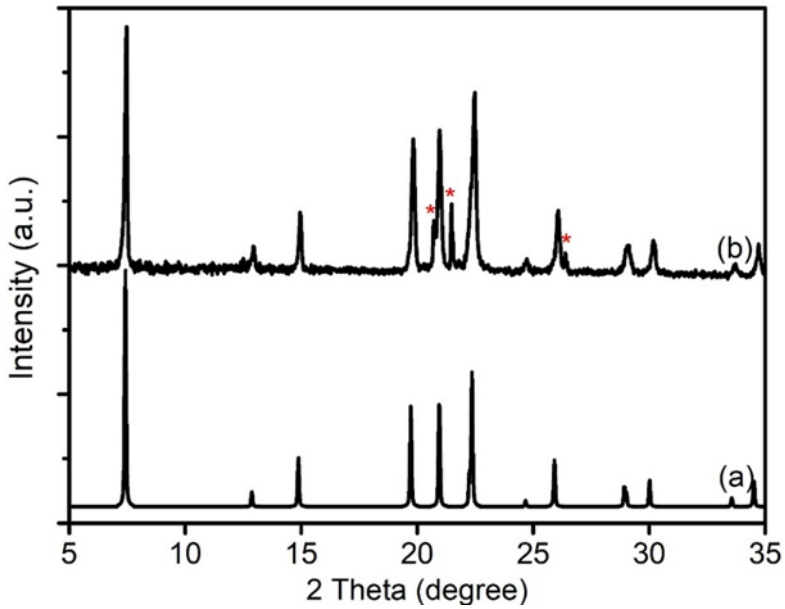

Figure 5.5 XRD patterns of (a) simulated and (b) PA-6.0. The asterisks show the presence of co-crystallized tridymite competing phase

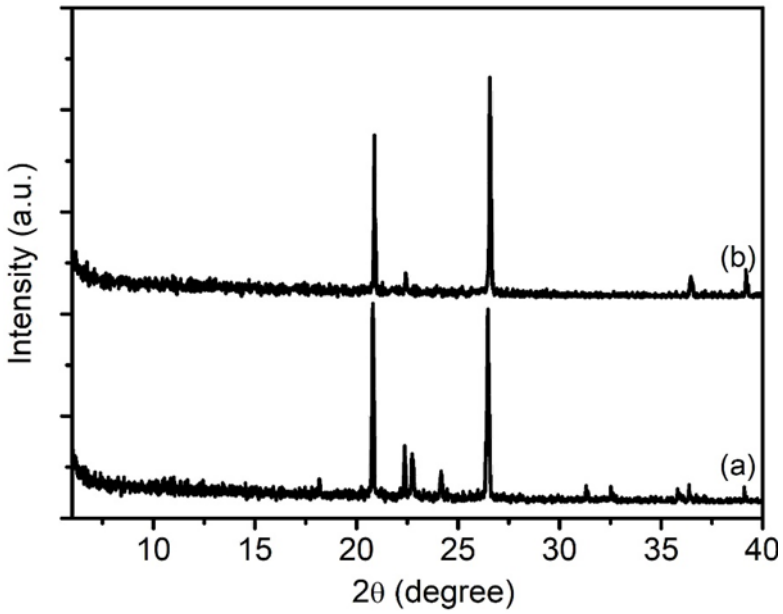

Figure 5.6 XRD patterns of samples synthesized using (a) H_3PO_4 and (b) $H_4P_2O_7$ as P sources without [empy]OH template after 5 h of hydrothermal treatment

The crystallization process of SAPO-5 is also followed using IR spectroscopy (Ma et al., 2021). The initial PA-0.2 and PyP-0.2 samples show no IR band in the zeolite fingerprint region (500−750 cm^{-1}) confirming their amorphous nature (Figure 7a,b) (Souissi et al., 2018). When the synthesis time is increased to 0.5 h, in both PA-0.5 and PyP-0.5 samples an increase peak intensity at 472 cm^{-1} (due to TO_4 bending where T = Al, P or Si) at the expense of the peak at 787 cm^{-1} (Si−O−T bridge) is observed (Souissi et al., 2018). Additionally, two IR bands at 742 and 559 cm^{-1} assigning to the *bog* and *t-afi* secondary building units of AFI, respectively, start to appear in PA-0.5. It agrees with the XRD data that reveals the fast formation of SAPO-5 framework structure (or nuclei) (Figure 5.4a). With time increasing to 5 h, these two AFI characteristic peaks slightly shift and are becoming more resolved indicating that amorphous entities are gradually transformed into crystalline SAPO-5 material in both samples. Concurrently, the wavenumbers of peaks for both PA-5.0 and PyP-5.0 samples at around 1225 cm^{-1} (Si−O−T stretching) and 1110 cm^{-1} (asymmetric O−P−O stretching) are different suggesting different chemical compositions (Si, Al and

P) of the framework structure and confinement configuration of the template molecules in SAPO-5 samples (Ma et al., 2022; Shannon, 1976).

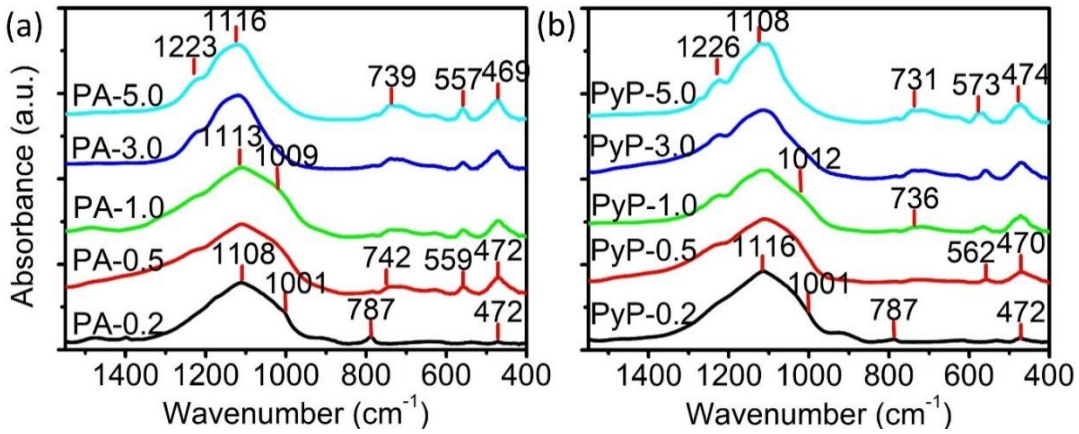

Figure 5.7 IR spectra of samples prepared using (a) H_3PO_4, and (b) $H_4P_2O_7$ acids after various hydrothermal heating time at 180 °C

The interaction between $[empy]^+$ and SAPO solids is investigated using TGA/DTG analysis. Based on the TGA/DTG data, both PA-*n* and PyP-*n* samples series generally display three steps of weight loss due to different amounts of adsorbed water and occluded $[empy]^+$ template (Figure 5.8, Table 5.1) (Ng et al., 2008). With increasing the crystallization time, the amount of occluded $[empy]^+$ increases in the expense of the amount of water adsorbed. This can be observed in the case of PA-5.0 when it experiences transformation of amorphous into fully crystalline SAPO-5 (Figure 5.4a). As a result, more water is released from the PA-5.0 (<200 °C) to allow the inclusion of $[empy]^+$ (7.8 wt%) in the micropores of SAPO-5 (200−630 °C) (Figure 5.8a,b). Similar trend is also observed by PyP-5.0 but with lower amount of occluded $[empy]^+$ (5.8 wt%) (Figure 5.8c,d) (Chen et al., 2020).

The direct relation between the amount of occluded $[empy]^+$ with the crystallinity of SAPO-5 is further investigated by constructing a linear plot where a fairly strong correlation between both variables is shown (R^2 >0.86) (Figure 5.9). From the linear plots, it is observed that PA-0.2 requires higher amount of $[empy]^+$

(31.0 mmol g^{-1}) to initiate crystallization as compared to PyP-0.2 (27.4 mmol g^{-1}). In addition, more $[empy]^+$ is also needed by the PA-*n* precursor to achieve the same crystallinity compared with PyP-*n*. Thus, based on the visual observation on products obtained (solid precipitate for PA-5.0 and colloidal suspension for PyP-5.0), it is suggested that PA-5.0 would have larger crystal size which confined more $[empy]^+$ cations, whereby larger amount of $[empy]^+$ is used for crystal growth instead of nucleation. As a result, high crystallinity proportionates to high amount of occluded $[empy]^+$ is observed. In addition, it is calculated that one $[empy]^+$ molecule is packed by approximately 33 and 42 TO_4 (T = Si, Al or P) tetrahedral primary units in PA-5.0 and PyP-5.0, respectively (Yang et al., 2020). This indicates that the $[empy]^+$ is loosely enfolded within the pores of PA-5.0 which indirectly reveals its hierarchical micro/mesoporosity with more pore opening that will be discussed in the nitrogen adsorption-desorption study.

Table 5.1 Weight losses of PA-*n* and PyP-*n* samples at different ranges of temperature calculated from TGA/DTG data

Samples	**<200 °C**	**200−630 °C**	**>630 °C**
PA-0.2	15.4	5.1	79.5
PA-0.5	10.9	5.7	83.4
PA-1.0	6.2	6.5	87.3
PA-3.0	5.7	6.9	87.4
PA-5.0	4.3	7.3	88.4
PyP-0.2	16.8	4.5	78.7
PyP-0.5	9.1	4.9	86.0
PyP-1.0	6.9	5.4	87.7
PyP-3.0	6.7	6.1	87.2

PyP-5.0	2.7	5.8	91.5

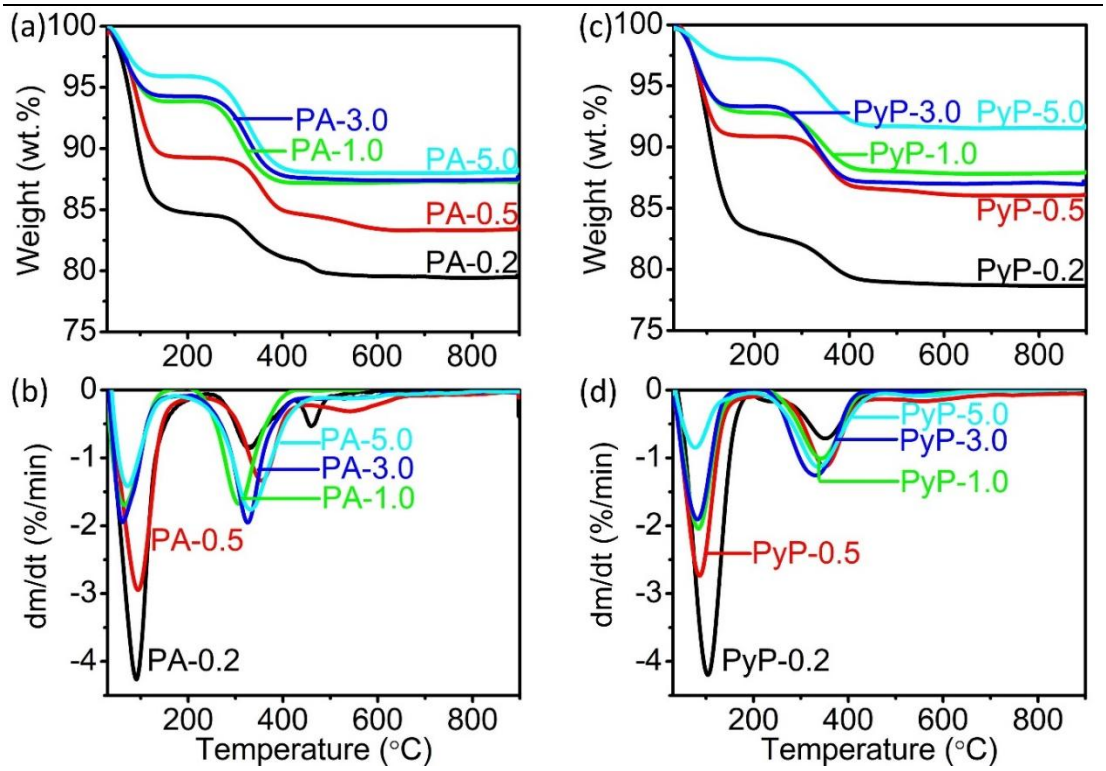

Figure 5.8 TGA and DTG profiles of samples prepared using (a, b) H_3PO_4 and (c, d) $H_4P_2O_7$ after various hours of hydrothermal treatment, respectively

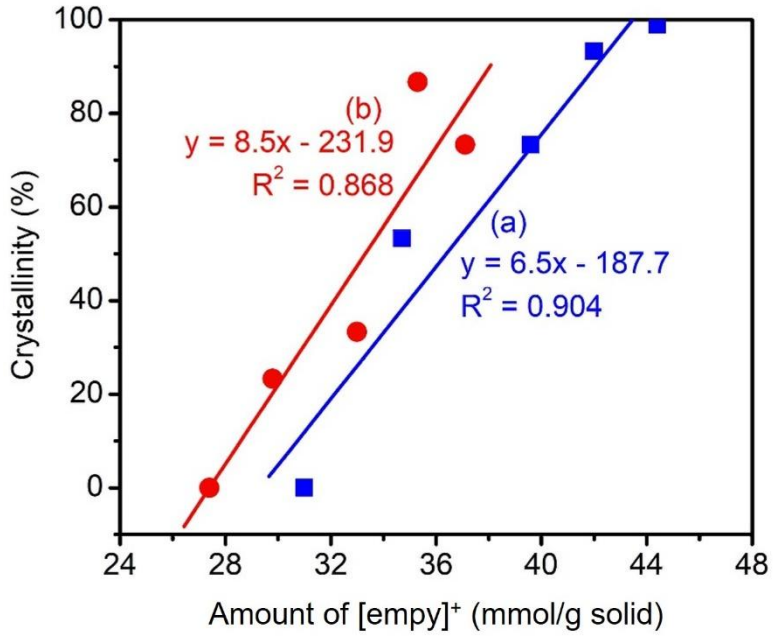

Figure 5.9 A plot of crystallinity versus amount of occluded $[empy]^+$ derived from XRD and TGA/DTG data of (a) PA-*n* and (b) PyP-*n* samples

The resulting PA-5.0 and PyP-5.0 SAPO-5 solids are further characterized with ^{27}Al MAS NMR spectroscopy. Both SAPO-5 samples display three ^{27}Al signals at approx. 38, 10 and -11 ppm (Figure 5.10). The first peak is originated from the tetrahedral framework Al (Al_{tetra}) species while the second peak is ascribed to the penta-coordinated Al (Al_{penta}) formed upon water adsorption (Ng et al., 2010). The peak at -11 ppm corresponds to the octahedral extraframework Al (Al_{octa}, EFAL) atoms due to defect sites. The position of the peaks corresponding to these Al species for PA-5.0 are slightly shifted compared to those of PyP-5.0 due to the different chemical environments of these Al units in the solids. PA-5.0 also shows significant quadrupolar broadening compared to PyP-5.0 indicating it has more distorted Al than PA-5.0 which shows sharper and more symmetry peaks (Gackowski et al., 2019). Additionally, a noticeable intense peak due to EFAL is also present in the spectrum of sample PA-5.0 at -11.5 ppm compared to PyP-5.0 (Wang et al., 2022). Thus, the presence of intense peak of EFAL indicates that PA-5.0 has larger amount of Lewis acid sites than PyP-5.0 besides the presence of Brønsted acid sites originated from the tetrahedral Al atoms (Xiang et al., 2024).

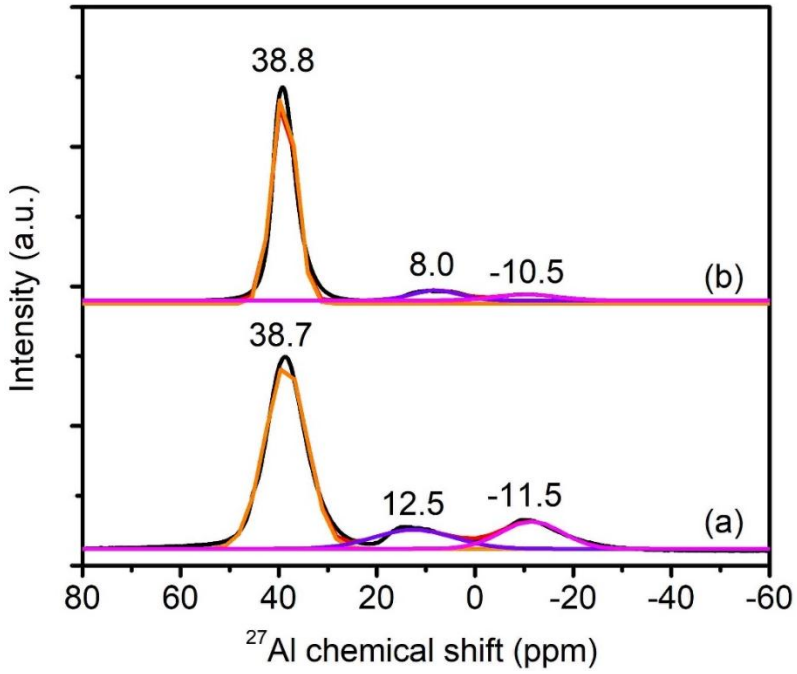

Figure 5.10 ^{27}Al MAS NMR spectra of samples (a) PA-5.0 and (b) PyP-5.0

Meanwhile, down-field ^{31}P NMR chemical shifting is detected in PyP-5.0 due to strong interaction (deshielding) between tetrahedral P sites and the framework Al (Figure 5.11). As seen in this sample, the peak at -30.2 ppm arising from the tetrahedral P species in SAPO-5 framework is broad. This demonstrates that the framework P atoms in the PyP-5.0 sample has more complex coordination environment than that in the PA-5.0 sample (Bing et al., 2013). Also, the ^{31}P peak of PyP-5.0 at -22.0 ppm is slightly broadened, indicating the presence of larger amount of amorphous silicoaluminophosphate left in the sample, and it is in line with the XRD observation that the PyP-5.0 SAPO-5 has lower crystallinity than its counterpart (Figure 5.4) (Wang et al., 2021).

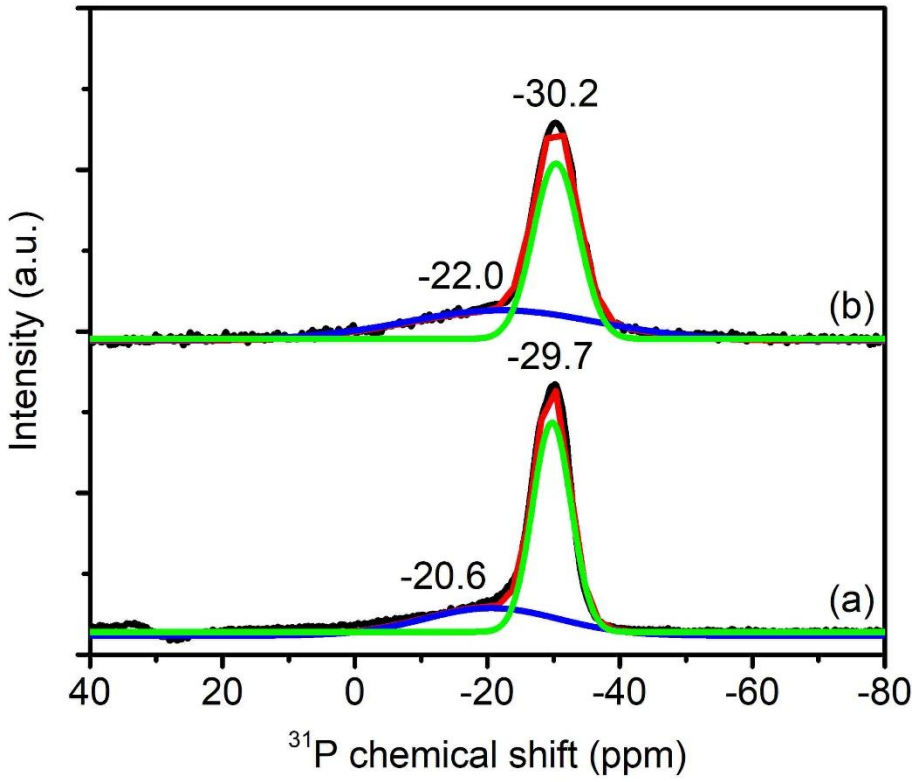

Figure 5.11 ^{31}P MAS NMR spectra of samples (a) PA-5.0 and (b) PyP-5.0

The elemental chemical compositions of fully crystalline samples PA-5.0 and PyP-5.0 SAPO-5 templated by [empy]OH are also determined. The chemical composition of PA-5.0 expressed as a molecular formula is $Al_{10.5}Si_{2.6}P_{10.9}O_{48}$, while for PyP-5.0 is $Al_{11.3}Si_{1.2}P_{11.7}O_{48}$ based on the XRF spectroscopy data; the Si/(Al+P) ratios for both samples is in the usual range for SAPO-5 material (0.06 to 0.18) (Kosslick & Fricke, 2006; Potter, 2020). As shown, the Si/(Al+P) ratio of sample PA-5.0 (0.12) is higher than that of PyP-5.0 (0.06) indicating that PA-5.0 has more Si incorporated into the AFI framework, which indirectly also contributes to higher surface acidity (Potter, 2020).

The morphology of crystals in samples PA-5.0 and PyP-5.0 was studied by FESEM. It is shown that the use of different P sources has profound effect on the morphology of SAPO-5. The PA-5.0 sample exhibits classical hexagonal cylindrical crystals with an average size of 1.1 × 0.4 μm^2 (Figure 5.12a–c). Interestingly, the

surface of crystals is rough and some crystals are found to have defective hollows on the surface, revealing the mesoporous feature. On the other hand, sample PyP-5.0 shows different morphological feature. As seen, the crystals prone to grow in x- and y-directions rather than in z-direction, producing hexagonal-shaped SAPO-5 nanoplates with a narrow particle size distribution centred at 180 nm (Figure 5.12d−f). The surface is smooth and no mesopores can be seen from the surface of SAPO-5 nanoplates. Considering the TG/DTG findings on the relation of crystallinity and $[empy]^+$ with FESEM data, it can hence be concluded that $H_4P_2O_7$ is beneficial in promoting nucleation over crystal growth of SAPO-5.

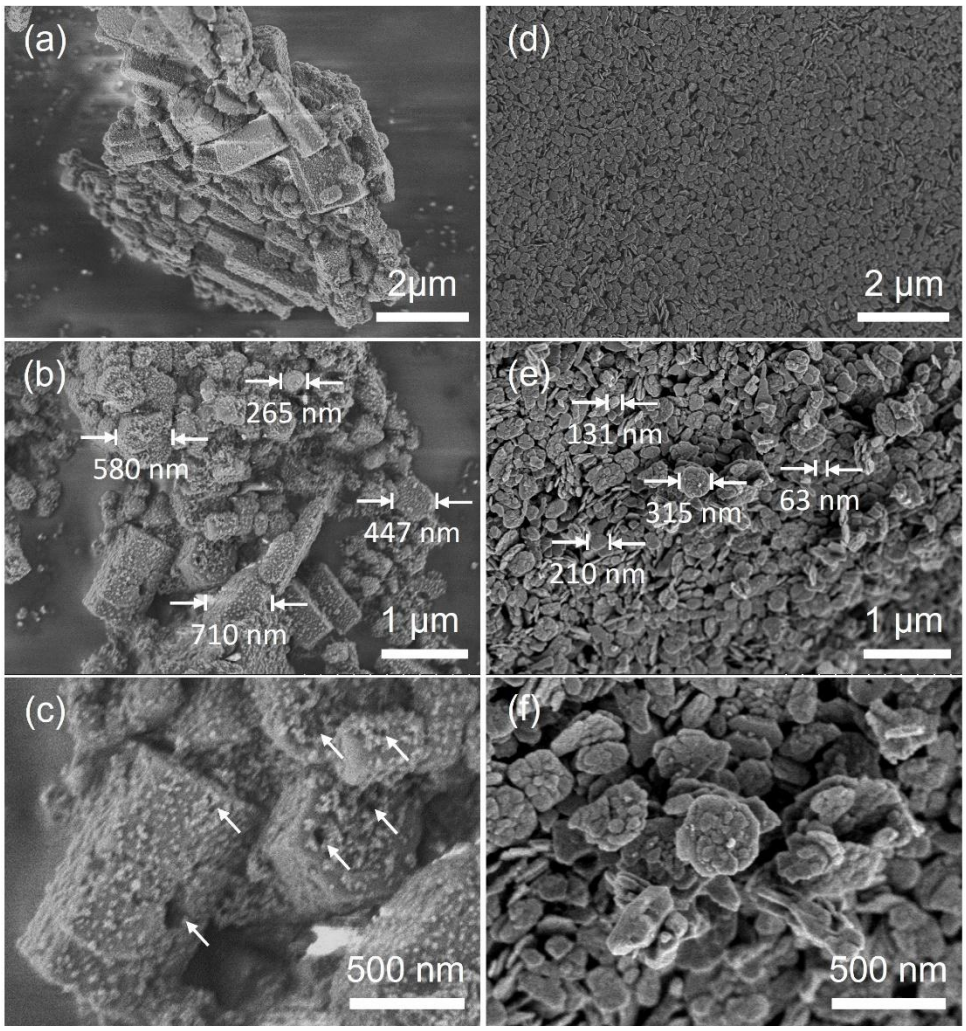

Figure 5.12 FESEM images of samples (a−c) PA-5.0 and (d−f) PyP-5.0 at different length scales

SAPO-5 crystals with different morphological features are studied using nitrogen adsorption-desorption analysis. Both samples display a combination of Type I and Type IV isotherms but with different patterns, confirming their hierarchical micro-/mesoporosity (Figure 5.13). For sample PyP-5.0, it has slit-shaped pores (H3 hysteresis loop) originating from the assembly and random orientation of nanoplates (Ashokan et al., 2021). Conversely, sample PA-5.0 shows broader H1 hysteresis loop which suggests that the solid has large ink-bottle shaped pores (Liu et al., 2021). As a result, the PA-5.0 (7.0 nm) exhibits larger average pore diameter than the PyP-5.0 (6.0 nm) (Table 5.2). This feature also explains the less packing of $[empy]^+$ in the pores of PA-5.0 as suggested by the TG/DTG analysis (Figure 5.9). The PA-5.0 sample

exhibits higher S_{micro} (222 m^2 g^{-1}) and V_{micro} (0.09 cm^3 g^{-1}) than the PyP-5.0 (182 m^2 g^{-1}, 0.07 cm^3 g^{-1}), which is originated from its higher crystallinity (Travkina et al., 2017). The hierarchical factor is also calculated and both PA-5.0 (0.12) and PyP-5.0 (0.10) samples indicating their hierarchical properties.

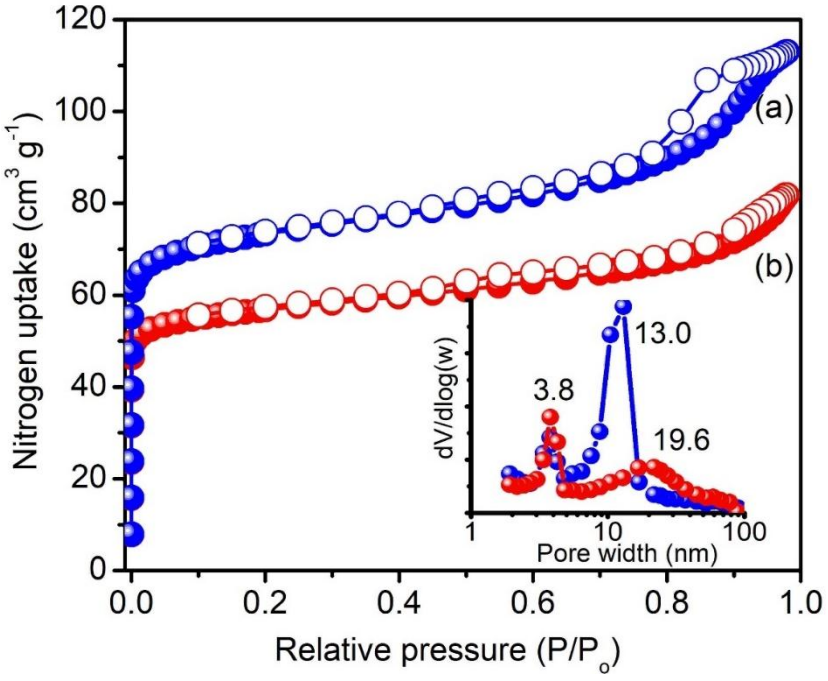

Figure 5.13 Nitrogen adsorption-desorption isotherms and BJH pore size distributions (inset) of (a) PA-5.0 and (b) PyP-5.0 samples

Table 5.2 Properties of SAPO-5 prepared using different P sources

Samples	S_{BET}[a] ($m^2\ g^{-1}$)	S_{micro}[b] ($m^2\ g^{-1}$)	S_{ext}[c] ($m^2\ g^{-1}$)	V_{micro}[d] ($cm^3\ g^{-1}$)	V_{tot}[e] ($cm^3\ g^{-1}$)	D_{av}[f] (nm)	HF[g]	NH_3-TPD acidity[h] (mmol g^{-1})			
								Weak	Mild	Medium-to-strong	Total
PA-5.0	285	222	63	0.09	0.17	7.0	0.12	0.13	0.10	0.50	0.73
PyP-5.0	224	182	42	0.07	0.13	6.0	0.10	0.08	0.10	0.22	0.40

[a]Specific surface area; [b]Micropore surface area; [c]External surface area; [d]Micropore volume; [e]Total pore volume; [f]Average pore size; [g]Hierarchical factor; [h]Acidity determined using deconvolution of peaks at 170 °C, 210 °C and 270 °C.

Based on the above findings and our understanding, the [empy]OH-templated crystallization process of SAPO-5 using H_3PO_4 and $H_4P_2O_7$ as P sources is considered to be as follows: the process begins with the mixing of precursors where aluminum isopropoxide and colloidal silica are hydrolyzed in [empy]OH alkaline solution. H_3PO_4 serves as readily made and active phosphate monomeric species for the formation of Si-O-P-O-Al oligomers (white amorphous precipitate formed). Long inorganic polymeric chain is then formed by extending the heating time where it also interacts with the $[empy]^+$ cation of [empy]OH by enfolding and encapsulating this guest cation, forming micropores. Concurrently, some $[empy]^+$ molecules are loosely enfolded within the pores, leading to the formation of secondary mesopores. These organic-inorganic entities serve as nucleation sites for the crystallization.

It should be noted that the stabilization energy alone cannot fully explain the crystal morphology of zeolite because the adsorption of organic template on the crystal surfaces during the crystal growth process can also influence the crystal growth rates of a particular crystal face and the final crystal morphology. It is reported that the stabilization energy of zeolite–organic template complex cannot fully explain the crystal morphology of zeolite (Keoh et al., 2016). Instead, it can be explained by the tendency of OSDA adsorb on the morphologically important plane surfaces (Jelfs et al., 2007). In the case of SAPO-5 synthesized with H_3PO_4 as the P source, the preferential adsorption sites for $[empy]^+$ template is [001] plane, *viz.* a surface that points out towards the z-direction (Gao et al., 2015). Hence, the anionic Si, Al and P inorganic monomers and oligomers from mother liquor will be attracted to this plane, whereby their accumulation on this [001] plane will lead to faster growth rate on this plane as compared to other planes, forming micron-sized SAPO-5 crystals with hexagonal and long cylindrical shape (Figure 5.14a).

On the other hand, when $H_4P_2O_7$ is added into the precursor mixture, it has to undergo additional hydrolysis step in order to form phosphate species, thus delaying the availability of reactive phosphate ions forming the inorganic oligomers (a clear solution with no amorphous solid formed). In addition, by taking the Löwenstein's rule into consideration in the skeleton of SAPO framework type material (thermodynamically unstable P-O-P bond is prohibited), only one P atom of $H_4P_2O_7$ will take part in the formation of AFI skeleton while the second -PO_3H group atom is pointed outward to the plane [001]. The second P atom cannot be incorporated into the AFI framework due to the fact that the formation of SAPO framework has to obey the Löwenstein's avoidance rule whereby thermodynamically unstable P-O-P bond is prohibited in the skeleton of framework. Hence, the occupancy of the second –PO_3H group on the [001] plane surface restricts the OSDA molecules from approaching, making the Si, Al and P monomers and oligomers preferably dwell and grow at the other surface planes. As a result, the crystal growth at [001] plane in *z*-direction is restricted while some nutrients from mother liquor are used to promote nucleation, leading to the formation of hexagonal SAPO-5 nanoplates grown in x-y direction (Figure 14b). With extending heating time to 6 h, the thermodynamically metastable SAPO-5 experiences reorganization of its inorganic polymeric chain and transforms into a more stable crystalline tridymite solid. Hence, the use of different P sources allows us to surmise how it affects the relative crystal growth rates of growing surfaces that further affecting the zeolite morphology.

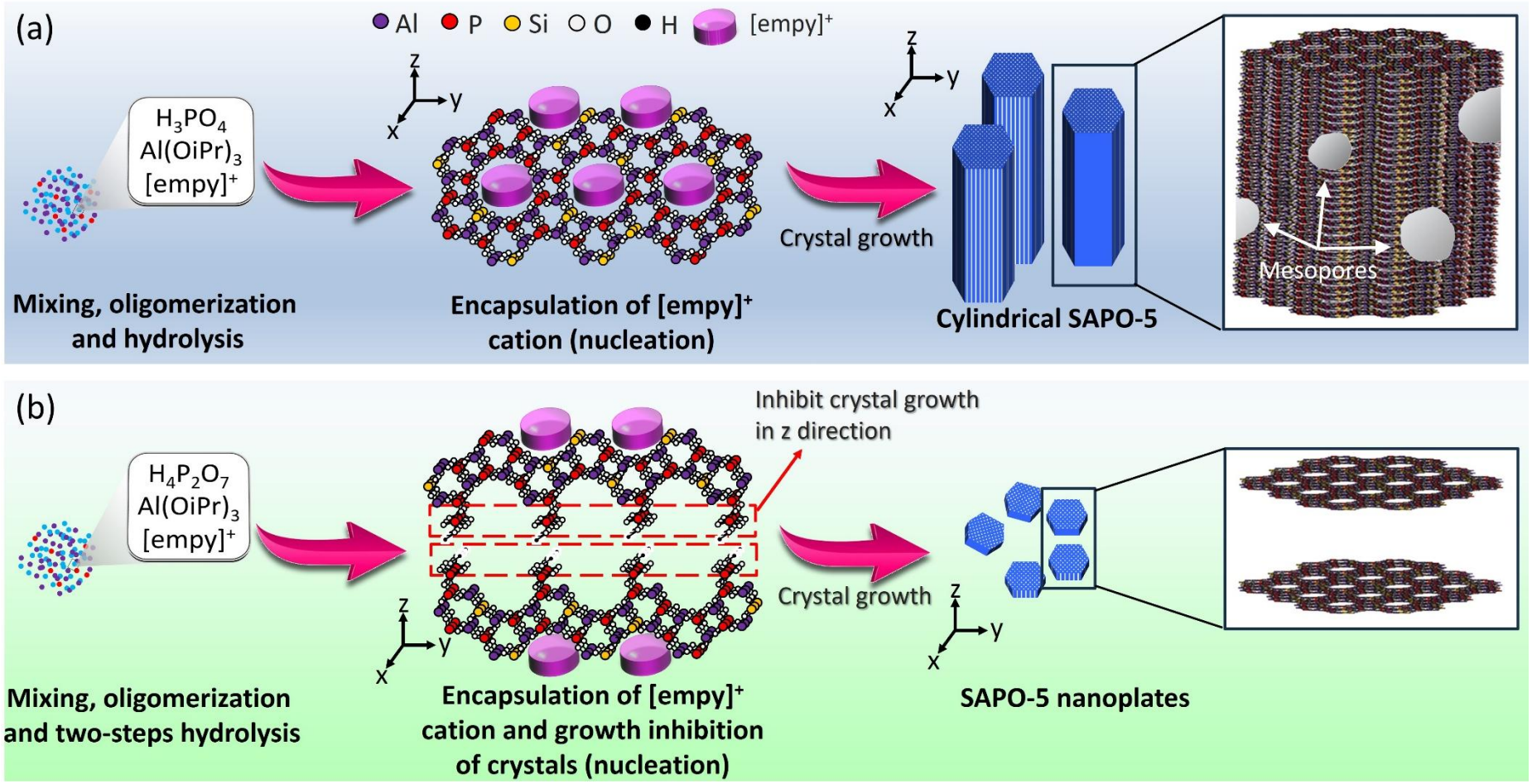

Figure 5.14 The crystallization pathways of SAPO-5 templated by [empy]OH using (a) H_3PO_4 and (b) $H_4P_2O_7$ as P sources

CHAPTER 6

CATALYTIC PERFORMANCE OF SAPO-11 AND SAPO-5 IN THE ESTERIFICATION OF LEVULINIC ACID AND LACTIC ACID

6.1 Catalytic esterification of levulinic acid study

Conversion of LA and EtOH into EL *via* esterification is used as a probe reaction to study the catalytic behavior of SAPO-11 (E-3 sample) under non-microwave instant heating conditions (Figure 6.1). Without adding any catalyst, the LA conversion is very low (5.6%) even after 60 min of heating at 150 °C. This indicates that the esterification of LA is an activated reaction. The conversion is enhanced tremendously when SAPO-11 is added, where 75.5% of conversion is recorded after heating at 150 °C for 20 min. Throughout the study, EL is produced over SAPO-11 with only water as a side product. Thus, it reveals that SAPO-11 is a potential active and selective catalyst for the conversion of LA into EL.

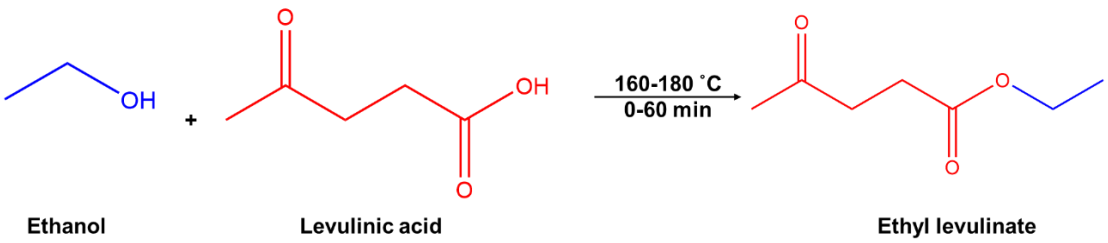

Figure 6.1 Esterification of LA and EtOH for producing EL

6.1.1 Effect of activation temperature of catalyst

Activation temperature is an important parameter prior performing catalytic reaction because it eliminates physiosorbed or chemisorbed water that deactivate surface active sites (Butt, 2012). Hence, different activation temperatures (room temperature, 100, 200, 300 and 400 °C) are studied separately on SAPO-11 under air conditions. As shown, the conversion of LA is positively influenced by the activation temperature (up to 300 °C) (Figure 6.2). This is because higher activation temperatures

can effectively remove the physiosorbed or chemisorbed water, leading to more efficient catalytic performance (Guo et al., 2019). Nevertheless, further increasing the temperature to 400 °C leads to a significant drop in the conversion. The decrease in performance can be explained by the partial collapse of the framework structure of SAPO-11 when it is activated at such high temperature (400 °C) (Wondraczek et al., 2013). As a result, it indirectly gives a detrimental impact on the reaction conversion. Hence, the SAPO-11 catalyst has to be activated at 300 °C prior use.

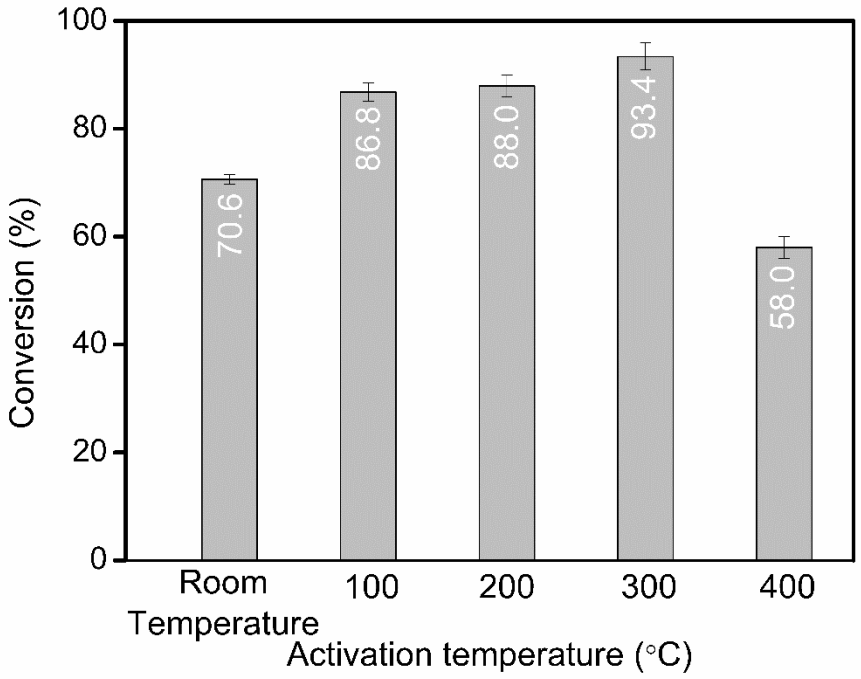

Figure 6.2 Effect of activation temperature on the conversion of LA when using SAPO-11 as a catalyst at 180 °C, for 30 min, on LA:EtOH ratio1:11

6.1.2 Effect of reaction temperature and time

The esterification reaction is investigated at various temperatures (150–180 °C) from 0−60 min over activated SAPO-11; the reaction at >190 °C was impossible because the reaction pressure will exceed 20 bar which will burst the reactor. The reaction conversion is enhanced by increasing the heating temperature (Figure 6.3). This is due to the fact that when more energy is provided to the system, the reaction

kinetics increase as stated by the Arrhenius equation (Du et al., 2016). For instance, at 30 min of reaction, 82.6% of conversion is recorded at 150 °C, and this increases to 87.0% (160 °C) and 90.6% (170 °C) before reaching to 93.4% at 180 °C (Figure 6.2(a–d)). Based on the reaction study, the optimum reaction time and temperature are 30 min and 180 °C, respectively, because the conversion reaches almost plateau after 30 min.

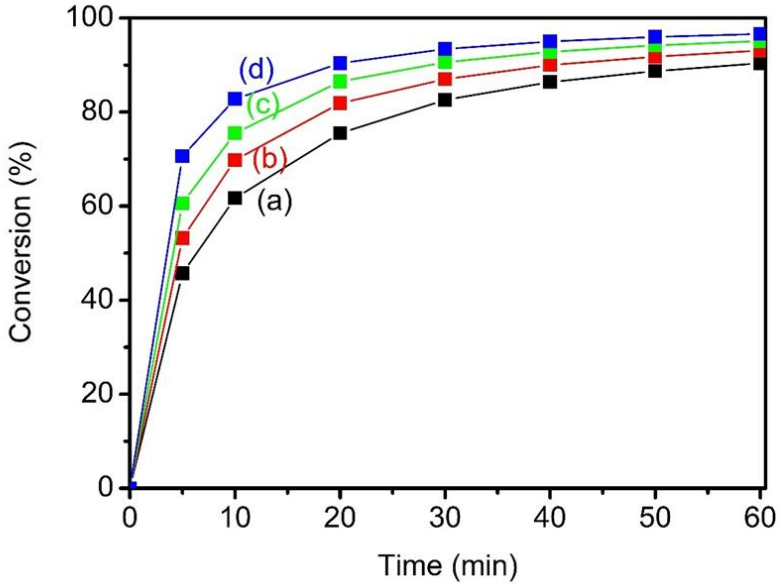

Figure 6.3 Conversion of LA via esterification enhanced by SAPO-11 (E-3) catalyst at (a) 150 °C, (b) 160 °C, (c) 170 °C and (d) 180 °C under conductive instant heating using 0.100 g of SAPO-11, on LA:EtOH ratio 1:11

6.1.3 Effect of catalyst amount

The effect of catalyst amount is studied at 180 °C for 30 min with a molar ratio of 1:11 (LA:EtOH) using 0, 0.025, 0.050, 0.075, 0.100 and 0.125 g of SAPO-11. Without catalyst, the conversion rate is merely 6.6%, and the LA conversion is enhanced significantly to 52.7% when 0.025 g catalyst is added (Figure 6.4). The conversion keeps increasing to 93.4% where the catalyst loading increases to 0.100 g. Such a phenomenon can be explained by the high availability of Brønsted acid sites when more solid acid catalyst is added (see Section 4.5). However, the LA conversion slightly decreases when the catalyst loading is further increased to 0.125 g (91.7%), and this may be due to the excessive catalyst loading causing inefficient stirring (Ma et al.,

2022). Furthermore, the water molecules produced during the esterification reaction can also deactivate the SAPO-11 catalyst's active sites, and this affects the efficacy of catalyst (Kiss et al., 2006). Therefore, 0.100 g of SAPO-11 catalyst is the ideal loading for this reaction.

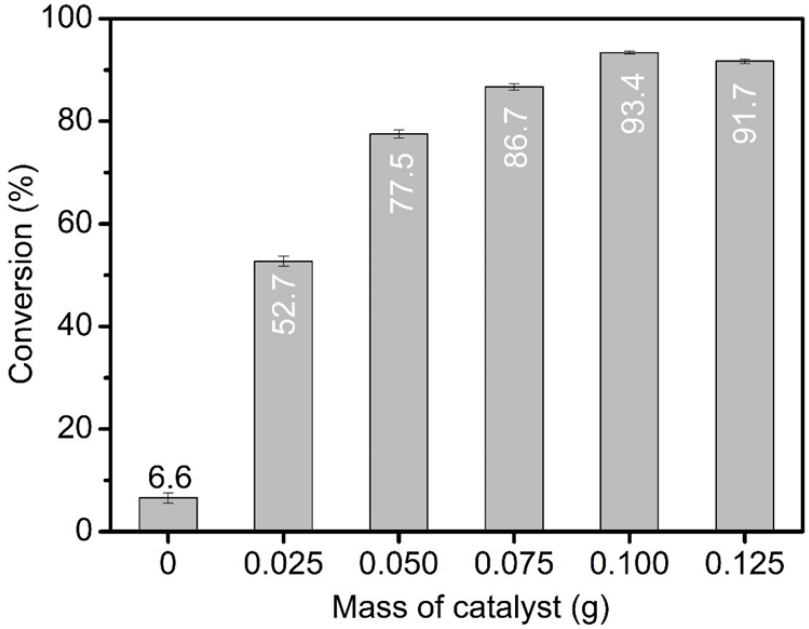

Figure 6.4 Effect of catalyst loading on the conversion of LA u at 180 °C, for 30 min, on LA:EtOH ratio1:11

6.1.4 Effect of LA:EtOH ratio

The effect of LA:EtOH molar ratio on esterification of LA is conducted at 180°C for 30 min by utilizing 0.100 g of SAPO-11. In order to get a high conversion of LA in the esterification of LA, one can reduce water by-product generation or increase the EtOH concentration to favor the forward reaction, following the Le Chatelier's principle (Song et al., 2021). As predicted, a remarkable increase in the reaction conversion is observed from 17.5% to 93.9% when the EtOH content is increased from 1:1 to 1:15 (Figure 6.5). In contrast, there is a consistent decrease in the LA conversion, dropping from 22.7% to 7.3% when the LA:EtOH ratio is raised from a ratio of 5:1 to 13:1. Thus, this phenomenon shows that when the concentration

of LA increases, the active sites of catalyst are occupied by LA molecules, leading to a drop in conversion efficiency (Qu et al., 2020). In contrast, the increased amount of EtOH enhances the reaction conversion. Hence, it is clearly shown that the activation of EtOH is the limiting step in the esterification reaction. From the study, the LA:EtOH molar ratio of 1:11 is selected as the optimal ratio as there is only very small increase in conversion beyond this point.

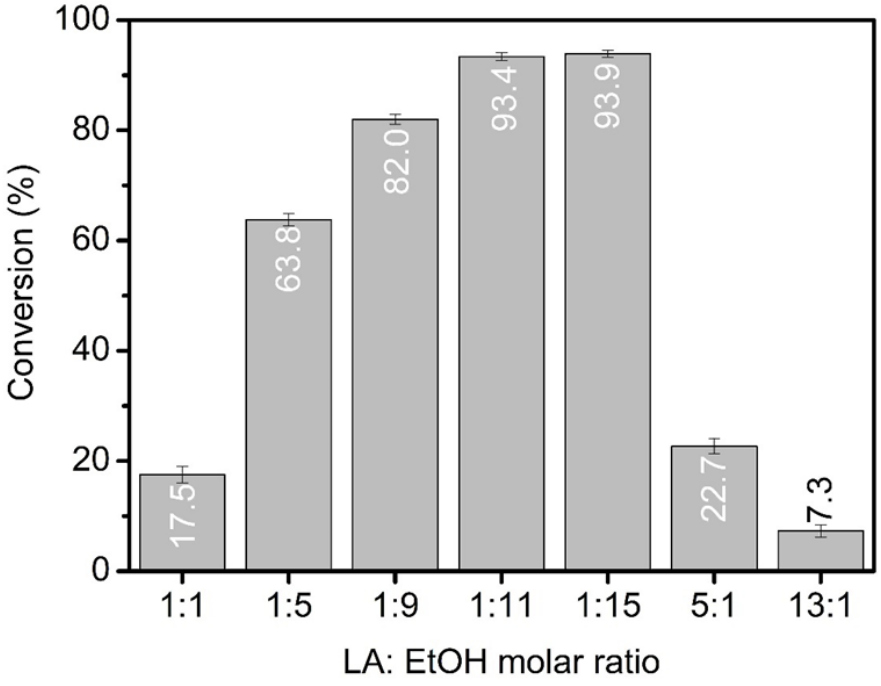

Figure 6.5 The effect of LA:EtOH molar ratios on the conversion of LA at 180 °C, for 30 min, using 0.100 g of SAPO-11

6.1.5 Effect of alcohol chain length and branching

Six types of alcohols, namely methanol, ethanol, 1-propanol, 2-propanol, 1-butanol, and 2-butanol are also studied to study the influence of their chain length and branching on LA esterification. The results show that small alcohol molecules such as methanol and EtOH exhibit more reactivity in this reaction (Figure 6.6). This is because methanol and EtOH of smaller molecules can easily access and react with LA at the active sites located inside the pores of SAPO-11. For methanol, it shows lower conversion despite its smaller size due to its high polarity that tends to strongly adsorb

on acid sites, which reduce its overall reactivity. The catalytic activity is weakening with increasing the molecular size (or molecular weight) of alcohols which can be explained by the molecular accessibility (Trincado et al., 2014). The conversion is 89.9% for 1-propanol and it decreases to 83.1% for 1-butanol.

In addition, branched alcohols such as 2-propanol and 2-butanol are also compared with 1-propanol and 1-butanol where the branched alcohols only afford 68.1% and 61.2% of conversion, respectively, which are lower than their linear counterparts. Thus, the branched alcohols enlarge their molecular sizes, which in turn restrict them from diffusing into the pores of SAPO-11. In addition, the branched alcohols also provide steric hindrance on hydroxyl group, making it more difficult be contact with the acid sites. As a result, low conversion is observed.

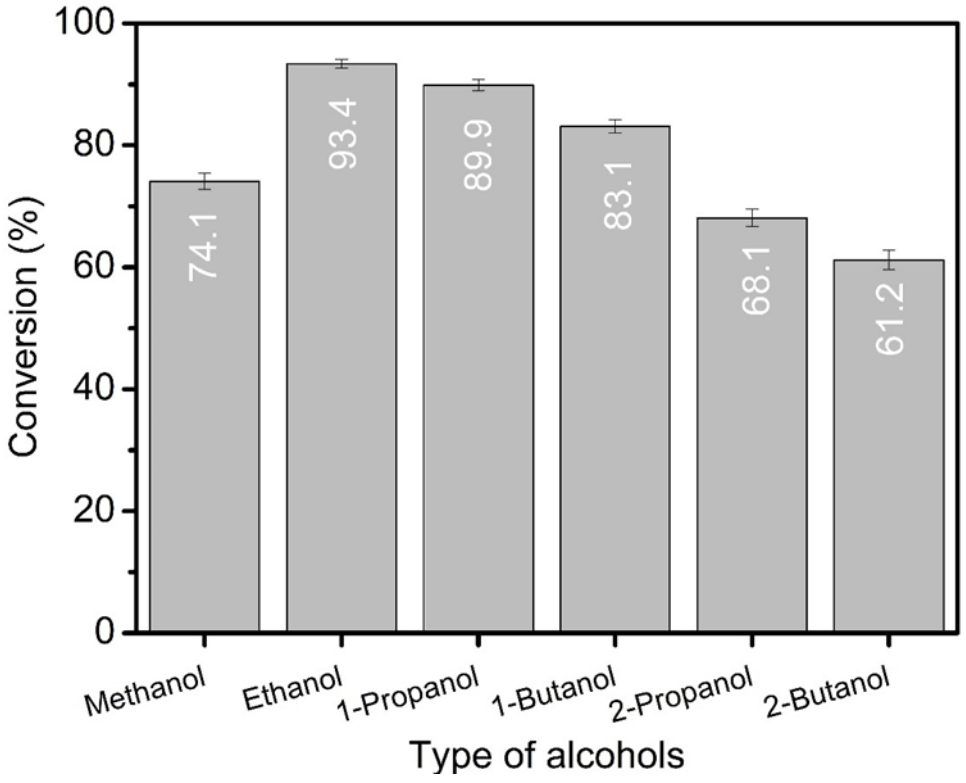

Figure 6.6 The effect of alcohol chain length and branching on the conversion of LA at 180 °C, for 30 min, on LA:alcohol ratio 1.36:14.8, using 0.100 g of SAPO-11

6.1.6 Effect of heating mode

Three heating modes, namely conventional reflux, autoclave and non-microwave instant heating, are utilized to conduct esterification of LA. For this study, the following reaction conditions are used: SAPO-11 mass = 0.100 g, LA = 1.36 mmol, EtOH = 14.8 mmol, reaction temperature = 180 °C, and reaction time = 30 min. The conventional reflux heating with a circulating chiller and in an oil bath gives the lowest LA conversion (18.7%) because of poor heat transmission, impacting the heating process overall (Figure 6.7). In addition, the reflux mode in an open system can only be performed at ambient pressure. Thus, low conversion is predicted.

The autoclave method (stirring in an oil bath) achieves a higher conversion (30.1%) due to autogenic pressure that improves molecular collision between reactants. However, the conversion remains quite low due to heat transfer issue where the heat has to transmit from oil bath to the reaction solution through a thick stainless steel and Teflon walls of autoclave.

On the other hand, the non-microwave instant heating method give an impressive conversion of 93.4% due to the use of superheating conductor (silicon carbide) as reaction vessel and high stirring speed (800 rpm). The combination of both features ensures the uniform and rapid heating of reaction mixture to the desired temperature, which mimics the rapid heating of a microwave (Li et al., 2019). In addition, the reaction is performed in a closed system and the high pressure also allows catalytic performance enhancement.

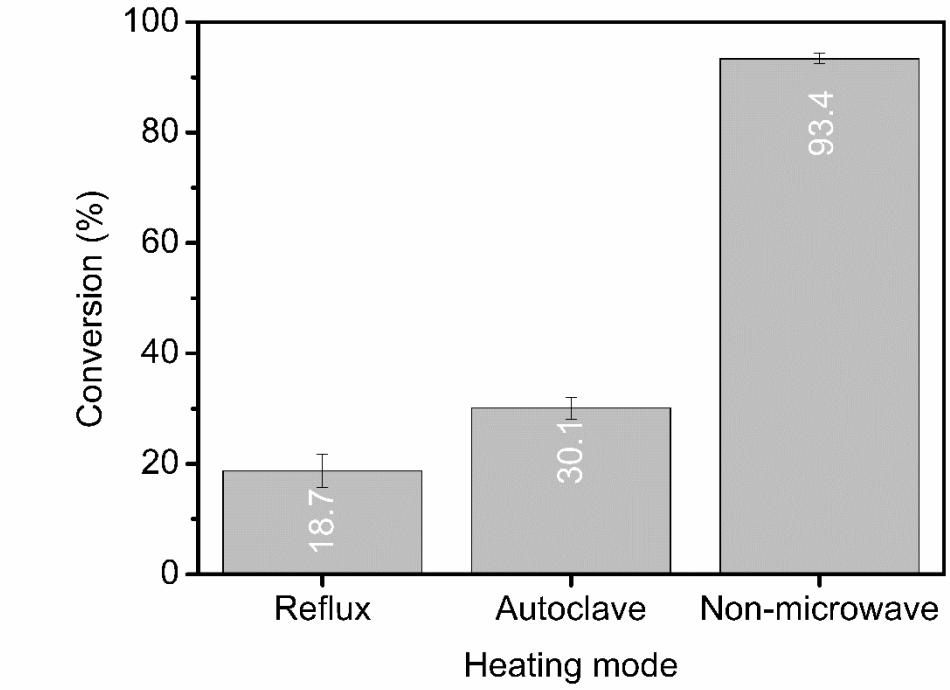

Figure 6.7 The effect of heating mode on the catalytic conversion of LA using 0.100 g of SAPO-11, on 1.34:14.8 LA:EtOH ratio at 180 °C, for 30 min

6.1.7 Catalytic performance of various catalysts

The catalytic performance of SAPO-11 is compared with conventional homogeneous catalysts (H_2SO_4, HCl, acetic acid, p-toluenesulfonic acid) at 180 °C for 30 min under non-microwave instant heating. It is shown that both H_2SO_4 and HCl achieve 100% conversion (Figure 6.8). However, their selectivity towards EL is merely 86.3% and 90.1%, respectively, where 4-ethoxy-valerolactone and alpha-Angelica lactone are produced as by-products.

For acetic acid, low conversion (74.2%) with 100% selectivity of EL is recorded and this can be explained by its weak acidity. On the other hand, SAPO-11 shows comparable catalytic performance as *p*-toluenesulfonic acid, achieving nearly 95% conversion and excellent 100% EL selectivity, whereas SAPO-5 achieves 95.7% conversion with the same 100% selectivity. The superior performance of SAPO-11 can hence be explained by its mild-to-strong acidity and one dimensional

10-membered ring pore channel (4.63 × 2.01 × 2.01 $Å^3$) that allows molecular sieving capability for selectively producing only EL as a single product.

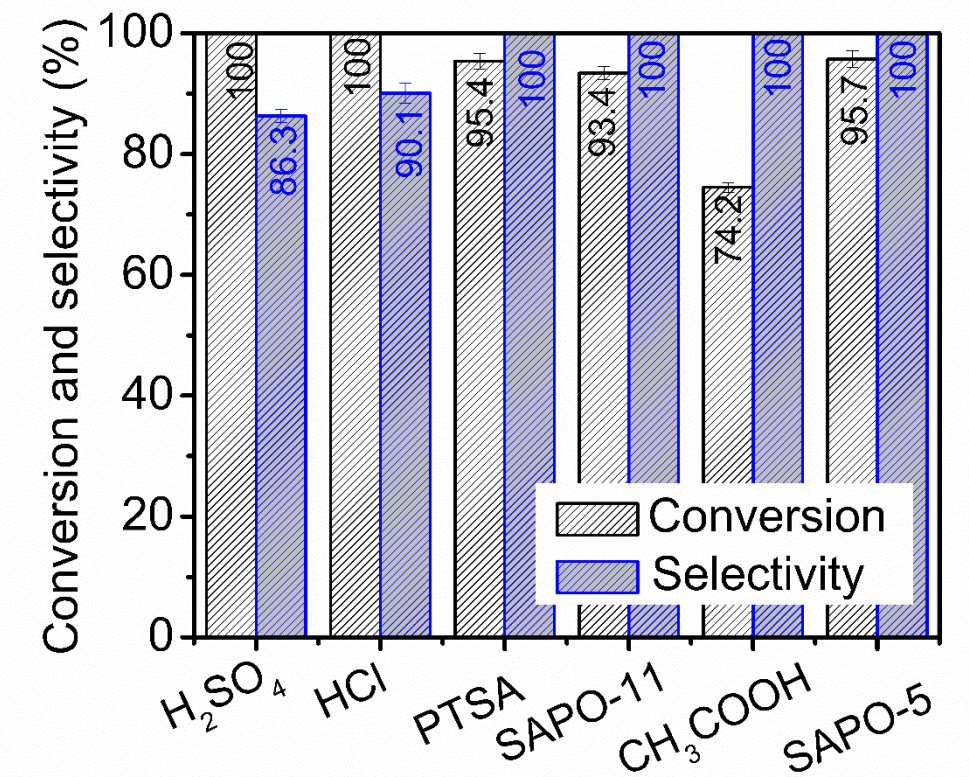

Figure 6.8 Comparison of catalytic activity between synthesized SAPO-11 and conventional homogeneous acids, on LA:EtOH ratio 1:11, using 0.100 g of SAPO-11 (17.98 µmol) equivalent to 0.0017 g of HCl, 0.0018 g of H_2SO_4, 0.0011 g of CH_3COOH and 0.0035 g of p-toluenesulfonic acid (PTSA)

6.1.8 Mass balance

The stoichiometric chemical equation for the esterification of LA and EtOH is shown as in Figure 6.1, where one mole of EtOH reacts with one mole of LA to yield one mole of EL. This simplified representation is further elucidated using theoretical mass balance whereby the Law of Conservation of Mass states that the mass entering a system must equal the mass exiting the system. This means that the mass input is equal to the mass output (Table 6.1).

When comparing the experimental mass balance data in Table 6.1 with the theoretical model, a slight discrepancy is observed in the mass of the products formed. Despite this difference, the experimental mass balance remains acceptable, as

demonstrated by the small error margin of 0.10%. Similarly, EtOH showed a minor difference between theoretical and experimental values, with 0.664 g in and 0.603 g out in the experiment, compared to the theoretical balance of 0.664 g in and 0.611 g out. EL, the main product, was predicted to have 0.165 g formed, whereas experimentally, 0.171 g was obtained. Water, another product, also showed a slight deviation from theoretical values (0.021 g predicted vs. 0.022 g experimentally).

Table 6.1 Theoretical and experimental mass balance

Substances	**Theoretical**		**Experimental**	
	In (g)	**Out (g)**	**In (g)**	**Out (g)**
Levulinic acid	0.142	0.009	0.142	0.009
Ethanol	0.664	0.611	0.664	0.603
Ethyl levulinate	0	0.165	0	0.171
Water	0	0.021	0	0.022
Total	**0.806**	**0.806**	**0.806**	**0.805**
Error	**0.0%**		**0.10%**	

6.1.9 Reusability test

Although HCl and H_2SO_4 homogeneous catalysts achieve 100% conversion, they are not reusable. On the other hand, the SAPO-11 catalyst is recyclable, and the reaction performance is nearly maintained even after five consecutive cycles of reaction with small loss in activity (Figure 6.9). Thus, being reusable, ecofriendly and not corrosive, SAPO-11 is more preferable as an acid catalyst compared to its homogeneous counterparts for catalyzing esterification of LA into EL.

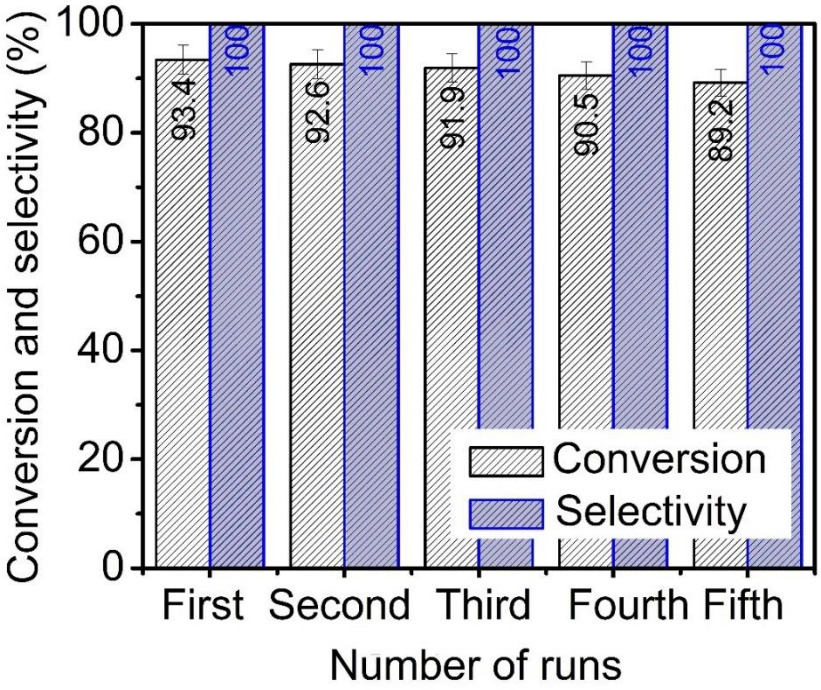

Figure 6.9 SAPO-11 catalyst reusability test at 180 °C, for 30 min

6.1.10 Proposed catalytic reaction mechanism

The esterification of LA and EtOH catalyzed by SAPO-11 is described as in Figure 6.10 based on the current and previous studies (Ramli et al., 2017). At first, LA and EtOH diffuse into the micropores of SAPO-11 where LA exhibits higher binding affinity towards the Brønsted acid sites of the catalyst, resulting in the formation of a protonated LA intermediate that augments the electrophilic nature of the carbonyl carbon (Step 1). Next, the oxygen of EtOH as nucleophile attacks the carbonyl carbon and forms an oxonium ion (Step 2). A new oxonium ion is then formed as a subsequence of proton transfer from the previous oxonium ion (Step 3). The acid sites of catalyst are restored through the loss of water and deprotonation, where EL as the end product is formed (Step 4).

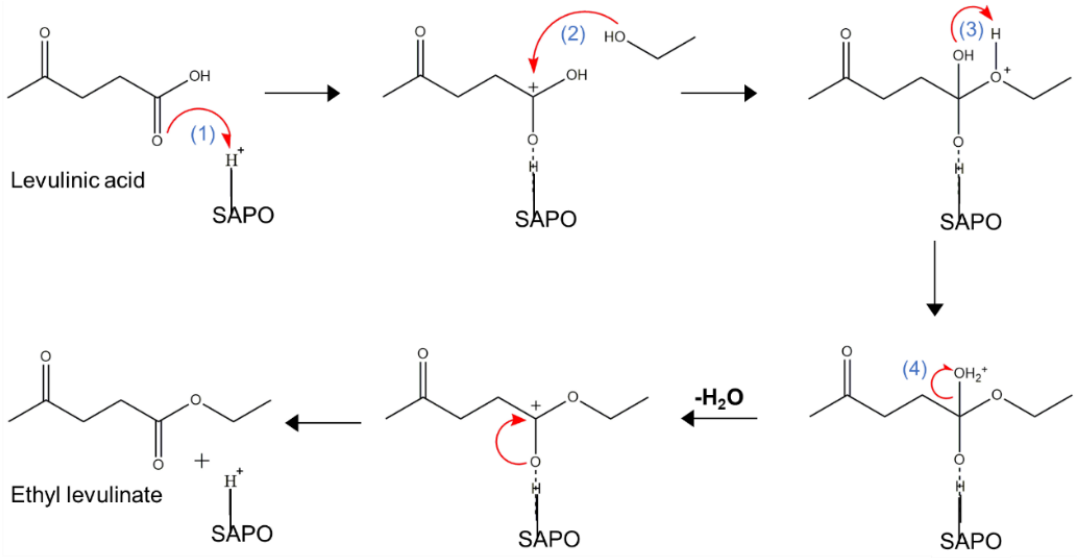

Figure 6.10 Mechanism of EtOH and LA esterification

6.2 Catalytic esterification of lactic acid study

The catalytic behaviour of SAPO-5 synthesized using two types of P sources, namely H_3PO_4 (PA-5.0) and $H_4P_2O_7$ (PyP-5.0) is studied in the esterification of LcA into ELc under non-microwave instant heating conditions. The effects of several reaction parameters are studied, such as activation temperature, reaction temperature, time, catalyst loading, reactants ratio, alcohol chain length and branching, heating mode and type of catalysts.

6.2.1 Effect of reaction temperature and time

The esterification of LcA is studied at 120, 140 and 160 °C while the reaction time is fixed at 20 min. It is shown that the reaction conversion increases with heating time and temperature. This trend is due to the more energy input is provided to the reaction system which increases the kinetic energy and effective molecular collision between reactants (Du et al., 2016).

Without catalyst, the conversion of 27.2% is observed at 120 °C without catalyst. This rate increases to 39.6% at 140 °C before it goes up to 46.8% at 160 °C. Conversely, employing PyP-5.0 SAPO-5 yields a conversion of 61.1% at 120 °C,

which rises to 67.0% at 140 °C and 74.5% at 160 °C. Similarly, PA-5.0 SAPO-5 follows the same trend, with an increased conversion of 80.9% at 120 °C and then to 85.1% at 140 °C, and finally reaching 90.9% at 160 °C after 30 min. Based on the reaction analysis, PA-5.0 SAPO-5 is more reactive than PyP-5.0 SAPO-5 while the optimal reaction time and temperature are determined to be 20 min of heating at 160 °C (87.0% conversion) since the conversion almost plateau after 20 min. For the next study, PA-5.0 SAPO-5 catalyst is used for the parametric and optimization studies.

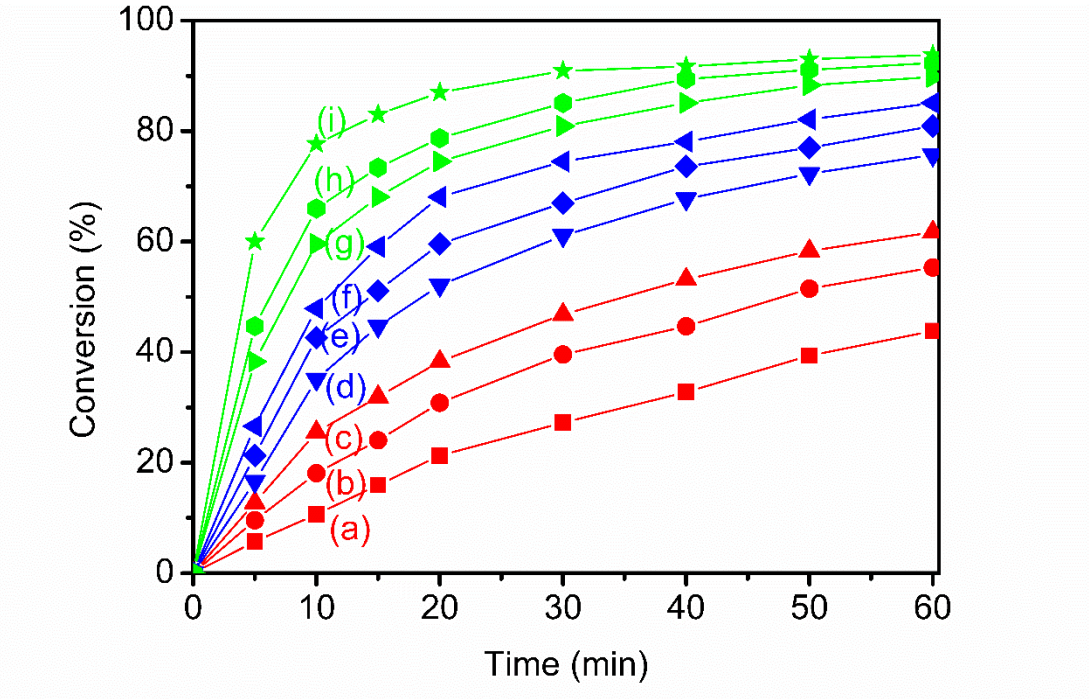

Figure 6.11 Catalytic esterification conversion of LcA (a, b, c) without catalyst, and with (d, e, f) PyP-5.0 and (g, h, i) PA-5.0 SAPO-5 catalysts at 120 °C, 140 °C and 160 °C, respectively using 0.100 g of SAPO-5, at 1:10 LcA:EtOH ratio.

6.2.2 Effect of activation temperature of catalyst

The catalyst requires exposure to a specific temperature range to achieve optimal activity (Othman et al., 2012). This activation process is crucial as it facilitates the removal of weakly bound impurities from the surface of catalyst (Montemore et al., 2017). Hence, the effect of activation temperature (25 °C to 400 °C) of PA-5.0 SAPO-5 on esterification of LcA is studied (Figure 6.12). It is observed that the selectivity remains at 100% across all activation temperatures, indicating that while

the catalyst activity may vary with temperature, the reaction pathway consistently favours the desired product, regardless of the activation temperature applied.

Without catalyst activation (at 25 °C), the conversion is 55.8%. When the activation temperature is raised, an increase in the conversion of LcA is observed until it reaches 300 °C (87.0%). Nevertheless, further increasing the temperature to 400 °C leads to a significant reduction in the conversion (53.7%). The observed decrease in performance can be attributed to the partial structural collapse of the SAPO-5 catalyst during activation at such high temperature (Bellatreche et al., 2016). Hence, the optimum activation temperature is 300 °C.

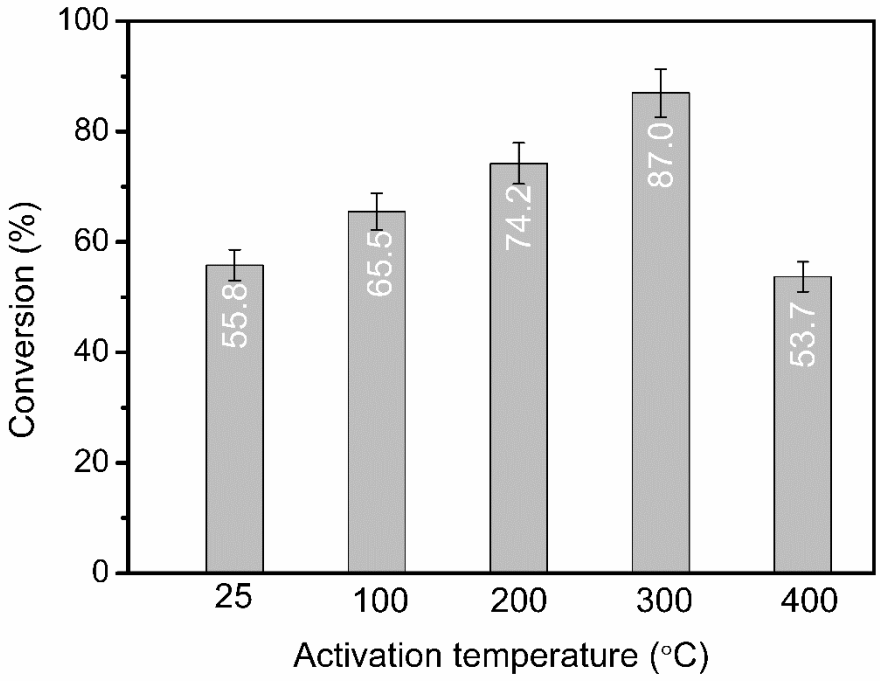

Figure 6.12 Effect of activation temperature on the conversion of LcA usin 0.100 g of PA-5.0 SAPO-5, at 160 °C, for 20 min, at 1:10 LcA:EtOH ratio

6.2.3 Effect of catalyst amount

The effect of PA5.0 SAPO-5 catalyst loading is investigated at 160 °C for 20 min with a LcA:EtOH molar ratio of 1:10 by varying the catalyst mass from 0 to 0.150 g. Without catalyst, the conversion is 38.3%. Upon adding 0.050 g of catalyst, the

conversion increases to 63.5% (Figure 6.13). Further increasing the catalyst loading to 0.100 g boosts the conversion to 87.0%. The enhancement of conversion with catalyst loading hence can be attributed to the increment of surface Brønsted acid sites that are available for reaction. However, when the catalyst loading is increased to 0.150 g, the conversion of LcA declines to 73.6%. This is possibly due to the inefficient stirring resulting from excessive amount of catalyst in the mixture, which affects the reaction conversion (Kiss et al., 2006; Ma et al., 2022). Thus, the optimum loading of 0.100 g of PA-5.0 SAPO-5 catalyst is used for further study.

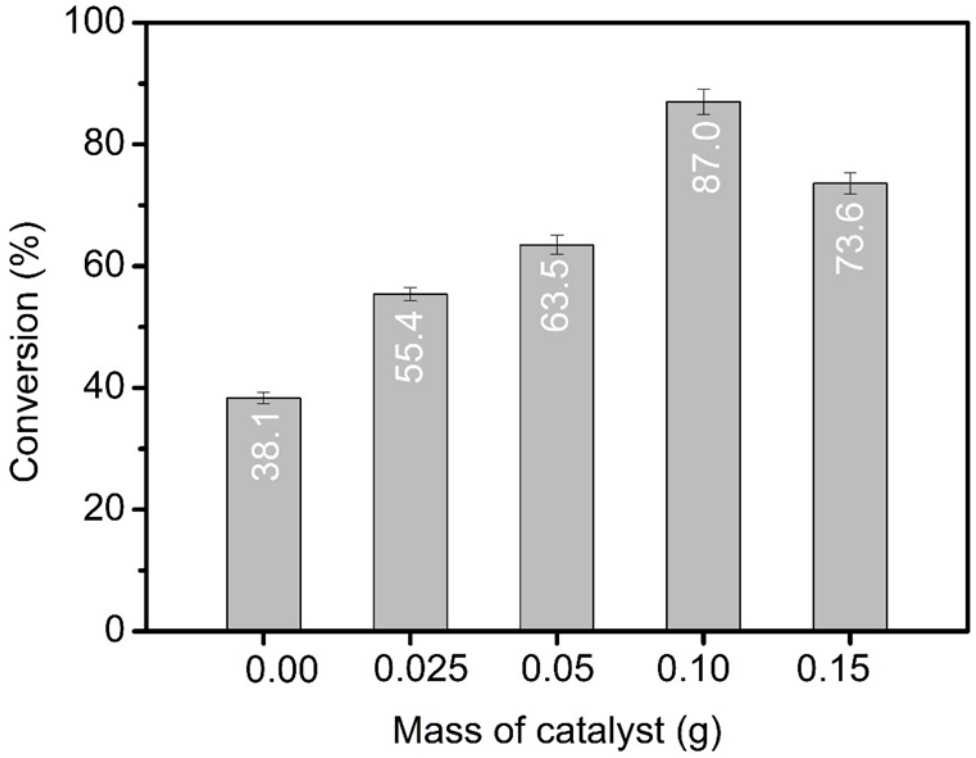

Figure 6.13 Effect of PA-5.0 SAPO-5 catalyst loading on the conversion of LcA at 160 °C, for 20 min, at 1:10 LcA:EtOH ratio

6.2.4 Effect of LcA:EtOH ratio

The effect of LcA:EtOH molar ratio is studied at 160 °C for 20 min using 0.100 g of PA-5.0 SAPO-5. Since the esterification of LcA is a reversible reaction, several ways to increase the reaction conversion can be considered by taking the Le Chatelier's principle into account. One can reduce the generation of water byproduct during the

reaction but it is quite tedious. Another strategy is to increase the concentration of EtOH so as to favor the forward reaction more than backward reaction. This can be proven when the ratio of LcA:EtOH is increased from 1:3 to 1:10, the reaction conversion is also increased from 60.8% to 78.0% (Figure 6.14). Based on the study, the LA:EtOH molar ratio of 1:10 is found to be the optimum ratio. Beyond this point, the LcA conversion decreases.

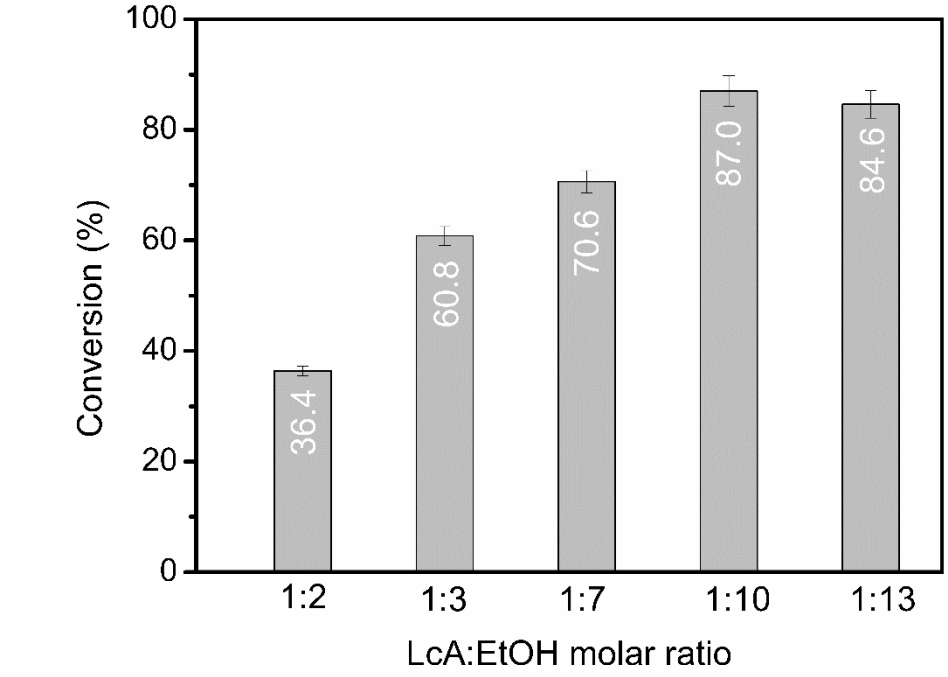

Figure 6.14 The effect of LcA:EtOH molar ratio on the conversion of LcA at 160 °C, for 20 min, using 0.100 g of PA-5.0 SAPO-5

6.2.5 Effect of alcohol chain length and branching

The effect of types of alcohols with different chain length and branching on the conversion of LcA is also studied with the PA-5.0 SAPO-5 catalyst. When methanol is used, the conversion of LcA reaches 54.8%, then it rises to 87.0% when EtOH is utilised (Figure 6.15). However, when the carbon chain length further increases, the conversion decreases from 87.0% to 79.8% and 59.7% when 1-propanol and 1-butanol are utilized, respectively. This decrease can be explained by the less effective accessibility of long chain alcohol molecules (1-propanol: 3.11 × 5.35 × 2.54

Å^3; 1-butanol: 1.81 × 6.61 × 2.54 Å^3) to the acid sites in the micropores of SAPO-5 (7.3 × 7.3 Å^2) compared to EtOH (3.36 × 4.07 × 2.03 Å^3) and LcA (4.95 × 3.69 × 2.58 Å^3) (Wasanasuk & Tashiro, 2011). In addition, branched alcohols such as 2-propanol (3.55 × 4.37 × 3.12 Å^3) and 2-butanol (4.05 × 5.66 × 2.99 Å^3) are also utilised in the esterification process, resulting in 75.4% and 13.7% of LcA conversion, respectively. Thus, it shows that their larger molecule sizes cause pore accessibility issue besides the branching also causes steric hindrance of OH group that reduces the ability of OH group to interact with the acid sites.

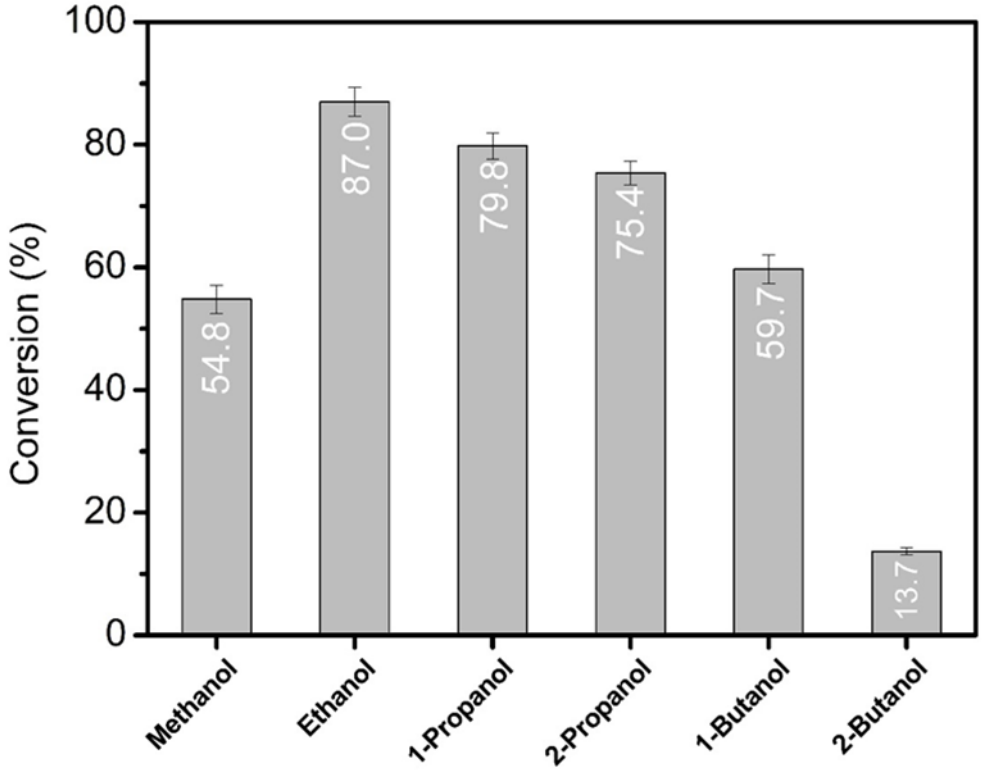

Figure 6.15 The effect of alcohol chain length and branching on the conversion of LcA at 160 °C, for 20 min, at 1.03:10.50 LcA:alcohol ratio, using 0.100 g of PA-5.0 SAPO-5

6.2.6 Effect of heating mode

The esterification of LcA using PA-5.0 SAPO-5 catalyst is investigated using three different heating modes, namely conventional reflux, autoclave, and non-microwave instant heating, where the reaction parameters are kept similar (Figure 6.16). For the conventional reflux heating, it results in a relatively low LcA conversion

of 17.4%. This result is attributed to inefficient heat transfer besides the unability of this method to conduct the reaction at above 1 atm, thus hindering the overall reaction performance. On the other hand, the autoclave method shows an improved conversion to 28.0% due to the autogenic pressure that promotes better molecular collision among reactants (Foster, 2013). For the non-microwave instant heating method that utilizes silicon carbide for superior thermal conduction and is able to run reaction up to 20 bars, it significantly enhances the conversion to 87.0%. Hence, this approach offers another good heating method that allows uniform and rapid heating besides achieves efficient conversion mimicking to microwave heating.

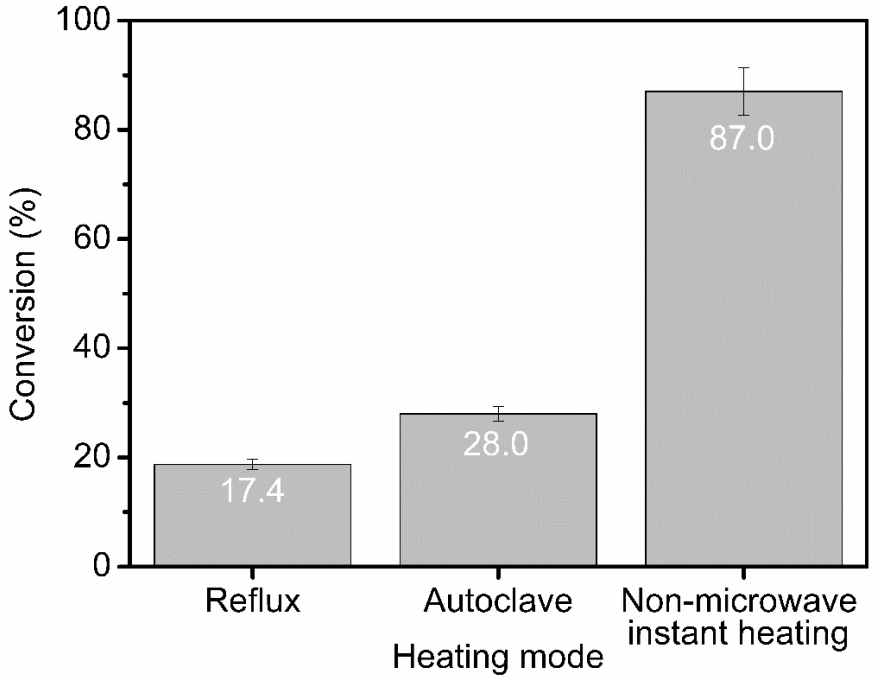

Figure 6.16 Effect of heating mode on the catalytic conversion of LcA using 0.100 g of PA-5.0 SAPO-5, on 1.03:10.50 LcA : EtOH ratio, at 160 °C, for 20 min

6.2.7 Catalytic performance of various catalysts

The catalytic behavior of PA-5.0 and PyP-5.0 samples in the esterification of LcA with EtOH is studied under non-microwave instant heating condition (160 °C, 20 min). In the absence of catalyst, the reaction goes in a slow manner (38.3% of conversion) but 100% selective to ELc (Table 6.2, Entry 1). The catalytic reaction is

enhanced by PyP-5.0 with 74.3% of conversion is recorded thanks to its nanocrystalline feature that provides a short diffusion path length (Entry 2) (Majano et al., 2011). Meanwhile, PA-5.0 catalyst affords higher conversion (87.0%) than PyP-5.0, suggesting that the PA-5.0 catalyst is more reactive thanks to its hierarchical structure that promotes high accessibility besides having high surface acidity (Entry 3) (Rilyanti et al., 2016). Of note, both catalysts also exhibit a high molecular sieving effect forming only ELc as a single product.

Table 6.2 Esterification of LcA with EtOH over various catalysts.[a]

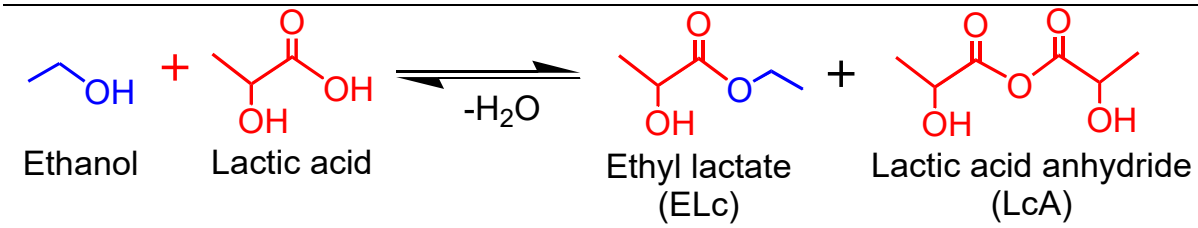

Entry	Catalyst	Conversion (%)	TON[b]	TOF (min^{-1})[b]	ELc selectivity (%)	LcA selectivity (%)
1	No catalyst	38.3	–	–	100	0
2	SAPO-5 (PyP-5.0)	74.3	5.2	0.26	100	0
3	SAPO-5 (PA-5.0)	87.0	7.1	0.35	100	0
4	H_2SO_4	100	9.0	0.45	86.3	13.7
5	HCl	100	9.0	0.45	90.1	9.9
6	H_3PO_4	57.1	2.7	0.14	92.0	8.0
7	H-Y	62.6	3.5	0.18	100	0
8	H-LTL	66.3	4.1	0.20	98.1	1.9
9	H-MOR	75.0	5.3	0.27	96.3	3.7
10	SAPO-20	47.4	1.3	0.07	100	0
11	SAPO-34	89.5	7.5	0.37	99.8	0.2

12	SAPO-11	59.7	4.9	0.24	100	0
13	TEAOH-SAPO-5	79.6	6.0	0.30	100	0

[a]Amount of catalyst = 68 μmol equivalent to 0.100 g of zeolite catalysts; lactic acid:ethanol molar ratio = 1:10, T = 160 °C; t = 20 min; n = 2. [b]After deducting reaction conversion without catalyst

Homogeneous (HCl, H_3PO_4 and H_2SO_4) and heterogeneous (H-MOR, H-LTL, H-Y, SAPO-20 and SAPO-34) catalysts are also assessed in this reaction for comparative study. As shown, non-recyclable H_2SO_4 and HCl attain full conversion but with reduced ELc selectivity (86−90%) (Entries 4 and 5). Instead, self-esterification of LcA prones to occur in this homogenous catalytic system, producing ethyl ester-2-oxo-propanoic acid as a side product. The H_3PO_4 with weaker acid strength merely gives 57.1% of conversion and 92.0% selective to ELc (Entry 6).

Meanwhile, protonated aluminosilicate zeolites with 12-membered ring pore sizes (H-MOR, H-LTL and H-Y) gives moderate activity (62–75%) and considerably good ELc selectivity (>96%) (Entries 7–9). H-LTL (Si/Al ratio = 3.1) with one-dimensional channel system shows better conversion than H-Y (Si/Al ratio = 2.1) although H-Y has three-dimensional porous system (Entries 7 and 8). This scenario can be due to the higher Si content of H-LTL that enhances its acid strength (Liu et al., 2016). This observation is further substantiated when high silica H-MOR catalyst (Si/Al ratio = 6.1) is used where 75.0% of conversion is achieved (Entry 9). The catalytic performance is also tested in other SAPO zeolites with small (SAPO-20) and medium (SAPO-34) pore sizes. Poor conversion is recorded by SAPO-20 (47.4%) which can be explained by its inaccessible micropores (2.53 × 2.53 $Å^2$) while the catalytic conversion mainly occurs on its external surface (Entry 10) (IZA, 2024). SAPO-34 shows good catalytic performance with 89.5% conversion and 99.8% of ELc selectivity due to its appropriate pore size (3.72 × 3.72 $Å^2$) that fits well the

reactants (EtOH: 3.53 × 2.03 × 1.80 $Å^3$; LcA: 4.35 × 3.56 × 3.07 $Å^3$) and ELc (7.11 × 3.55 × 3.12 $Å^3$) (Entry 11) (IZA, 2024). Its performance is comparable as PA-5.0 SAPO-5 catalyst.

The TOF is computed to express the catalytic efficiency of catalysts. Strong H_2SO_4 and HCl displays high TOF (0.45 min^{-1}) demonstrating the high efficiency of their protons (H^+) in catalyzing the reaction (Entries 4 and 5). Nevertheless, these homogeneous catalysts are harmful, toxic and non-reusable. On the other hand, SAPO-5, in particular PA-5.0, appears to be the most ideal catalyst among zeolite catalysts since it shows very high activity (TOF = 0.35 min^{-1}) almost similar as SAPO-34 (TOF = 0.37 min^{-1}), and only ELc is produced thanks to its hierarchical effect (Entry 3). In addition, PA-5.0 also exhibits similar selectivity but higher activity than conventional TEAOH-synthesized SAPO-5 (TOF = 0.30 min^{-1}) thanks to its hierarchical structure that promotes better diffusivity (Entry 13). Meanwhile, SAPO-11 shows lower LcA conversion compared to SAPO-5 (59.7%) but with 100% selectivity (Entry 12).

The catalyst reusability of both SAPO-5 samples is performed. Both zeolites show high reusability where the product selectivity is maintained, and the TOF values only drop approx. 24% (PA-5.0: 0.35 → 0.28 min^{-1}; PyP-5.0: 0.26 → 0.19 min^{-1}) after the 5^{th} run of reaction (Figure 6.17). In addition, the framework structure of SAPO-5 remains stable and no structural collapse is observed after reusability test (Figure 6.18). Hence, from the reaction efficiency and environmental point of view, hierarchical PA-5.0 SAPO-5 is a promising catalyst to replace conventional homogeneous catalysts for producing various biofuel compounds.

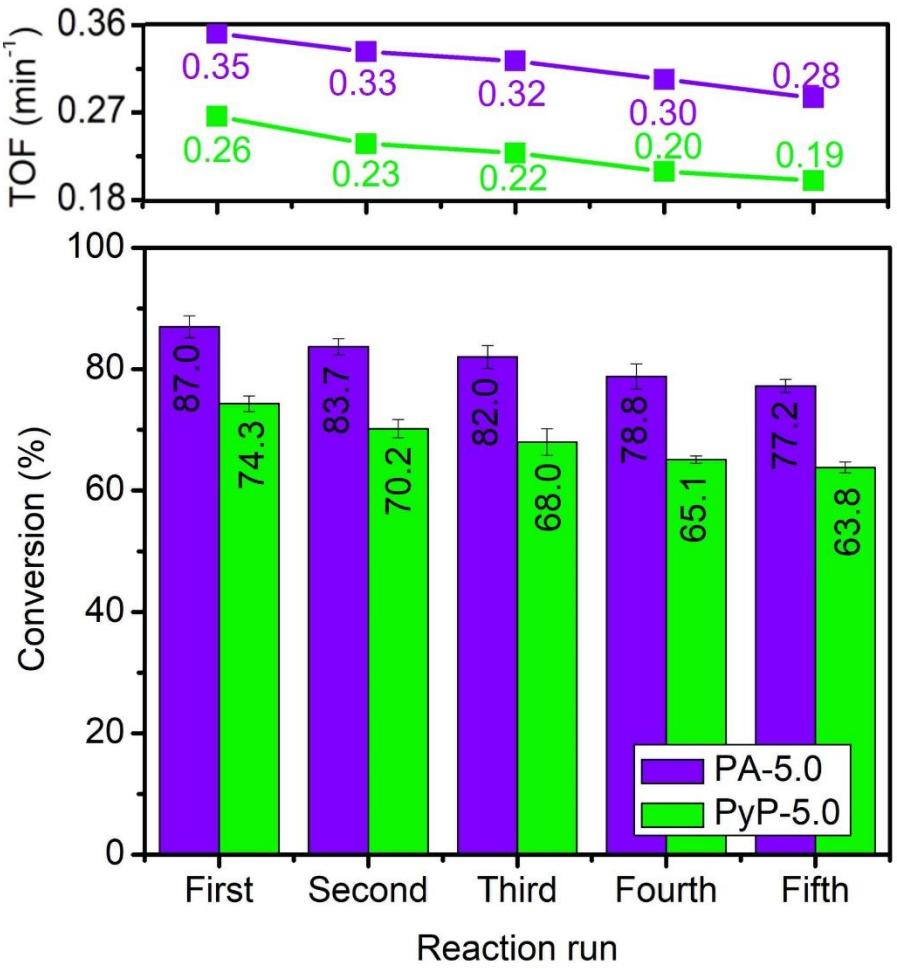

Figure 6.17 Catalyst reusability study of PA-5.0 and PyP-5.0 after five consecutive runs

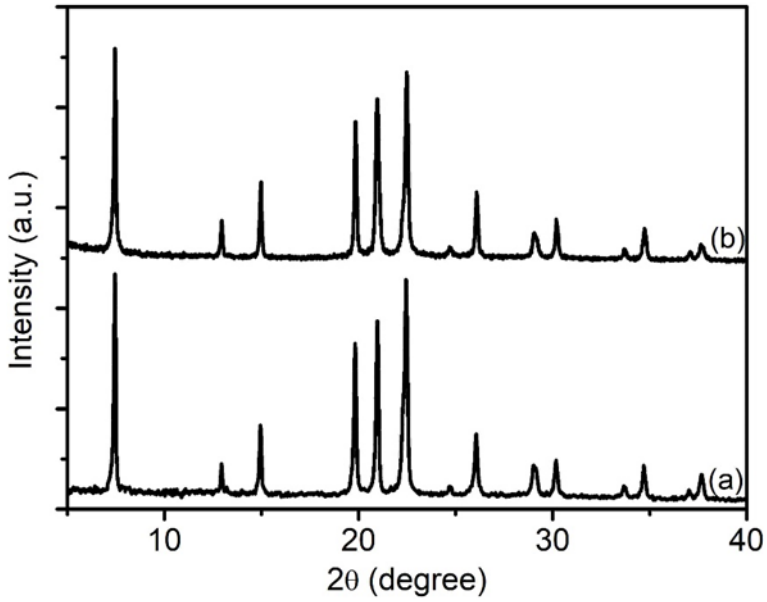

Figure 6.18 XRD patterns of (a) fresh PA-5.0 and (b) PA-5.0 after 5th reaction runs

6.2.8 Mass balance

The theoretical stoichiometric equation for the reaction between EtOH and LcA is illustrated in Table 6.2, showing a balanced reaction where one mole of EtOH reacts with one mole of LcA to produce one mole of ELc. This simplified representation is detailed in Table 6.3, which combines both theoretical and experimental mass balance data for the PA-5.0 SAPO-5 catalyst, providing a comprehensive view essential for accurately determining reactant quantities during experimentation (Appendix 6). According to the Law of Conservation of Mass, the mass entering a system must equal the mass exiting the system, meaning the mass input is equal to the mass output.

However, when comparing the experimental mass balance data for PA-5.0 SAPO-5 with the theoretical model, a slightly inconsistency is observed in the mass of the products formed, where the mass of products (water and ELc is lower than the mass of reactants (LcA and EtOH). This difference arises because some products might still remain in the zeolite pores during the reaction process, and hence lower amount of water and ELc is observed. Nevertheless, the experimental mass balance

only shows small difference from the theoretical one, and this difference is still acceptable.

Table 6.3 Theoretical and experimental mass balance of esterification of LcA and EtOH to produce ELc and water

Substances	**Theoretical**		**Experimental**	
	In (g)	**Out (mg)**	**In (mg)**	**Out (mg)**
Lactic acid	0.0945	0.012	0.0945	0.012
Ethanol	0.482	0.440	0.482	0.435
Ethyl lactate	0	0.108	0	0.113
Water	0.0105	0.027	0.0105	0.017
TOTAL	**0.587**	**0.587**	**0.587**	**0.577**
Error	**0.0%**		**1.7%**	

6.2.9 Thermodynamics of esterification of lactic acid and ethanol

The synthesis of ELc using the PA-5.0 and PyP-5.0 SAPO-5 catalysts influences both the kinetic and thermodynamic properties of the reaction. To elucidate this effect, the thermodynamic parameters (ΔH°_{rxn}, ΔS°_{rxn} and ΔG°_{rxn}) for the esterification of LcA at 160 °C were determined using the following equations:

$$\Delta H^{\circ}_{\mathbf{rxn}} = \Delta H^{\circ}_{\mathbf{298k}} + \int_{298}^{433} \Delta C^{\circ}_{\mathbf{p}} dT \quad (6.7)$$

$$\Delta S^{\circ}_{\mathbf{rxn}} = \Delta S^{\circ}_{\mathbf{298k}} + \int_{298}^{433} \frac{\Delta C^{\circ}_{\mathbf{p}}}{T} dT \quad (6.8)$$

$$\Delta G^{\circ}_{\mathbf{rxn}} = \Delta H^{\circ}_{\mathbf{rxn}} - T\Delta S^{\circ}_{\mathbf{rxn}} \quad (6.9)$$

where the enthalpy change (ΔH°_{vap}) and entropy (ΔS°_{vap}) of vaporization for EtOH, LcA, ELc and water are also included. The energy profiles of the esterification reaction catalyzed by PA-5.0 and PyP-5.0 SAPO-5 are depicted in Figure 6.19. Calculations indicate that the esterification of LcA with EtOH is endothermic reaction

(ΔH°_{rxn} = 8.7 kJ mol^{-1}). Additionally, the ΔG°_{rxn} is −4.3 kJ mol^{-1}, indicating that the reaction is spontaneous at 160 °C. Despite being thermodynamically favorable, the reaction proceeds very slowly without a catalyst, as evidenced by a low conversion of 38.3% at 160 °C after 20 min (Figure 6.11c). Therefore, Gibbs free energy alone cannot explain the reaction rate or conversion efficiency. To address these aspects, the analysis of the chemical kinetics is essential.

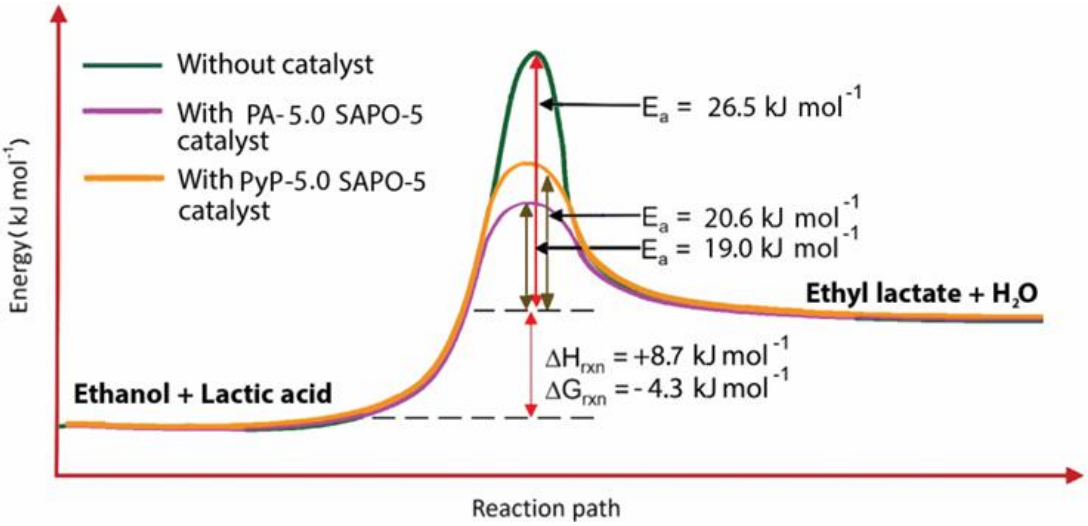

Figure 6.19 Energy profiles of reaction without and with PA-5.0 and PyP-5.0 SAPO-5 catalysts

Reaction kinetics, or rate constants, are highly dependent on temperature. At elevated temperatures, the reaction proceeds at a faster rate, although the activation energy remains unchanged (Atkins & Paula, 2006). This phenomenon can be observed in Section 6.2.1, where an increase in reaction temperature leads to an increase in reaction conversion at the same reaction time.

The presence of the PA-5.0 and PyP-5.0 SAPO-5 catalysts is crucial in the esterification of LcA as they lower the activation energy by providing an alternative reaction pathway (Khan et al., 2021). This pathway allows for the diffusion, adsorption and close proximity of reactant molecules on the active sites of SAPO-5 catalysts before they react and convert into ELc. As a result, this new pathway reduces the

activation energy from 26.5 kJ mol^{-1} to 19.0 kJ mol^{-1} for PA-5.0, and 20.6 kJ mol^{-1} for PyP-5.0.

6.2.10 Proposed catalytic reaction mechanism

Figure 6.20 displays the possible conversion mechanism of LcA and EtOH to ELc by SAPO-5 zeolite as a catalyst. The conversion mechanism of LcA and EtOH to ELc facilitated by SAPO-5 zeolite as a catalyst involves several critical steps. Initially, LcA interacts with the SAPO-5 catalyst, where a proton from the acidic sites of the zeolite is added to the carboxylic acid group of LcA. This protonation enhances the electrophilicity of the carbonyl carbon, making it more susceptible to nucleophilic attack. Subsequently, EtOH, which is activated by the zeolite, attacks the protonated carbonyl carbon, leading to the formation of a tetrahedral intermediate. The hydroxyl group from LcA is integrated into this intermediate structure. The intermediate can then undergo rearrangement to yield ELc, resulting from the loss of a water molecule. This dehydration step is crucial for progressing towards the final product, ELc. Throughout this process, the role of SAPO-5 zeolite is significant, serving as a solid acid catalyst that promotes protonation and enhances the reactivity of the reactants. The structure of the zeolite also contributes to shape selectivity, influencing the formation of the desired products. Furthermore, the utilization of a solid catalyst like SAPO-5 allows for easier product separation and potential catalyst reusability, underscoring its advantages in industrial applications. This mechanism exemplifies the efficacy of heterogeneous catalysts in organic synthesis and highlights a valuable pathway for producing bio-based chemicals from renewable resources.

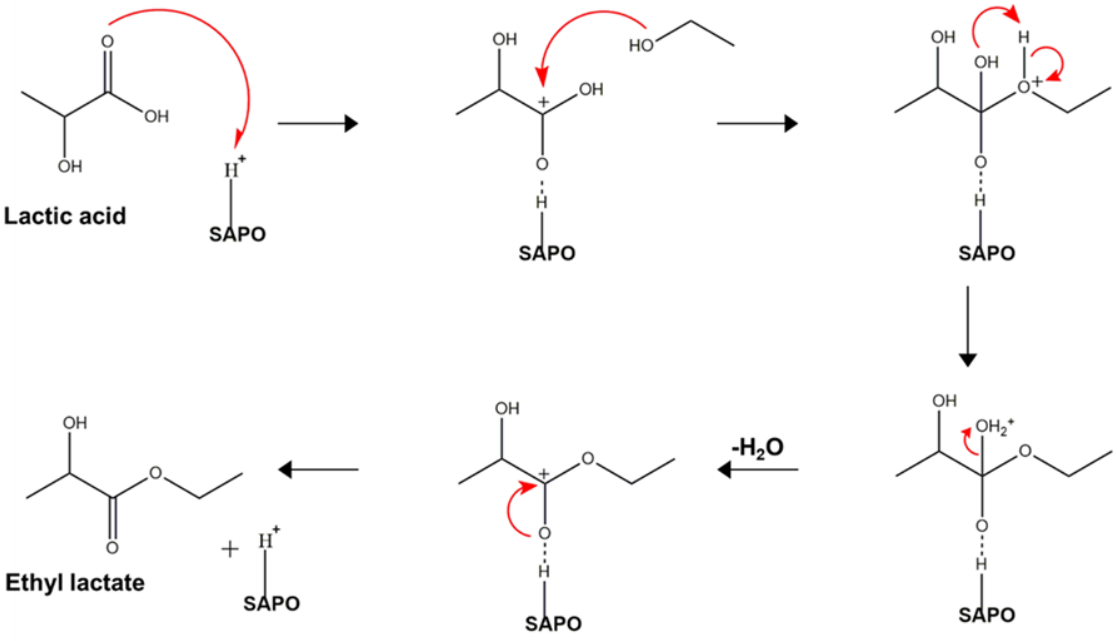

Figure 6.20 Mechanism of esterification of LcA and EtOH to produce ELc

CHAPTER 7

CONCLUSION AND FUTURE RECOMMENDATIONS

7.1 Conclusion

This study has achieved significant advancements in the crystallization and catalytic performance of SAPO materials. The crystallization of SAPO-11 has successfully been accomplished under ionothermal conditions using the novel ionic liquid 1-propylpyridinium bromide ([PPy]Br) as both solvent and structure-directing agent. By carefully optimizing the synthesis parameters such as temperature, phosphorus content, silicon amount, and [PPy]Br concentration, pure SAPO-11 has been crystallized at 150 °C after 133 h of ionothermal heating. This optimization minimizes the formation of undesired crystalline phases such as AFI, berlinite and tridymite. The synthesized SAPO-11 exhibits a high surface area of 149 m^2 g^{-1} with the presence of both Brønsted and Lewis acidities, which are advantageous for catalytic applications.

In addition, the crystallization of SAPO-5 using 5-ethyl-2-methyl-1-propylpyridinium hydroxide ([empy]OH) as a template, with phosphoric acid (H_3PO_4) and pyrophosphoric acid ($H_4P_2O_7$) serving as phosphorus sources, has been explored. The selection of phosphorus source has shown its significant impacts on nucleation, crystal growth and surface acidity. SAPO-5 synthesized with H3PO_4 displayed higher crystallinity that displays a hierarchical structure with intracrystal mesoporosity. Conversely, the use of $H_4P_2O_7$ results in hexagonal SAPO-5 nanoplates with textural mesoporosity. The hierarchical SAPO-5 prepared with H_3PO_4 exhibits a higher hierarchical factor (HF) and acidity compared to those synthesized with $H_4P_2O_7$.

The catalytic performance of SAPO-11 and SAPO-5 has thoroughly been evaluated. For SAPO-11, it demonstrates excellent efficiency in the esterification of

LA with EtOH, giving 93.4% of conversion and 100% selectivity to EL within 30 min at 180 °C under non-microwave instant heating conditions. Its performance has been shown to be better than those of conventional homogeneous catalysts (HCl, H_2SO_4, CH_3COOH).

On the other Similarly, SAPO-5, particularly synthesized with phosphoric acid (PA-5.0), shows much superior catalytic performance in the esterification of LcA with EtOH than SAPO-5 synthesized with pyrophosphoric acid (PyP-5.0). It is shown that PA-5.0 with hierarchical structure and high acidity results in a conversion of 87.0% at 160 °C within 20 min. In contrast, the PyP-5.0 SAPO-5 shows slightly lower conversion rate of 74.3%. Both SAPO-5 catalysts demonstrated good recyclability and selectivity, surpassing traditional acidic catalysts (HCl (100% conversion, 90.1% selectivity), H_3PO_4 (57.1% conversion, 92% selectivity), and H_2SO_4 (100% conversion, 86.3% selectivity)) and other zeolite catalysts (H-MOR (75% conversion, 96.3% selectivity), H-LTL (66.3% conversion, 98.1% selectivity), H-Y(62.6% conversion, 100% selectivity), SAPO-20 (47.4% conversion, 100% selectivity) and SAPO-34 (89.5% conversion, 99.1% selectivity)).

In conclusion, this research highlights the successful development and optimization of SAPO-11 and SAPO-5 materials, showing their effective crystallization and exceptional catalytic performance. The tailored synthesis conditions not only enhance the crystallization processes but also significantly improves the catalytic properties of these materials. These findings pave the way for further advancements in the use of SAPO materials in various catalytic applications and materials science.

7.2 Recommendations for future research

This study provides a comprehensive understanding of the successful crystallization and time-dependent formation of SAPO-11 using a novel ionic liquid (1-propylpyridinium bromide) and the crystallization of SAPO-5 in the presence of a novel 5-ethyl-2-methyl pyridinium hydroxide template with different phosphorus sources. However, the full potential of pyridinium-based organic templates remains largely unexplored. This research lays the groundwork for future studies to expand the application possibilities of pyridinium-based organic templates in zeolite synthesis. The following recommendations are suggested for further research:

1. Conduct a detailed investigation into how other Si and Al sources affect the crystallization behaviour and physicochemical properties of SAPO-5 zeotype materials when using pyridinium-based organic templates. For example, using tetraethoxysilane (TEOS) and HS-40 colloidal silica as comparative Si source, while sodium aluminate and aluminium hydroxide as Al sources and are compared with aluminium isopropoxide in the SAPO zeolite synthesis.
2. Examine the influence of different alkyl chain lengths or functional groups in pyridinium-based organic templates, such as 2-propylpyridinium hydroxide, 1-butylpyridinium hydroxide and 1-benzylpyridinium hydroxide, on the synthesis of SAPO zeolites, considering how the polarity and molecular size may affect the crystallization profiles of zeolites.
3. Synthesize other SAPO zeolites using other pyridinium-based ionic liquid under ionothermal synthesis.
4. Explore the potential applications of SAPO-11 and SAPO-5 in other applications, such as catalytic reactions (acylation, alkylation), sensor and membrane technologies.

REFERENCES

Abbasizadeh, S., & Karimzadeh, R. (2018). Effect of next-nearest-neighbor aluminum atoms in the HZSM-5 framework synthesized with various aluminum sources on liquefied petroleum gas transformation to light olefins. *Industrial & Engineering Chemistry Research*, *57*, 7783-7794.

Abdullahi, H., Wong, K.-L., Lim, G. K., Awala, H., Vicente, A., Ling, T. C., Mintova, S., & Ng, E.-P. (2019). Effects of various alkali metal cations on the synthesis, crystallization and catalytic properties of NKX-2 aluminophosphites. *Materials Chemistry and Physics*, *222*, 81-86.

Adam, F., Kueh, C.-W., & Ng, E.-P. (2013). The immobilization of iron (III) aminopyridine complex on MCM-41: Its preparation and characterization. *Journal of Porous Materials*, *20*, 1337-1343.

Ahmad, E., Alam, M. I., Pant, K., & Haider, M. A. (2016). Catalytic and mechanistic insights into the production of ethyl levulinate from biorenewable feedstocks. *Green Chemistry*, *18*, 4804-4823.

Ahmad, N. H., Daou, T. J., Maireles-Torres, P., Zaarour, M., Mintova, S., Ling, T.-C., & Ng, E.-P. (2020). Morphological effects on catalytic performance of LTL zeolites in acylation of 2-methylfuran enhanced by non-microwave instant heating. *Materials Chemistry and Physics*, *244*, 122688.

Ahmed, M., & Sakthivel, A. (2019). Amine functionalized AFI type microporous SAPO-5 materials: preparation, unique method on template extraction, characterization and its catalytic application on epoxide ring opening. *Journal of Porous Materials*, *26*, 319-326.

Alfonzo, M., Goldwasser, J., López, C., Machado, F., Matjushin, M., Méndez, B., & de Agudelo, M. R. (1995). Effect of the synthesis conditions on the crystallinity and surface acidity of SAPO-11. *Journal of Molecular Catalysis A: Chemical*, *98*, 35-48.

Ali, D., Zeiger, C. R., Azim, M. M., Lein, H. L., Mathisen, K. J. M., & Materials, M. (2020). Evaluation of surfactant templates for one-pot hydrothermal synthesis of hierarchical SAPO-5. *Microporous and Mesoporous Materials, 306*, 110364.

Ashokan, A., Rajendran, V., Kumar, T. S., & Jayaraman, G. (2021). Eggshell derived hydroxyapatite microspheres for chromatographic applications by a novel dissolution-precipitation method. *Ceramics International, 47*, 18575-18583.

Askari, S., Siahmard, A. B., Halladj, R., & Alipour, S. M. (2016). Different techniques and their effective parameters in nano SAPO-34 synthesis: A review. *Powder Technology, 301*, 268-287.

Ates, A. (2019). The modification of aluminium content of natural zeolites with different composition. *Powder Technology*, *344*, 199-207.

Atkins, P., & De Paula, J. (2006). *Physical chemistry* (Vol. 1). Macmillan, City University of New York, Brooklyn, New York.

Auwal, I. A., Mintova, S., Ling, T. C., Khoerunnisa, F., Wong, K.-L., & Ng, E.-P. (2020). Crystallization profile and morphological study of SAPO-5 templated by imidazolium cations of different functional groups. *Microporous and Mesoporous Materials, 308*, 110514.

Auwal, I. A., Wong, K.-L., Ling, T. C., Ooi, B. S., & Ng, E.-P. (2020). Metal chlorides grafted on SAPO-5 (MCl_x/SAPO-5) as reusable and superior catalysts for acylation of 2-methylfuran under non-microwave instant heating condition. *Processes, 8*, 603.

Baerlocher, C., & McCusker, L. (2017). *Database of Zeolite Structures* Database of Zeolite Structures. Retrieved January 5, 2023, http://www.iza-structure.org/databases/

Baile, P., Fernández, E., Vidal, L., & Canals, A. (2019). Zeolites and zeolite-based materials in extraction and microextraction techniques. *Analyst*, *144*, 366-387.

Baláž, M. (2021). *Environmental mechanochemistry*. Springer, Cham.

Barrer, R. M. (1982). *Hydrothermal chemistry of zeolites.* Academic Press, London.

Basina, G., AlShami, D., Polychronopoulou, K., Tzitzios, V., Balasubramanian, V., Dawaymeh, F., Georgios, N. K., & Al Wahedi, Y. (2018). Hierarchical $AlPO_4$-5 and SAPO-5 microporous molecular sieves with mesoporous connectivity for water sorption applications. *Surface and Coatings Technology*, *353*, 378-386.

Bellatreche, S., Hasnaoui, A., Boukoussa, B., García-Aguilar, J., Berenguer-Murcia, Á., Cazorla-Amoros, D., & Bengueddach, A. (2016). Structural and textural features of TiO_2/SAPO-34 nanocomposite prepared by the sol–gel method. *Research on Chemical Intermediates*, *42*, 8039-8053.

Bing, L., Li, F., Li, Q., Lei, Y., Ji, S., Han, D., Wang, F., & Wang, G. (2020). One-pot synthesis of core-shell structured SSZ-13 zeolite using aluminum isopropoxide as an aluminum source. *Materials Letters*, *266*, 127497.

Bing, L., Peng, T., Yue, Q., ZHANG, L., Shutao, X., Xiong, S., Dong, F., & Zhongmin, L. (2013). Study of crystallization process of SAPO-11 molecular sieve. *Chinese Journal of Catalysis, 34*, 593-603.

Blasco, T., Chica, A., Corma, A., Murphy, W., Agúndez-Rodríguez, J., & Pérez-Pariente, J. (2006). Changing the Si distribution in SAPO-11 by synthesis with surfactants improves the hydroisomerization/dewaxing properties. *Journal of Catalysis, 242*, 153-161.

Bleta, R., Ponchel, A., & Monflier, E. (2018). Cyclodextrin-based supramolecular assemblies: a versatile toolbox for the preparation of functional porous materials. *Environmental Chemistry Letters*, *16*, 1393-1413.

Boltz, M. (2014). Tailor-made conception of zeolites for catalysis: From the active site to the reactor. [Doctoral dissertation, University of Strasbourg], Strasbourg.

Bougault, H., Dpt, M. G. J. M., & techniques, c. L. (2019). Hydrothermal hydrogen and methane: scientific insight a new potential resource?. *196*, 73-80.

Bruice, P. Y. (2017). *Organic chemistry*. Pearson, London.

Butt, J. (2012). *Activation, deactivation, and poisoning of catalysts*. Elsevier, Amsterdam.

Byrappa, K., & Kumar, B. S. (2007). Characterization of zeolites by infrared spectroscopy. *Asian Journal of Chemistry*, *19*, 4933.

Cai, R., Sun, M., Chen, Z., Munoz, R., O'Neill, C., Beving, D. E., & Yan, Y. (2008). Ionothermal synthesis of oriented zeolite AEL films and their application as corrosion-resistant coatings. *Angewandte Chemie International Edition, 47*, 525-528.

Chai, Y., Dai, W., Wu, G., Guan, N., & Li, L. (2021). Confinement in a zeolite and zeolite catalysis. *Accounts of Chemical Research*, *54*, 2894-2904.

Chen, C.-T., Iyoki, K., Yonezawa, Y., Okubo, T., & Wakihara, T. (2020). Understanding the nucleation and crystal growth of zeolites: a case study on the crystallization of ZSM-5 from a hydrogel system under ultrasonication. *T he Journal of Physical Chemistry C, 124*, 11516-11524.

Chen, D., Tang, Q., Deng, W., Chaianansutcharit, S., & Guo, L. (2022). Comparative studies on the toluene sorption performance over silicalite-1 zeolites with different morphologies. *Microporous and Mesoporous Materials*, *346*, 112275.

Chen, X., Meng, X., & Xiao, F.-s. (2015). Solvent-free synthesis of SAPO-5 zeolite with plate-like morphology in the presence of surfactants. *Chinese Journal of Catalysis*, *36*, 797-800.

Chen, Z., Dong, Y., Jiang, S., Song, W., Lai, W., Yi, X., & Fang, W. (2017). Low-temperature synthesis of hierarchical architectures of SAPO-11 zeolite as a good hydroisomerization support. *Journal of Materials Science*, *52*, 4460-4471.

Choo, M.-Y., Juan, J. C., Oi, L. E., Ling, T. C., Ng, E.-P., Noorsaadah, A. R., Centi, G., Lee, K. T. (2019). The role of nanosized zeolite Y in the H_2-free catalytic deoxygenation of triolein. *Catalysis Science & Technology*, *9*, 772-782.

Choo, M.-Y., Oi, L. E., Ling, T. C., Ng, E.-P., Lin, Y.-C., Centi, G., & Juan, J. C. (2020). Deoxygenation of triolein to green diesel in the H_2-free condition: Effect of transition metal oxide supported on zeolite Y. *Journal of Analytical and Applied Pyrolysis*, *147*, 104797.

Cooper, E. R., Andrews, C. D., Wheatley, P. S., Webb, P. B., Wormald, P., & Morris, R. E. (2004). Ionic liquids and eutectic mixtures as solvent and template in synthesis of zeolite analogues. *Nature*, *430*, 1012-1016.

Dai, X., Cheng, Y., Si, M., Wei, Q., Chen, D., Huang, W., & Zhou, Y. (2022). SAPO-11 molecular sieves synthesized in alcohol-water concentrated gel system with improved acidity, mesoporous volume and hydroisomerization performance. *Fuel*, *314*, 123131.

Dai, X., Cheng, Y., Wei, Q., Si, M., & Zhou, Y. (2022). Small-crystal and hierarchical SAPO-11 molecular sieve synthesized via three-stage crystallization method and hydroisomerization performance of corresponding NiWS supported catalyst. *Fuel, 324*, 124610.

Dalal, A., Nehra, K., Hooda, A., Singh, D., Kumar, P., Kumar, S., Malik, R. S., Rathi, B. (2023). Luminous lanthanide diketonates: Review on synthesis and optoelectronic characterizations. *Inorganica Chimica Acta*, 121406.

Delgado, P., Sanz, M. T., Beltrán, S., & Núñez, L. A. (2010). Ethyl lactate production via esterification of lactic acid with ethanol combined with pervaporation. *Chemical Engineering Journal, 165*, 693-700.

Deneyer, A., Ke, Q., Devos, J., & Dusselier, M. (2020). Zeolite synthesis under nonconventional conditions: reagents, reactors, and modi operandi. *Chemistry of Materials*, *32*, 4884-4919.

Di, C.-Y., Li, X.-F., Wang, P., Li, Z.-H., Fan, B.-B., & Dou, T. (2017). Green and efficient dry gel conversion synthesis of SAPO-34 catalyst with plate-like morphology. *Petroleum Science*, *14*, 203-213.

Díaz, M. J., Ruiz-Montoya, M., Palma, A., & de-Paz, M.-V. (2021). Thermogravimetry applicability in compost and composting research: A review. *Applied Sciences*, *11*, 1692.

Doan, T., Nguyen, K., Dam, P., Vuong, T. H., Le, M. T., & Thanh, H. P. J. J. o. C. (2019). Synthesis of SAPO-34 Using Different Combinations of Organic Structure-Directing Agents. *Wiley Online Library, 2019*, 6197527.

Donohue, M. D., & Aranovich, G. L. (1998). Classification of Gibbs adsorption isotherms. *Advances in Colloid and Interface Science*, *76*, 137-152.

Du, R.-L., Wu, K., Xu, D.-A., Chao, C.-Y., Zhang, L., & Du, X.-D. (2016). A modified Arrhenius equation to predict the reaction rate constant of Anyuan pulverized-coal pyrolysis at different heating rates. *Fuel Processing Technology*, *148*, 295-301.

Du, Y., Feng, B., Jiang, Y., Yuan, L., Huang, K., & Li, J. (2018). Solvent-Free Synthesis and n‐Hexadecane Hydroisomerization Performance of SAPO-11 Catalyst. *European Journal of Inorganic Chemistry*, *2018*, 2599-2606.

Dudek, M. K., Kazmierski, S., Kostrzewa, M., & Potrzebowski, M. J. (2018). Solid-state NMR studies of molecular crystals. *Annual Reports on NMR Spectroscopy*, *95*, 1-81.

Dusselier, M., & Davis, M. E. (2018). Small-pore zeolites: synthesis and catalysis. *Chemical Reviews*, *118*, 5265-5329.

Dutta, A. (2017). Fourier transform infrared spectroscopy. *Spectroscopic methods for nanomaterials characterization* (pp. 73–93). Elsevier, Amsterdam.

Falaki, F. (2019). Sample preparation techniques for gas chromatography. In *Gas Chromatography-Derivatization, Sample Preparation, Application*. IntechOpen, London.

Falciglia, P. P., Roccaro, P., Bonanno, L., De Guidi, G., Vagliasindi, F. G., & Romano, S. (2018). A review on the microwave heating as a sustainable technique for environmental remediation/detoxification applications. *Renewable and Sustainable Energy Reviews*, *95*, 147-170.

Fedeyko, J. M., Rimer, J. D., Lobo, R. F., & Vlachos, D. G. (2004). Spontaneous formation of silica nanoparticles in basic solutions of small tetraalkylammonium cations. *The Journal of Physical Chemistry B, 108*, 12271-12275.

Feliczak-Guzik, A. (2018). Hierarchical zeolites: Synthesis and catalytic properties. *Microporous and Mesoporous Materials*, *259*, 33-45.

Feng, J., Guo, L., Wang, Z., Wang, B., Wang, J., Lu, T., Xu, J., Zhan, Y., Rawal, A., Zhao, C., & Han, L. (2019). Effect of Ionothermal Synthesis on the Acidity and Catalytic Performance of a SAPO-5 Molecular Sieve. *ChemistrySelect, 4*, 10520-10524.

Fletcher, R. E. (2019). *The Location and Effect of Aluminium in Zeolites* UCL (University College London)], London.

Fortas, W., Djelad, A., Hasnaoui, M., Sassi, M., & Bengueddach, A. (2018). Adsorption of gentian violet dyes in aqueous solution on microporous AlPOs molecular sieves synthesized by ionothermal method. *Materials Research Express, 5*, 025018.

Foster, A. J. (2013). *Catalytic deoxygenation of biomassderivatives for the production of fuels and chemicals*. [Doctoral dissertation, University of Delaware], Newark.

Fraga-Corral, M., Otero, P., Cassani, L., Echave, J., Garcia-Oliveira, P., Carpena, M., Chamorro, F., Lourenço-Lopes, C., Prieto, M. A., & Simal-Gandara, J. (2021). Traditional applications of tannin rich extracts supported by scientific data: Chemical composition, bioavailability and bioaccessibility. *Foods, 10*, 251.

Gackowski, M., Podobiński, J., Broclawik, E., & Datka, J. (2019). IR and NMR Studies of the status of Al and acid sites in desilicated zeolite Y. *Molecules, 25*, 31.

Gao, B., Tian, P., Li, M., Yang, M., Qiao, Y., Wang, L., Xu, S., & Liu, Z. (2015). In situ growth and assembly of microporous aluminophosphate nanosheets into ordered architectures at low temperature and their enhanced catalytic performance. *Journal of Materials Chemistry A, 3*, 7741-7749.

Ge, L., Li, W., Li, S., Yu, G., Li, W., Qiu, M., & Chen, X. (2022). Designed synthesis of single-crystalline silicoaluminophosphate zeolite via interzeolite transformation for n-dodecane hydroisomerization. *Microporous and Mesoporous Materials*, *330*, 111568.

Geng, L., Dong, H., Liu, X., & Zhang, B. (2018). Efficient manipulation of continuous AFI-type aluminophosphate membranes with distinctive microstructures on macroporous α-Al_2O_3 substrates. *Molecules*, *23*, 1127.

Gharibeh, M., Tompsett, G., & Conner, W. (2008). Microwave reaction enhancement: the rapid synthesis of SAPO-11 molecular sieves. *Topics in Catalysis*, *49*, 157-166.

Gomes, G. J., Dal Pozzo, D. M., Zalazar, M. F., Costa, M. B., Arroyo, P. A., & Bittencourt, P. R. (2019). Oleic acid esterification catalyzed by zeolite Y-model of the biomass conversion. *Topics in Catalysis*, *62*, 874-883.

Gordina, N., Prokof'ev, V. Y., & Il'in, A. (2003). Synthesis of NaA zeolite by mechanochemical methods. *Russian Journal of Applied Chemistry*, *76*, 661-662.

Grabias-Blicharz, E., Panek, R., Franus, M., & Franus, W. (2022). Mechanochemically assisted coal fly ash conversion into zeolite. *Materials, 15*, 7174.

Grand, J., Awala, H., & Mintova, S. (2016). Mechanism of zeolites crystal growth: new findings and open questions. *CrystEngComm*, *18*, 650-664.

Guangyu, L., Peng, T., & Zhongmin, L. (2012). Synthesis of SAPO-34 molecular sieves templated with diethylamine and their properties compared with other templates. *Chinese Journal of Catalysis*, *33*, 174-182.

Guo, F., Peng, K., Liang, S., Jia, X., Jiang, X., & Qian, L. (2019). Evaluation of the catalytic performance of different activated biochar catalysts for removal of tar from biomass pyrolysis. *Fuel, 258*, 116204.

Guzman Barrera, N. I. (2018). *Eco-compatible syntheses of bio-based solvents for the paint and coating industry.* [Doctoral dissertation, Institut National Polytechnique de Toulouse - INPT], Toulouse.

Han, L., Yan, X., Guo, L., Duan, Y., Wang, Z., Lu, T., Xu, J., Zhang, Y.,Wang, J. (2021). Ionothermal Synthesis of Triclinic SAPO-34 Zeolites. *Catalysts*, *11*, 616.

Han, Y., Wu, W., Li, N., Yu, X., Cao, Y., Xue, M., & Yu, T. (2023). Ionothermal Synthesis of Zeotype Materials for Catalysis, Separation and Coatings. *Journal of Molecular Liquids,* 122529.

Hirota, Y., Murata, K., Tanaka, S., Nishiyama, N., Egashira, Y., & Ueyama, K. (2010). Dry gel conversion synthesis of SAPO-34 nanocrystals. *Materials Chemistry and Physics*, *123*, 507-509.

Hu, E., Lai, Z., & Wang, K. (2010). Adsorption properties of the SAPO-5 molecular sieve. *Journal of Chemical & Engineering Data*, *55*, 3286-3289.

Huseynova, G., Aliyeva, N., & Rashidova, S. (2022). Zeolite-containing catalysts in alkylation processes. *Catalysis Research*, *2*, 1-12.

Hussain, S. Z., & Maqbool, K. (2014). GC-MS: Principle, Technique and its application in Food Science. *International Journal of Current Science*, *13*, 116-126.

Hodges, J. M., Morse, J. R., Fenton, J. L., Ackerman, J. D., Alameda, L. T., & Schaak, R. E. J. C. o. M. (2017). Insights into the seeded-growth synthesis of colloidal hybrid nanoparticles. *29*, 106-119.

Ijaola, A. O., Farayibi, P. K., & Asmatulu, E. (2020). Superhydrophobic coatings for steel pipeline protection in oil and gas industries: A comprehensive review. *Journal of Natural Gas Science and Engineering, 83*, 103544.

Ishii, M., Jorge, S. D., de Oliveira, A. A., Palace-Berl, F., Sonehara, I. Y., Pasqualoto, K. F. M., & Tavares, L. C. (2011). Synthesis, molecular modeling and preliminary biological evaluation of a set of 3-acetyl-2,5-disubstituted-2,3-dihydro-1,3,4-oxadiazole as potential antibacterial, anti-Trypanosoma cruzi

and antifungal agents. *Bioorganic & Medicinal Chemistry*, *19*, 6292-6301.

Itakura, M., Goto, I., Takahashi, A., Fujitani, T., Ide, Y., Sadakane, M., & Sano, T. (2011). Synthesis of high-silica CHA type zeolite by interzeolite conversion of FAU type zeolite in the presence of seed crystals. *Microporous and Mesoporous Materials*, *144*, 91-96.

IZA. (2024). *Database of zeolite structures.* Retrieved August 5, 2024 https://www.iza-structure.org/databases/

Jadav, D., Bandyopadhyay, R., & Bandyopadhyay, M. (2020). Synthesis of Hierarchical SAPO-5 & SAPO-34 Materials by Post-Synthetic Alkali Treatment and Their Enhanced Catalytic Activity in Transesterification. *European Journal of Inorganic Chemistry, 2020*, 847-853.

Jelfs, K. E., Slater, B., Lewis, D. W., & Willock, D. J. (2007). The role of organic templates in controlling zeolite crystal morphology. *Studies in Surface Science and Catalysis*, *170*, 1685-1692.

Jhung, S. H., Chang, J.-S., Hwang, Y. K., & Park, S.-E. (2004). Crystal morphology control of AFI type molecular sieves with microwave irradiation. *Journal of Materials Chemistry, 14*, 280-285.

Kadja, G. T., Fabiani, V. A., Aziz, M. H., Fajar, A. T., Prasetyo, A., Suendo, V., Ng, E. P., & Mukti, R. R. (2017). The effect of structural properties of natural silica precursors in the mesoporogen-free synthesis of hierarchical ZSM-5 below 100° C. *Advanced Powder Technology, 28*, 443-452.

Keoh, S. H., Chaikittisilp, W., Muraoka, K., Mukti, R. R., Shimojima, A., Kumar, P., Tsapatsis, M., & Okubo, T. (2016). Factors governing the formation of hierarchically and sequentially intergrown MFI zeolites by using simple diquaternary ammonium structure-directing agents. *Chemistry of Materials, 28*, 8997-9007.

Khaleque, A., Alam, M. M., Hoque, M., Mondal, S., Haider, J. B., Xu, B., Johir, M. A. H., Karamakar, A. K., Zhou, J. L., & Ahmed, M. B. (2020). Zeolite synthesis from low-cost materials and environmental applications: A review. *Environmental Advances*, *2*, 100019.

Khan, Z., Javed, F., Shamair, Z., Hafeez, A., Fazal, T., Aslam, A., Zimmerman, W. B., & Rehman, F. (2021). Current developments in esterification reaction: A review on process and parameters. *Journal of Industrial and Engineering Chemistry, 103*, 80-101.

Khoo, D. Y., Awala, H., Mintova, S., & Ng, E.-P. (2014). Synthesis of AlPO-5 with diol-substituted imidazolium-based organic template. *Microporous and Mesoporous Materials, 194*, 200-207.

Khoo, D. Y., Kok, W.-M., Mukti, R. R., Mintova, S., & Ng, E.-P. (2013). Ionothermal approach for synthesizing AlPO-5 with hexagonal thin-plate morphology influenced by various parameters at ambient pressure. *Solid State Sciences*, *25*, 63-69.

Kiss, A. A., Dimian, A. C., & Rothenberg, G. (2006). Solid acid catalysts for biodiesel Production - Towards sustainable energy. *Advanced Synthesis & Catalysis*, *348*, 75-81.

Klunk, M. A., Das, M., Dasgupta, S., Impiombato, A. N., Caetano, N. R., Wander, P. R., & Moraes, C. A. M. (2020). Comparative study using different external sources of aluminum on the zeolites synthesis from rice husk ash. *Materials Research Express*, *7*, 015023.

Komesu, A., Wolf Maciel, M. R., Rocha de Oliveira, J. A., da Silva Martins, L. H., & Maciel Filho, R. (2017). Purification of lactic acid produced by fermentation: focus on non-traditional distillation processes. *Separation & Purification Reviews*, *46*, 241-254.

Kosslick, H., & Fricke, R. (2006). Chemical analysis of aluminosilicates, aluminophosphates and related molecular sieves. *Characterization II* (pp. 1-66). Springer, Cham.

Krachuamram, S., Chanapattharapol, K. C., & Kamonsutthipaijit, N. (2021). Synthesis and characterization of NaX-type zeolites prepared by different silica and alumina sources and their CO_2 adsorption properties. *Microporous and Mesoporous Materials*, *310*, 110632.

Kumar, A., Rana, S., Sharma, G., Dhiman, P., Shekh, M. I., & Stadler, F. J. (2023). Recent advances in zeolitic imidazole frameworks based photocatalysts for organic pollutant degradation and clean energy production. *Journal of Environmental Chemical Engineering*, *11*, 110770.

Kumar, K. V., Gadipelli, S., Wood, B., Ramisetty, K. A., Stewart, A. A., Howard, C. A., brett, D. J. L., & Rodriguez-Reinoso, F. (2019). Characterization of the adsorption site energies and heterogeneous surfaces of porous materials. *Journal of Materials Chemistry A*, *7*, 10104-10137.

Kumar, N., Villegas, J. I., Salmi, T., Murzin, D. Y., & Heikkilä, T. (2005). Isomerization of n-butane to isobutane over Pt-SAPO-5, SAPO-5, Pt-H-mordenite and H-mordenite catalysts. *Catalysis Today*, *100*, 355-361.

Kuwahara, Y., Ohmichi, T., Kamegawa, T., Mori, K., & Yamashita, H. (2010). A novel conversion process for waste slag: synthesis of a hydrotalcite-like compound and zeolite from blast furnace slag and evaluation of adsorption capacities. *Journal of Materials Chemistry*, *20*, 5052-5062.

Lamberti, F. M., Ingram, A., & Wood, J. (2021). Synergistic dual catalytic system and kinetics for the alcoholysis of poly (lactic acid). *Processes, 9*, 921.

Leal Silva, J. F., Grekin, R., Mariano, A. P., & Maciel Filho, R. (2018). Making levulinic acid and ethyl levulinate economically viable: a worldwide technoeconomic and environmental assessment of possible routes. *Energy Technology*, *6*, 613-639.

Lee, Y.-J., Baek, S.-C., & Jun, K.-W. (2007). Methanol conversion on SAPO-34 catalysts prepared by mixed template method. *Applied Catalysis A: General*, *329*, 130-136.

Lei, T., Wang, Z., Li, Y., Li, Z., He, X., & Zhu, J. (2013). Performance of a Diesel Engine with Ethyl Levulinate-Diesel Blends: A Study using Grey Relational Analysis. *BioResources*, *8,* 2696-2707.

Lesthaeghe, D., Vansteenkiste, P., Verstraelen, T., Ghysels, A., Kirschhock, C. E., Martens, J. A., Van Speybroeck, V., & Waroquier, M. (2008). MFI fingerprint: How pentasil-induced IR bands shift during zeolite nanogrowth. *The Journal of Physical Chemistry C*, *112*, 9186-9191.

Li, H., Zhao, Z., Xiouras, C., Stefanidis, G. D., Li, X., & Gao, X. (2019). Fundamentals and applications of microwave heating to chemicals separation processes. *Renewable and Sustainable Energy Reviews, 114*, 109316.

Li, M., Zeng, C., & Zhang, L. (2012). Hydrothermal synthesis of SAPO-5 with novel morphologies from hydrogels containing acetic acid and high concentration of triethylamine under neutral or alkaline conditions. *CrystEngComm*, *14*(10), 3787-3792.

Li, Y., Liang, G., Chang, L., Zi, C., Zhang, Y., Peng, Z., & Zhao, W. (2021). Conversion of biomass ash to different types of zeolites: a review. *Energy Sources, Part A: Recovery, Utilization, and Environmental Effects*, *43*, 1745-1758.

Li, Y., Liu, R., Guo, Q., Bian, H., Lan, A., Li, X., Han, P., & Dou, T. J. J. o. P. M. (2019). Efficient synthesis of high silica SSZ-13 zeolite via a steam-assisted crystallization process. *Journal of Porous Materials, 26*, 1879-1888.

Li, Y., & Yang, W. (2008). Microwave synthesis of zeolite membranes: A review. *Journal of Membrane Science*, *316*, 3-17.

Li, Y., & Yu, J. (2021). Emerging applications of zeolites in catalysis, separation and host-guest assembly. *Nature Reviews Materials*, *6*, 1156-1174.

Lima, G. C., Mello, M. I., Bieseki, L., Araujo, A. S., & Pergher, S. B. (2021). Hydrothermal Synthesis of Silicoaluminophosphate with AEL Structure Using a Residue of Fluorescent Lamps as Starting Material. *Molecules*, *26*, 7366.

Lin, Y., Wei, Y., Zhang, L., Guo, K., Wang, M., Huang, P., Meng, X., & Zhang, R. (2019). Facile ionothermal synthesis of SAPO-LTA zeotypes with high structural stability and their catalytic performance in MTO reaction. *Microporous and Mesoporous Materials, 288*, 109611.

Liu, C., Li, G., Hensen, E. J., & Pidko, E. A. J. J. o. C. (2016). Relationship between acidity and catalytic reactivity of faujasite zeolite: A periodic DFT study. *J. Catal, 344*, 570-577.

Liu, K., Zakharova, N., Adeyilola, A., & Zeng, L. (2021). Experimental study on the pore shape damage of shale samples during the crushing process. *Energy & Fuels, 35*, 2183-2191.

Liu, P., Ren, J., & Sun, Y. (2008). Influence of template on Si distribution of SAPO-11 and their performance for n-paraffin isomerization. *Microporous and Mesoporous Materials*, *114*, 365-372.

Liu, Q., Wang, D., Li, Z., Li, Z., Peng, X., Liu, C., Zhang, Y., & Zheng, P. (2020). Recent developments in the flame-retardant system of epoxy resin. *Materials*, *13*, 2145.

Liu, Y., Cui, X., Han, L., Yu, Z., & Liu, X. (2014). Role of fluoride ions in synthesis and isomerization performance of superfine SAPO-11 zeolite. *Microporous and Mesoporous Materials*, *198*, 230-235.

Lodrijeh, S. R., Askari, S., & Halladj, R. (2021). Seeding-induced nano-sized SAPO-34 synthesis with superior MTO performance: Energy-efficient approach with highly reduced OSDA consumption. *Powder Technology, 389*, 383-391.

Ma, H., Xu, R., You, W., Wen, G., Wang, S., Xu, Y., Wang, B., Wang, L., Wei, Y., Xu, Y., Zhang, W., Tian, Z., & Lin, L. (2009). Ionothermal synthesis of gallophosphate molecular sieves in 1-alkyl-3-methyl imidazolium bromide ionic liquids. *Microporous and Mesoporous Materials, 120*, 278-284.

Ma, Y.-K., Chia, S., Daou, T. J., Khoerunnisa, F., El-Bahy, S. M., El-Bahy, Z. M., Ling T. C., & Ng, E.-P. (2022). SAPO-34 crystallized using novel pyridinium template as highly active catalyst for synthesis of ethyl levulinate biofuel. *Microporous and Mesoporous Materials*, *333*, 111754.

Ma, Y.-K., Chia, S., Paillaud, J.-L., Daou, T. J., Khoerunnisa, F., El-Bahy, Z. M., Ling T. C., Altalhi, A. A., Mahmoud, S. F., & Ng, E.-P. (2022). SAPO-35 zeolite crystallized using novel structure-directing agent for catalytic conversion of levulinic acid into ethyl levulinate under non-microwave instant heating. *Materials Chemistry and Physics*, *287*, 126240.

Ma, Y.-K., Rigolet, S., Michelin, L., Paillaud, J.-L., Mintova, S., Khoerunnisa, F., Daou, T. J., & Ng, E.-P. (2021). Facile and fast determination of Si/Al ratio of zeolites using FTIR spectroscopy technique. *Microporous and Mesoporous Materials, 311*, 110683.

Ma, Y., Li, N., Ren, X., Xiang, S., & Guan, N. (2006). Synthesis of SAPO-41 from a new reproducible route using H_3PO_3 as the phosphorus source and its application in hydroisomerization of n-decane. *Journal of Molecular Catalysis A: Chemical, 250*, 9-14.

Majano, G., Ng, E.-P., Lakiss, L., & Mintova, S. (2011). Nanosized molecular sieves utilized as an environmentally friendly alternative to antioxidants for lubricant oils. *Green Chemistry, 13*, 2435-2440.

Marturano, V., Cerruti, P., & Ambrogi, V. (2017). Polymer additives. *Physical Sciences Reviews*, *2*, 20160130.

Maton, C., De Vos, N., & Stevens, C. V. (2013). Ionic liquid thermal stabilities: decomposition mechanisms and analysis tools. *Chemical Society Reviews*, *42*, 5963-5977.

Mei, J., Duan, A., & Wang, X. (2021). A brief review on solvent-free synthesis of zeolites. *Materials*, *14*(4), 788.

Meldrum, F. C., & O'Shaughnessy, C. (2020). Crystallization in confinement. *Advanced Materials*, *32*, 2001068.

Meng, X., & Xiao, F.-S. (2014). Green routes for synthesis of zeolites. *Chemical Reviews*, *114*, 1521-1543.

Millini, R., & Bellussi, G. (2017). Zeolite science and perspectives.

Mintova, S., Mo, S., & Bein, T. (1998). Nanosized $AlPO_4$-5 molecular sieves and ultrathin films prepared by microwave synthesis. *Chemistry of Materials, 10*, 4030-4036.

Mishra, R. R., & Sharma, A. K. (2016). Microwave–material interaction phenomena: Heating mechanisms, challenges and opportunities in material processing. *Composites Part A: Applied Science and Manufacturing, 81*, 78-97.

Montemore, M. M., Van Spronsen, M. A., Madix, R. J., & Friend, C. M. (2017). O_2 activation by metal surfaces: implications for bonding and reactivity on heterogeneous catalysts. *Chemical Reviews*, *118*, 2816-2862.

Mora, A.-S., Tayouo, R., Boutevin, B., David, G., & Caillol, S. (2020). A perspective approach on the amine reactivity and the hydrogen bonds effect on epoxy-amine systems. *European Polymer Journal*, *123*, 109460.

Morris, R. E. (2009). Ionothermal synthesis—ionic liquids as functional solvents in the preparation of crystalline materials. *Chemical Communications*, 2990-2998.

Mortén, M., Mentel, Ł., Lazzarini, A., Pankin, I. A., Lamberti, C., Bordiga, S., Crocellà, V., Svelle, S., Lillerud, K. P., & Olsbye, U. (2018). A Systematic Study of Isomorphically Substituted H-MAlPO-5 Materials for the Methanol-to-Hydrocarbons Reaction. *ChemPhysChem, 19*, 484-495.

Moshoeshoe, M., Nadiye-Tabbiruka, M. S., & Obuseng, V. (2017). A review of the chemistry, structure, properties and applications of zeolites. *Am. J. Mater. Sci*, *7*, 196-221.

Ng, E.-P., Awala, H., Komaty, S., & Mintova, S. (2019). Microwave-green synthesis of AlPO-n and SAPO-n (n= 5 and 18) nanosized crystals and their assembly in layers. *Microporous and Mesoporous Materials, 280*, 256-263.

Ng, E.-P., Delmotte, L., & Mintova, S. (2008). Environmentally benign synthesis of nanosized aluminophosphate enhanced by microwave heating. *Green Chemistry, 10*, 1043-1048.

Ng, E.-P., Sekhon, S. S., & Mintova, S. (2009). Discrete MnAlPO-5 nanocrystals synthesized by an ionothermal approach. *Chemical Communications*, *13*, 1661-1663.

Ng, E. P., Itani, L., Sekhon, S. S., & Mintova, S. (2010). Micro-to Macroscopic Observations of MnAlPO-5 Nanocrystal Growth in Ionic-Liquid Media. *Chemistry–A European Journal, 16*, 12890-12897.

Oh, H.-C., Jung, S., Ko, I.-J., & Choi, E.-Y. (2018). Ionothermal synthesis of metal-organic Framework. *Recent Advancements in the Metallurgical Engineering and Electrodeposition*, (pp. 1-24). IntechOpen, London.

Okejiri, F. U. (2021). Ultrasound-Driven Fabrication of Nanosized High-Entropy Materials for Heterogeneous Catalysis. [Doctoral dissertation, University of Tennessee], Knoxville.

Orazbayev, B., Kozhakhmetova, D., Wójtowicz, R., & Krawczyk, J. (2020). Modeling of a catalytic cracking in the gasoline production installation with a fuzzy environment. *Energies*, *13*, 4736.

Othman, R., Dicks, A. L., & Zhu, Z. (2012). Non precious metal catalysts for the PEM fuel cell cathode. *International Journal of Hydrogen Energy*, *37*, 357-372.

Panczyk, T., Gac, W., Panczyk, M., Borowiecki, T., & Rudzinski, W. (2006). On the Equilibrium Nature of Thermodesorption Processes. TPD-NH_3 Studies of Surface Acidity of Ni/MgO− Al_2O_3 Catalysts. *Langmuir, 22*, 6613-6621.

Parameshwaran, R., Sarı, A., Jalaiah, N., & Karunakaran, R. (2018). Applications of thermal analysis to the study of phase-change materials. *Handbook of Thermal Analysis and Calorimetry*, 6, 519-572.

Parnham, E. R., Wheatley, P. S., & Morris, R. E. (2006). The ionothermal synthesis of SIZ-6—a layered aluminophosphate. *Chemical Communications*, *4*, 380-382.

Pastore, H., Coluccia, S., & Marchese, L. (2005). Porous aluminophosphates: from molecular sieves to designed acid catalysts. *Annu. Rev. Mater. Res.*, *35*, 351-395.

Paul, G., Bisio, C., Braschi, I., Cossi, M., Gatti, G., Gianotti, E., & Marchese, L. (2018). Combined solid-state NMR, FT-IR and computational studies on layered and porous materials. *Chemical Society Reviews*, *47*, 5684-5739.

Pileidis, F. D., Tabassum, M., Coutts, S., & Titirici, M.-M. (2014). Esterification of levulinic acid into ethyl levulinate catalysed by sulfonated hydrothermal carbons. *Chinese Journal of Catalysis*, *35*, 929-936.

Potter, M. E. (2020). Down the microporous rabbit hole of silicoaluminophosphates: Recent developments on synthesis, characterization, and catalytic applications. *ACS Catalysis, 10*, 9758-9789.

Pradhan, S., Rajamani, S., Agrawal, G., Dash, M., & Samal, S. (2017). NMR, FT-IR and raman characterization of biomaterials. *Characterization of Polymeric Biomaterials* (pp. 147-173). Elsevier, Amsterdam.

Qu, W., Liu, X., Chen, J., Dong, Y., Tang, X., & Chen, Y. (2020). Single-atom catalysts reveal the dinuclear characteristic of active sites in NO selective reduction with NH_3. *Nature Communications, 11*, 1532.

Rabaev, M., Landau, M. V., Vidruk-Nehemya, R., Koukouliev, V., Zarchin, R., & Herskowitz, M. (2015). Conversion of vegetable oils on Pt/Al_2O_3/SAPO-11 to diesel and jet fuels containing aromatics. *Fuel, 161*, 287-294.

Radnik, J., Dang, T. T. H., Gatla, S., Raghuwanshi, V. S., Tatchev, D., & Hoell, A. (2019). Identifying the location of Cu ions in nanostructured SAPO-5 molecular sieves and its impact on the redox properties. *RSC Advances, 9*, 6429-6437.

Raman, G. (2023). Identifying extra-large pore structures in zeolites with a machine learning approach and its deployment into production. *Microporous and Mesoporous Materials*, *348*, 112362.

Ramli, N. A. S., Sivasubramaniam, D., & Amin, N. A. S. (2017). Esterification of levulinic acid using ZrO_2-supported phosphotungstic acid catalyst for ethyl levulinate production. *BioEnergy Research*, *10*, 1105-1116.

Rana, K. K., & Rana, S. (2014). Microwave reactors: A brief review on its fundamental aspects and applications. *Open Access Library Journal*, *1*, 1-20.

Ravi, M., Sushkevich, V. L., & van Bokhoven, J. A. (2020). Towards a better understanding of Lewis acidic aluminium in zeolites. *Nature Materials*, *19*, 1047-1056.

Ren, L., Wu, Q., Yang, C., Zhu, L., Li, C., Zhang, P., Zhang, H., Meng, X., & Xiao, F.-S. (2012). Solvent-free synthesis of zeolites from solid raw materials. *Journal of the American Chemical Society*, *134*, 15173-15176.

Ren, X., Ghazani, M. S., Zhu, H., Ao, W., Zhang, H., Moreside, E., Zho, J., Yang, P., Zhong, N., & Bi, X. (2022). Challenges and opportunities in microwave-assisted catalytic pyrolysis of biomass: A review. *Applied Energy*, *315*, 118970.

Resasco, D. E., Crossley, S. P., Wang, B., & White, J. L. (2021). Interaction of water with zeolites: a review. *Catalysis Reviews*, *63*, 302-362.

Rilyanti, M., Mukti, R. R., Kadja, G. T., Ogura, M., Nur, H., & Ng, E.-P. (2016). On the drastic reduction of organic structure directing agent in the steam-assisted crystallization of zeolite with hierarchical porosity. *Microporous and Mesoporous Materials, 230*, 30-38.

Rizzo, C., Carati, A., Tagliabue, M., & Perego, C. (2000). Synthesis and textural properties of amorphous silica-aluminas. *Studies in Surface Science and Catalysis*, 613-622.

Roldán, R., Sánchez-Sánchez, M., Sankar, G., Romero-Salguero, F. J., & Jiménez-Sanchidrián, C. (2007). Influence of pH and Si content on Si incorporation in SAPO-5 and their catalytic activity for isomerisation of n-heptane over Pt loaded catalysts. *Microporous and Mesoporous Materials*, *99*, 288-298.

Said, S., & Zaky, M. T. (2022). PtSn supported on hierarchical mesoporous SAPO-11: Synthesis, characterization and catalytic evaluation in n-heptane hydroisomerization. *Journal of Organometallic Chemistry, 957*, 122180.

Saleh, T. A. (2022). Adsorption technology and surface science. *Interface Science and Technology*, 39-64.

Salvatella, L. (2017). The alkyl group is a-I+ R substituent. *Educación Química*, *28*, 232-237.

Samanta, S., Bhunia, K., Pradhan, D., Satpati, B., & Srivastava, R. (2018). $NiCuCo_2O_4$ supported Ni–Cu ion-exchanged mesoporous zeolite heteronano architecture: an efficient, stable, and economical nonprecious electrocatalyst for methanol oxidation. *ACS Sustainable Chemistry & Engineering*, *6*, 2023-2036.

Sánchez-Sánchez, M., Romero, Á. A., Pinilla-Herrero, I., & Sastre, E. J. C. T. (2017). Ionothermal preparation of triclinic SAPO-34 and its catalytic performance in the MTO process. *Catalysis Today, 296*, 239-246.

Sani, Y. M., Daud, W. M. A. W., & Aziz, A. A. (2014). Activity of solid acid catalysts for biodiesel production: a critical review. *Applied Catalysis A: General*, *470*, 140-161.

Santiago, O., Walsh, K., Kele, B., Gardner, E., & Chapman, J. (2016). Novel pre-treatment of zeolite materials for the removal of sodium ions: potential materials for coal seam gas co-produced wastewater. *SpringerPlus*, *5*, 1-16.

Santos, I. C., & Schug, K. A. (2017). Recent advances and applications of gas chromatography vacuum ultraviolet spectroscopy. *Journal of Separation Science*, *40*, 138-151.

Santos, L. A. d., Fraga, G. d. V., Pontes, D. A., Campos, L., Pontes, L. A., & Teixeira, L. S. (2021). Alternatives for the production of levulinic acid obtained from biomass. *Química Nova*, *44*, 1300-1310.

Sedighi, M., Towfighi, J., & Mohamadalizadeh, A. (2014). Effect of phosphorus and water contents on physico-chemical properties of SAPO-34 molecular sieve. *Powder Technology*, *259*, 81-86.

Serrano-Ruiz, J. C., & Dumesic, J. A. (2011). Catalytic routes for the conversion of biomass into liquid hydrocarbon transportation fuels. *Energy & Environmental Science*, *4*, 83-99.

Shalmani, F. M., Askari, S., & Halladj, R. (2013). Microwave synthesis of SAPO molecular sieves. *Reviews in Chemical Engineering*, *29*, 99-122.

Shamanaeva, I., Strelova, S., Solovyeva, M., & Grekova, A. (2022). Rapid and effective way to synthesize highly crystalline nanosized SAPO-34 particles. *Nanomaterials*, *12*, 4086.

Shannon, R. D. (1976). Revised effective ionic radii and systematic studies of interatomic distances in halides and chalcogenides. *Foundations of Crystallography, 32*, 751-767.

Shao, H., Chen, J., Zhong, J., Leng, Y., & Wang, J. (2015). Development of MeSAPO-5 molecular sieves from attapulgite for dehydration of carbohydrates. *Industrial & Engineering Chemistry Research, 54*, 1470-1477.

Shi, J., Yang, Z., Dai, H., Lu, X., Peng, L., Tan, X., Shi, L., & Fahim, R. (2018). Preparation and application of modified zeolites as adsorbents in wastewater treatment. *Water Science and Technology*, *2017*, 621-635.

Shuit, S. H., Ng, E. P., & Tan, S. H. (2015). A facile and acid-free approach towards the preparation of sulphonated multi-walled carbon nanotubes as a strong protonic acid catalyst for biodiesel production. *Journal of the Taiwan Institute of Chemical Engineers*, *52*, 100-108.

Silva, A. V., Miranda, L. S., Nele, M., Louis, B., & Pereira, M. M. (2016). Insights to achieve a better control of silicon-aluminum ratio and ZSM-5 zeolite crystal morphology through the assistance of biomass. *Catalysts*, *6*, 30.

Sing, K. S. (1985). Reporting physisorption data for gas/solid systems with special reference to the determination of surface area and porosity (Recommendations 1984). *Pure and Applied Chemistry*, *57*, 603-619.

Skoog, D., Holler, F., & Crouch, S. (2017). Principles of instrumental analysis: Cengage learning. *Cengage Learning,* Boston.

Smail, H. A., Rehan, M., Shareef, K. M., Ramli, Z., Nizami, A.-S., & Gardy, J. (2019). Synthesis of uniform mesoporous zeolite ZSM-5 catalyst for friedel-crafts acylation. *ChemEngineering, 3*, 35.

Song, M., Di, X., Zhang, Y., Sun, Y., Wang, Z., Yuan, Z., & Guo, Y. (2021). The effect of enzyme loading, alcohol/acid ratio and temperature on the enzymatic esterification of levulinic acid with methanol for methyl levulinate production: a kinetic study. *RSC Advances*, *11*, 15054-15059.

Souissi, F. Z., Ettoumi, H., Barré, M., & Toumi, M. (2018). Preparation and electrical conductivity of potassium phosphate glasses containing Al_2O_3. *Journal of Non-Crystalline Solids, 481*, 585-589.

Soulard, M., Bilger, S., Kessler, H., & Guth, J. (1991). Characterization of the products remaining in the solid after partial thermal decomposition of Pr_4NF-, Pr_3NHF-, and Pr_4NOH-MFI precursors. *Zeolites*, *11*, 107-115.

Stanciakova, K., & Weckhuysen, B. (2021). Water–active site interactions in zeolites and their relevance in catalysis. *Trends in Chemistry*, *3*, 456-468.

Su, H., Yan, Y., Zhang, J.-N., & Yan, W. (2023). CO_2 captured by silicoaluminophosphate (SAPO) zeotypes. *Sustainable Chemistry for Climate Action*, *1,* 100022.

Tago, T., & Masuda, T. (2010). Zeolite nanocrystals-synthesis and applications. *InTech, Faculty of Engineering, Hokkaido University, Hokkaido*.

Takacs, L. (2013). The historical development of mechanochemistry. *Chemical Society Reviews*, *42*, 7649-7659.

Tanaka, S. (2020). Mechanochemical synthesis of MOFs. *Metal-Organic Frameworks for Biomedical Applications*, 197-222.

Tao, S., Li, X., Lv, G., Wang, C., Xu, R., Ma, H., & Tian, Z. (2017). Highly mesoporous SAPO-11 molecular sieves with tunable acidity: facile synthesis, formation mechanism and catalytic performance in hydroisomerization of n-dodecane. *Catalysis Science & Technology*, *7*, 5775-5784.

Terasaka, K., Imai, H., & Li, X. (2015). Control of Morphology and acidity of SAPO-5 for the methanol-to-olefins (MTO) reaction. *J. Adv. Chem. Eng, 5*, 1000138.

Tiuliukova, I., Rudina, N., Lysikov, A., Cherepanova, S., & Parkhomchuk, E. (2018). Screw-like morphology of silicoaluminophosphate-11 (SAPO-11) crystallized in ethanol medium. *Materials Letters*, *228*, 61-64.

Tosheva, L., Ng, E.-P., Mintova, S., Holzl, M., Metzger, T. H., & Doyle, A. M. (2008). $AlPO_4$-18 seed layers and films by secondary growth. *Chemistry of Materials*, *20*, 5721-5726.

Travkina, O., Agliullin, M., Filippova, N., Khazipova, A., Danilova, I., Grigor'Eva, N., Narender, N., Pavlov, M. L., & Kutepov, B. (2017). Template-free synthesis of high degree crystallinity zeolite Y with micro–meso–macroporous structure. *RSC Advances, 7*, 32581-32590.

Trincado, M., Banerjee, D., & Grützmacher, H. (2014). Molecular catalysts for hydrogen production from alcohols. *Energy & Environmental Science, 7*, 2464-2503.

Umehara, Y., Itakura, M., Yamanaka, N., Sadakane, M., & Sano, T. (2013). First synthesis of SAPO molecular sieve with LTL-type structure by hydrothermal conversion of SAPO-37 with FAU-type structure. *Microporous and Mesoporous Materials*, *179*, 224-230.

Unlu, D., Ilgen, O., & Hilmioglu, N. D. (2016). Biodiesel additive ethyl levulinate synthesis by catalytic membrane: SO_4^{2-}/ZrO_2 loaded hydroxyethyl cellulose. *Chemical Engineering Journal*, *302*, 260-268.

Utchariyajit, K., & Wongkasemjit, S. (2010). Effect of synthesis parameters on mesoporous SAPO-5 with AFI-type formation via microwave radiation using alumatrane and silatrane precursors. *Microporous and Mesoporous Materials*, *135*, 116-123.

Verdoliva, V., Saviano, M., & De Luca, S. (2019). Zeolites as acid/basic solid catalysts: recent synthetic developments. *Catalysts, 9*, 248.

Wang, C., Leng, S., Guo, H., Cao, L., & Huang, J. J. A. S. S. (2019). Acid and alkali treatments for regulation of hydrophilicity/hydrophobicity of natural zeolite. *478*, 319-326.

Wang, G., Valldor, M., Spielberg, E. T., & Mudring, A.-V. (2014). Ionothermal synthesis, crystal structure, and magnetic study of Co_2PO_4OH isostructural with caminite. *Inorganic Chemistry*, *53*, 3072-3077.

Wang, K., Zhang, J., Fan, S., Peng, X., Tsubaki, N., & Zhao, T.-S. (2021). Transformation of LPG to light olefins on composite HZSM-5/SAPO-5. *New Journal of Chemistry, 45*, 4860-4866.

Wang, P., Liu, H., Wang, C., Lv, G., Wang, D., Ma, H., & Tian, Z. (2021). Direct synthesis of shaped MgAPO-11 molecular sieves and the catalytic performance in n-dodecane hydroisomerization. *RSC Advances, 11*, 25364-25374.

Wang, P., Lv, A., Hu, J., & Lu, G. (2012). The synthesis of SAPO-34 with mixed template and its catalytic performance for methanol to olefins reaction. *Microporous and Mesoporous Materials*, *152*, 178-184.

Wang, W., Xu, J., & Deng, F. (2022). Recent advances in solid-state NMR of zeolite catalysts. *National Science Review, 9*, 155.

Wang, X., Guo, F., Wei, X., Liu, Z., Zhang, W., Guo, S., & Zhao, L. (2016). The catalytic performance of methylation of naphthalene with methanol over SAPO-11 zeolites synthesized with different Si content. *Korean Journal of Chemical Engineering*, *33*, 2034-2041.

Wang, Y., Chen, S.-L., Jiang, Y.-J., Cao, Y.-Q., Chen, F., Chang, W.-K., & Gao, Y.-L. (2016). Influence of template content on selective synthesis of SAPO-18, SAPO-18/34 intergrowth and SAPO-34 molecular sieves used for methanol-to-olefins process. *RSC Advances*, *6*, 104985-104994.

Wang, Y., Xu, Y., Li, D., Liu, H., Li, X., Tao, S., & Tian, Z. (2015). Ionothermal synthesis of zeolitic imidazolate frameworks and the synthesis dissolution-crystallization mechanism. *Chinese Journal of Catalysis*, *36*, 855-865.

Wasanasuk, K., & Tashiro, K. (2011). Crystal structure and disorder in Poly (l-lactic acid) δ form (α′ form) and the phase transition mechanism to the ordered α form. *Polymer*, *52*, 6097-6109.

Waseda, Y., Matsubara, E., & Shinoda, K. (2011). *X-ray diffraction crystallography: introduction, examples and solved problems*. Springer Science & Business Media, Cham.

Welton, T. (1999). Room-temperature ionic liquids. Solvents for synthesis and catalysis. *Chemical Reviews, 99*, 2071-2084.

Wen, C., Wang, X., Xu, J., & Fan, Y. (2019). Hierarchical SAPO-11 molecular sieve-based catalysts for enhancing the double-branched hydroisomerization of alkanes. *Fuel*, *255*, 115821.

Wen, J., Dong, H., & Zeng, G. (2018). Application of zeolite in removing salinity/sodicity from wastewater: A review of mechanisms, challenges and opportunities. *Journal of Cleaner Production*, *197*, 1435-1446.

West, M., Ellis, A. T., Potts, P. J., Streli, C., Vanhoof, C., & Wobrauschek, P. J. J. o. A. A. S. (2016). 2016 Atomic Spectrometry Update–a review of advances in X-ray fluorescence spectrometry and its applications. *31*, 1706-1755.

Wightman, R. (2022). An overview of cryo-scanning electron microscopy techniques for plant imaging. *Plants*, *11*, 1113.

Wojnarowicz, J., Chudoba, T., & Lojkowski, W. (2020). A review of microwave synthesis of zinc oxide nanomaterials: Reactants, process parameters and morphologies. *Nanomaterials*, *10*, 1086.

Wondraczek, L., Gao, G., Möncke, D., Selvam, T., Kuhnt, A., Schwieger, W., Palles, D., & Kamitsos, E. I. (2013). Thermal collapse of SAPO-34 molecular sieve towards a perfect glass. *Journal of Non-Crystalline Solids*, *360*, 36-40.

Wong, S.-F., Awala, H., Vincente, A., Retoux, R., Ling, T. C., Mintova, S., Mukti, R. R., & Ng, E.-P. (2017). KF zeolite nanocrystals synthesized from organic-template-free precursor mixture. *Microporous and Mesoporous Materials*, *249*, 105-110.

Wong, S.-F., Deekomwong, K., Wittayakun, J., Ling, T. C., Muraza, O., Adam, F., & Ng, E.- P. (2017). Crystal growth study of KF nanozeolite and its catalytic behavior in Aldol condensation of benzaldehyde and heptanal enhanced by microwave heating. *Materials Chemistry and Physics, 196*, 295-301.

Wu, Q., Meng, X., Gao, X., & Xiao, F.-S. (2018). Solvent-free synthesis of zeolites: mechanism and utility. *Accounts of Chemical Research*, *51*, 1396-1403.

Xiang, M., Shi, Z., Zhang, X., Gao, Z., Guo, J., Wu, Z., Ma, S., Bai, J., & Deng, Y. (2024). Facile synthesis of hierarchical SAPO-56 zeolite as a highly efficient catalyst for CO_2 hydrogenation to methanol. *Fuel, 361*, 130663.

Xiao, Z., Zhan, W., Guo, Y., Guo, Y., Gong, X., & Lu, G. (2016). The synthesis of Co-doped SAPO-5 molecular sieve and its performance in the oxidation of cyclohexane with molecular oxygen. *Chinese Journal of Catalysis, 37*, 273-280.

Xing, G., Liu, S., Guan, Q., & Li, W. (2019). Investigation on hydroisomerization and hydrocracking of C_{15}–C_{18} n-alkanes utilizing a hollow tubular Ni-Mo/SAPO-11 catalyst with high selectivity of jet fuel. *Catalysis Today, 330*, 109-116.

Xu, H., & Wu, P. (2022). New progress in zeolite synthesis and catalysis. *National Science Review*, *9*, nwac045.

Xu, J., Haw, K.-G., Li, Z., Pati, S., Wang, Z., & Kawi, S. (2021). A mini-review on recent developments in SAPO-34 zeolite membranes and membrane reactors. *Reaction Chemistry & Engineering*, *6,* 52-66.

Xu, W. P., Chen, X. F., Guo, H. J., Li, H. L., Zhang, H. R., Xiong, L., & Chen, X. D. (2021). Conversion of levulinic acid to valuable chemicals: A review. *Journal of Chemical Technology & Biotechnology*, *96*, 3009-3024.

Xu, X. T., Zhai, J. P., Li, I. L., & Ruan, S. C. (2013). Morphology Control of SAPO-11 and SAPO-47 Crystals in the Presence of Diethylamine. *Applied Mechanics and Materials*, *275*, 1737-1741.

Xu, Y. P., Tian, Z. J., Wang, S. J., Hu, Y., Wang, L., Wang, B. C., Ma, Y-C., Hou, L., Yu J-Y., & Lin, L. W. (2006). Microwave-enhanced ionothermal synthesis of aluminophosphate molecular sieves. *Angewandte Chemie International Edition, 45*, 3965-3970.

Yadav, R., & Singh, A. K. (2021). Recent developments on clean fuels over SAPO-type catalysts. *Catalysis for Clean Energy and Environmental Sustainability: Petrochemicals and Refining Processes, 2*, 503-525.

Yan, K., Lafleur, T., Wu, X., Chai, J., Wu, G., & Xie, X. (2015). Cascade upgrading of γ-valerolactone to biofuels. *Chemical Communications*, *51*, 6984-6987.

Yang, G., & Park, S.-J. (2019). Conventional and microwave hydrothermal synthesis and application of functional materials: A review. *Materials*, *12*, 1177.

Yang, L., Wang, W., Song, X., Bai, X., Feng, Z., Liu, T., & Wu, W. (2019). The hydroisomerization of n-decane over Pd/SAPO-11 bifunctional catalysts: The effects of templates on characteristics and catalytic performances. *Fuel Processing Technology*, *190*, 13-20.

Yang, M., Fan, D., Wei, Y., Tian, P., & Liu, Z. (2019). Recent progress in methanol-to-olefins (MTO) catalysts. *Advanced Materials, 31*, 1902181.

Yang, S.-T., Kim, J.-Y., Chae, H.-J., Kim, M., Jeong, S.-Y., & Ahn, W.-S. (2012). Microwave synthesis of mesoporous SAPO-34 with a hierarchical pore structure. *Materials Research Bulletin*, *47*, 3888-3892.

Yang, Z., Li, J., Liu, Y., & Liu, C. (2017). Effect of silicon precursor on silicon incorporation in SAPO-11 and their catalytic performance for hydroisomerization of n-octane on Pt-based catalysts. *Journal of Energy Chemistry*, *26*, 688-694.

Yang, Z., Zhang, L., Zhou, Y., Wang, H., Wen, L., & Kianfar, E. (2020). Investigation of effective parameters on SAPO-34 nanocatalyst in the methanol-to-olefin conversion process: a review. *Reviews in Inorganic Chemistry*, *40*, 91-105.

Ye, L., Cao, F., Ying, W., Fang, D., & Sun, Q. (2011). Effect of different TEAOH/DEA combinations on SAPO-34's synthesis and catalytic performance. *Journal of Porous Materials*, *18*, 225-232.

Yu, L., Yu, X. Y., & Lou, X. W. (2018). The Design and Synthesis of Hollow Micro-/Nanostructures: Present and Future Trends. *Advanced Materials*, *30*, 1800939.

Yu, Q., Guo, Y., Wu, X., Yang, Z., Wang, H., Ge, Q., & Zhu, X. (2021). Ketonization of propionic acid on Lewis acidic Zr-beta zeolite with improved stability and selectivity. *ACS Sustainable Chemistry & Engineering, 9*, 7982-7992.

Yu, J., & Xu, R. J. A. o. c. r. (2003). Rich structure chemistry in the aluminophosphate family. *36*, 481-490.

Zeng, X., Hu, X., Song, H., Xia, G., Shen, Z.-Y., Yu, R., & Moskovits, M. (2021). Microwave synthesis of zeolites and their related applications. *Microporous and Mesoporous Materials*, *323*, 111262.

Zhang, S., Chen, S.-L., Dong, P., Yuan, G., & Xu, K. (2007). Characterization and hydroisomerization performance of SAPO-11 molecular sieves synthesized in different media. *Applied Catalysis A: General*, *332*(1), 46-55.

Zhang, Y., Ding, H., Li, L., Zhu, K., & Liu, J. (2022). Generating nanocrystalline SAPO-34 through bead-milling and porogen-assisted recrystallization: Structural evolution and catalytic consequence in dimethyl ether-to-olefin conversion. *Applied Catalysis A: General*, *632*, 118483.

Zhao, C., Yang, Y., Chen, W., Wang, H., Zhao, D., & Webley, P. A. (2009). Hydrothermal synthesis of novel $AlPO_4$-5 brooms and nano-fibers and their templated carbon structures. *CrystEngComm, 11*(5), 739-742.

Zhao, L., Yang, G., Hu, H., Sun, Y., Ma, Z., Peng, P., Ng, E.-P., Tian, P., Guo, H., & Svetlena, M. (2022). SAPO-34 crystals with nanosheet morphology synthesized by pyrophosphoric acid as new phosphorus source. *Microporous and Mesoporous Materials, 333*, 111753.

Zhao, X., Wang, H., Kang, C., Sun, Z., Li, G., & Wang, X. (2012). Ionothermal synthesis of mesoporous SAPO-5 molecular sieves by microwave heating and using eutectic solvent as structure-directing agent. *Microporous and Mesoporous Materials, 151*, 501-505.

Zhao, X., Wen, J., Zhao, J., Li, A., Li, G., & Wang, X. (2015). Hierarchically structured SAPO-5 molecular sieve catalysts with tailored mesoporosity for alkylation reaction. *Journal of Porous Materials, 22*, 577-584.

Zones, S. I., & Davis, M. E. (1996). Zeolite materials: recent discoveries and future prospects. *Current Opinion in Solid State and Materials Science, 1*, 107-117.

APPENDICES

APPENDIX 1

GC-FID chromatographs (a) before and (b) after the esterification of levulinic acid reaction in the presence of the solid acid catalyst SAPO-11 under non-microwave instant heating method (180 ˚C, 30 min)

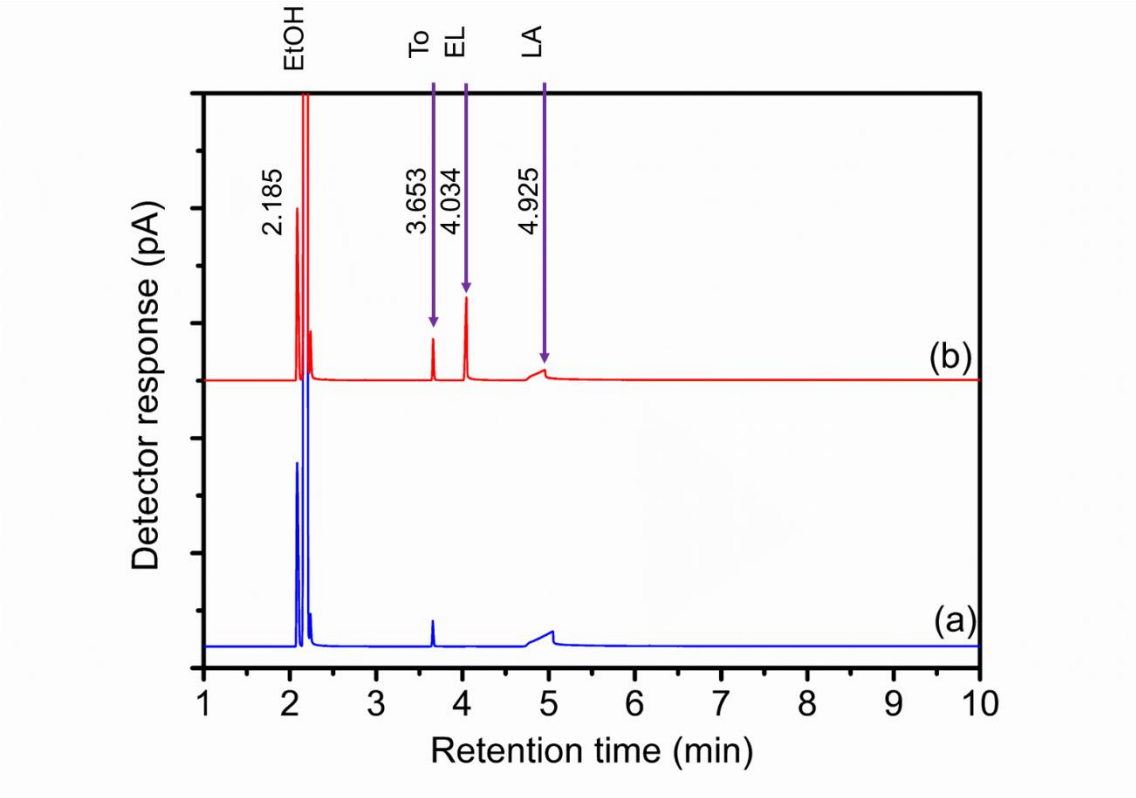

APPENDIX 2

Mass spectrum of ethyl levulinate

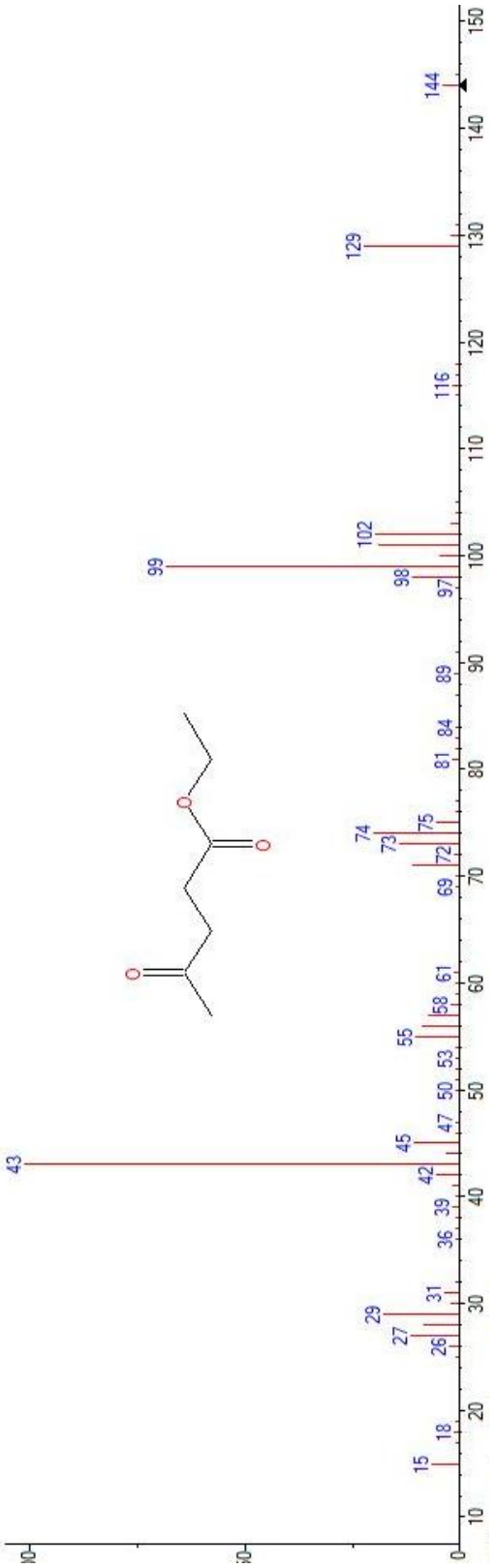

APPENDIX 3

Mass balance of catalytic esterification of levulinic acid and ethanol reaction

Theoretical:

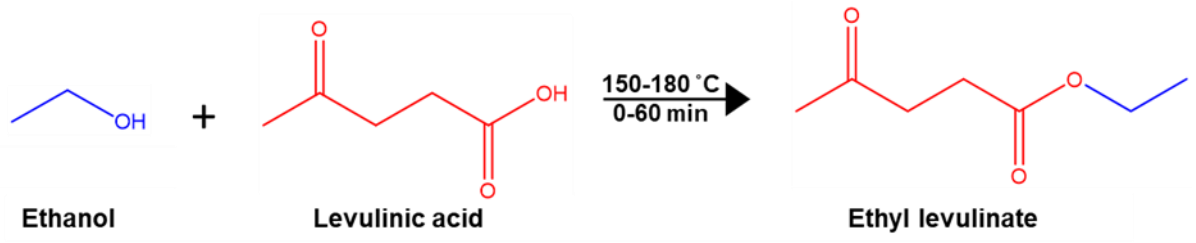

Basis: 0.664 g ethanol with 0.142 g levulinic acid have been used, 93.4% conversion and 100% selective of ethyl levulinate at 180 °C, 30 min.

Reactants:

Ethanol (MW 46.068 g mol^{-1}) = 0.664 g ≡ 14.37 mmol (99.7%)

Levulinic acid (MW 116.11 g mol^{-1}) = 0.142 g ≡ 1.22 mmol (99.9%)

Products formed:

Ethyl levulinate (MW 144.17 g mol^{-1}) = 0.00122* 93.4%* 144.17 *100% = 0.165 g

Water (MW 18.02 g mol^{-1}) = 0.00122* 93.4%* 18.02 *100% = 0.021 g

Reactants unreacted:

Levulinic acid (MW 116.11 g mol^{-1}) = 6.6% × 0.00122 mol × 116.11 g mol^{-1} = 0.009 g

Ethanol (MW 46.068 g mol^{-1}) = (0.01437 - (0.00122 * 93.4)) * 46.068 / 99.7% = 0.611 g

The Law of Conservation of Mass states that

{mass in} = {Mass out}

Substances	In (g)	Out (g)
Levulinic acid	0.142	0.009
Ethanol	0.664	0.611
Ethyl levulinate	0	0.165

Water	0	0.021
TOTAL	**0.806**	**0.806**

$$\% \text{ error} = \frac{0.806\ \text{g} - 0.806\ \text{g}}{0.806\ \text{g}} \times 100\%$$

$$= 0.00\%$$

Experimental:

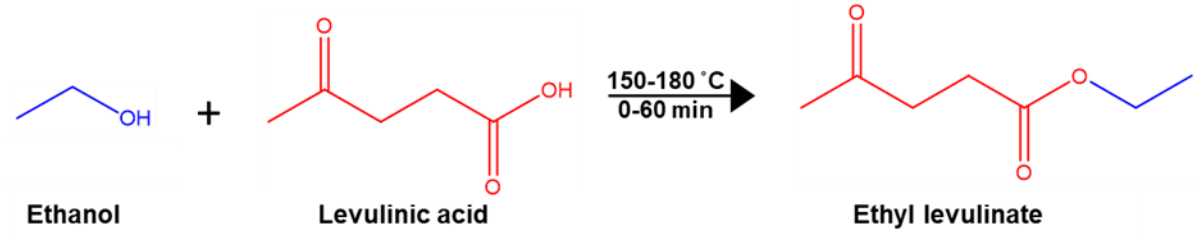

Basis: 0.664 g ethanol with 0.142 g levulinic acid have been used, 93.4% conversion and 100% selective of ethyl levulinate at 180 °C, 30 min.

Reactants:

Ethanol (MW 46.068 g mol^{-1}) = 0.664 g ≡ 14.37 mmol (99.7%)

Levulinic acid (MW 116.11 g mol^{-1}) = 0.142 g ≡ 1.22 mmol (99.9%)

Products formed:

Ethyl levulinate (MW 144.17 g mol^{-1}) = z g

Water (MW 18.02 g mol^{-1}) = x g

Reactants unreacted:

Levulinic acid (MW 116.11 g mol^{-1}) = 6.6% × 0.00122 mol × 116.11 g mol^{-1} = 0.009 g

Ethanol (MW 46.068 g mol^{-1}) = y g

Carbon atom

Mass of C atoms in levulinic acid:

$$= \left[\frac{12\ \text{g/mol} \times 5}{116.11\ \text{g/mol}}\right] \times 0.142\ \text{g}$$

= 0.073 g

Mass of C atoms in ethanol:

$$= \left[\frac{12\ \text{g/mol} \times 2}{46.068\ \text{g/mol}}\right] \times 0.664\ \text{g}$$

= 0.346 g

Mass of C atoms in ethyl levulinate produced:

$$= \left[\frac{12\ \text{g/mol} \times 7}{144.17\text{g/mol}}\right] \times \text{z g}$$

= 0.583z g

Mass of C atoms in unreacted levulinic acid:

$$= \left[\frac{12\ \text{g/mol} \times 5}{116.11\ \text{g/mol}}\right] \times 0.009\ \text{g}$$

= 0.005 g

Mass of C atoms in unreacted ethanol:

$$= \left[\frac{12\ \text{g/mol} \times 2}{46.068\ \text{g/mol}}\right] \times \text{y g}$$

= 0.521y g

∴ Mass of C atoms in = Mass of C atoms out

Mass of C atoms in (ethanol + levulinic acid) = Mass of C atoms out (ethyl levulinate + unreacted levulinic acid + unreacted ethanol)

0.073 g + 0.346 g = 0.583z g + 0.005 g + 0.521y g

Oxygen atom

Mass of O atoms in levulinic acid:

$$= \left[\frac{16.02\ \text{g/mol} \times 3}{116.11\ \text{g/mol}}\right] \times 0.142\ \text{g}$$

= 0.059 g

Mass of O atoms in ethanol:

$$= \left[\frac{16.02\ \text{g/mol} \times 1}{46.068\ \text{g/mol}}\right] \times 0.664\ \text{g}$$

= 0.231 g

Mass of O atoms in ethyl levulinate produced:

$$= \left[\frac{16.02\ \text{g/mol} \times 3}{144.17\ \text{g/mol}}\right] \times \text{z g}$$

= 0.333z g

Mass of O atoms in water produced:

$$= \left[\frac{16.02\ \text{g/mol} \times 1}{18.02\ \text{g/mol}}\right] \times \text{x g}$$

= 0.889x g

Mass of O atoms in unreacted levulinic acid:

$$= \left[\frac{16.02\ \text{g/mol} \times 3}{116.11\ \text{g/mol}}\right] \times 0.009\ \text{g}$$

= 0.004 g

Mass of O atoms in unreacted ethanol:

$$= \left[\frac{16.02\ \text{g/mol} \times 1}{46.068\ \text{g/mol}}\right] \times \text{y g}$$

= 0.348y g

∴ Mass of O atoms in = Mass of O atoms out

Mass of O atoms in (levulinic acid + ethanol) = Mass of O atoms out (ethyl levulinate produced+ water produced + unreacted levulinic acid + unreacted ethanol)

0.059 g + 0.231 g = 0.333z g + 0.889x g + 0.004 g + 0.348y g

Hydrogen atom

Mass of H atoms in levulinic acid:

$$= \left[\frac{1\ \text{g/mol} \times 8}{116.11\ \text{g/mol}}\right] \times 0.142\ \text{g}$$

= 0.010 g

Mass of H atoms in ethanol:

$$= \left[\frac{1\ \text{g/mol} \times 6}{46.068\ \text{g/mol}}\right] \times 0.664\ \text{g}$$

= 0.086 g

Mass of H atoms in ethyl levulinate produced:

$$= \left[\frac{1\ \text{g/mol} \times 12}{144.17\ \text{g/mol}}\right] \times \text{z g}$$

= 0.083z g

Mass of H atoms in water produced:

$$= \left[\frac{1\ \text{g/mol} \times 2}{18.02\ \text{g/mol}}\right] \times \text{x g}$$

= 0.111x g

Mass of H atoms in unreacted levulinic acid:

$$= \left[\frac{1\ \text{g/mol} \times 8}{116.11\ \text{g/mol}}\right] \times 0.009\ \text{g}$$

= 0.001 g

Mass of H atoms in unreacted ethanol:

$$= \left[\frac{1\ \text{g/mol} \times 6}{46.068\ \text{g/mol}}\right] \times \text{y g}$$

= 0.130y g

∴ Mass of H atoms in = Mass of H atoms out

Mass of H atoms in (levulinic acid + ethanol) = Mass of H atoms out (ethyl levulinate produced+ water produced + unreacted levulinic acid + unreacted ethanol)

0.010 g + 0.086 g = 0.083z g + 0.111x g + 0.001 g + 0.130y g

After solve these three equations:

z = 0.171 g, y = 0.603 g, x = 0.022 g

The Law of Conservation of Mass states that

{mass in} = {Mass out}

Substances	In (g)	Out (g)
Levulinic acid	0.142	0.009
Ethanol	0.664	0.603
Ethyl levulinate	0	0.171
Water	0	0.022
TOTAL	**0.806**	**0.805**

$$\% \text{ error} = \frac{0.806\ \text{g} - 0.805\ \text{g}}{0.806\ \text{g}} \times 100\%$$

= 0.10%

APPENDIX 4

GC-FID chromatographs (a) before and (b) after the esterification of SAPO-5 reaction in the presence of the solid acid catalyst SAPO-5 under non-microwave instant heating method (160 ˚C, 20 min)

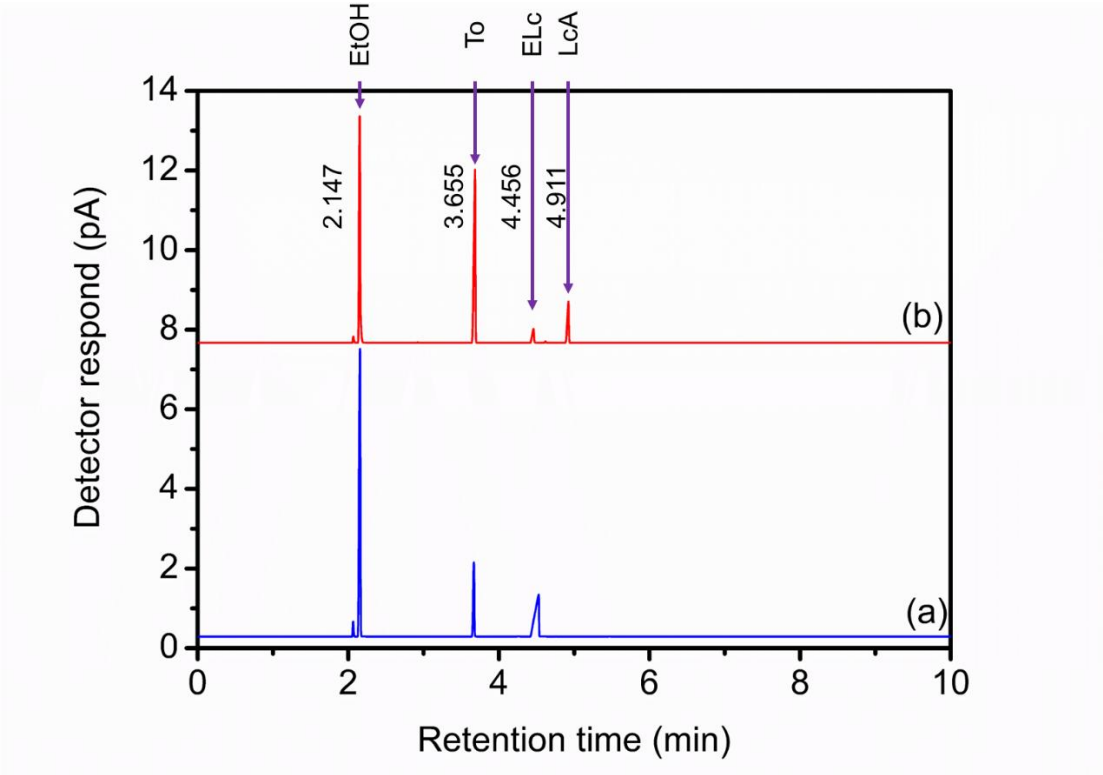

APPENDIX 5
Mass spectrum of ethyl lactate

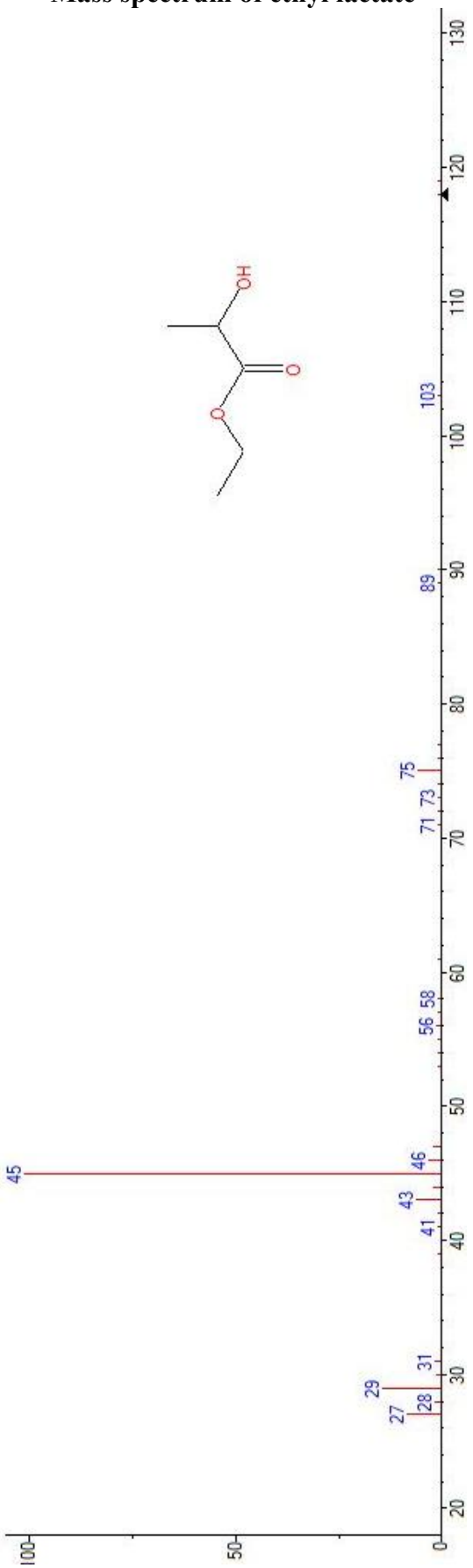

APPENDIX 6

Mass balance of catalytic esterification of lactic acid and ethanol reaction

Theoretical

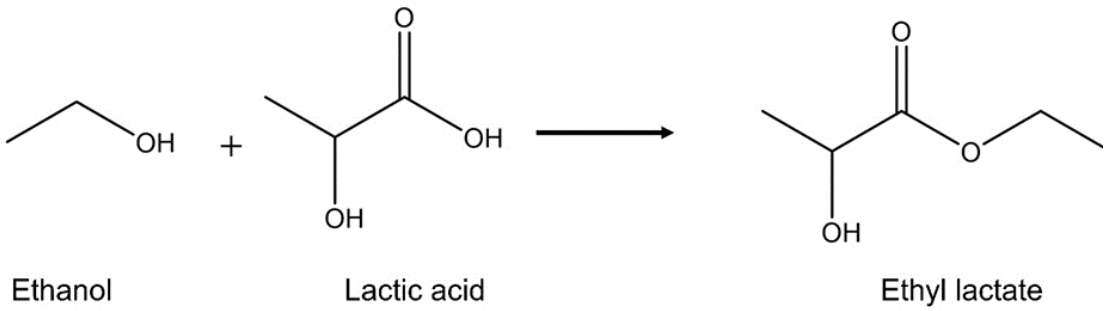

Basis: 0.482 g ethanol with 0.105 g lactic acid have been used, 87.0% conversion and 100% selective of ethyl lactate at 160 °C, 20 min.

Reactants:

Ethanol (MW 46.068 g mol^{-1}) = 0.482 g = 10.4 mmol (99.7%)

Lactic acid (MW 90.08 g mol^{-1}) = 0.105 g; (90.0%) the other 10% is water

The real mass is 0.0945 = 1.049 mmol (90.0%)

Water (MW 18.02 g mol^{-1}) = (0.105 × 10%) = 0.0105 g = 0.58 mmol (100%)

Products formed:

Ethyl lactate (MW 118.13 g mol^{-1}) = 0.001049 × 87.0% × 118.13 ×100% = 0.108 g

Water (MW 18.02 g mol^{-1}) = 0.001049 × 87.0% × 18.02 × 100% + 0.0105 = 0.027 g

Reactants unreacted:

Lactic acid (MW 90.08 g mol^{-1}) = (1-87.0%) × 0.945 g = 0.012 g

Ethanol (MW 46.068 g mol^{-1}) = (0.0104 - (0.001094 × 87.0)) × 46.068 / 99.7% = 0.440 g

The Law of Conservation of Mass states that

{mass in} = {Mass out}

Substances	In (g)	Out (g)
Lactic acid	0.0945	0.012
Ethanol	0.482	0.440
Ethyl lactate	0	0.108
Water	0.0105	0.027
TOTAL	**0.587**	**0.587**

$$\% \text{ error} = \frac{0.587\ \text{g} - 0.587\ \text{g}}{0.587\ \text{g}} \times 100\%$$

= 0.00%

Experimental

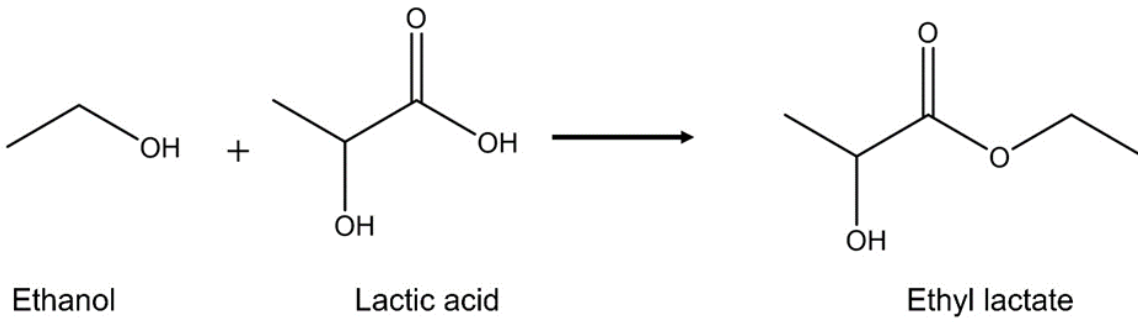

Ethanol Lactic acid Ethyl lactate

Basis: 0.482 g ethanol with 0.105 g lactic acid have been used, 87.0% conversion and 100% selective of ethyl lactate at 160 °C, 20 min.

Reactants:

Ethanol (MW 46.068 g mol^{-1}) = 0.482 g = 10.4 mmol (99.7%)

Lactic acid (MW 90.08 g mol^{-1}) = 0.105 g; (90.0%) the other 10% is water

The real mass is 0.0945 = 1.49 mmol (90.0%)

Water (MW 18.02 g mol^{-1}) = (0.105 × 10%) = 0.0105 g = 0.58 mmol (100%)

Products formed:

Ethyl lactate (MW 118.13 g mol^{-1}) = z g

Water (MW 18.02 g mol^{-1}) = x g + 0.0105 g

Reactants unreacted:

Lactic acid (MW 90.08 g mol^{-1}) = 13.0% × 0.001049 mol × 90.08 g mol^{-1} = 0.012 g

Ethanol (MW 46.068 g mol^{-1}) = y g

Carbon atom

Mass of C atoms in lactic acid:

$$= \left[\frac{12\ \text{g/mol} \times 3}{90.08\ \text{g/mol}}\right] \times 0.0945\ \text{g}$$

= 0.038 g

Mass of C atoms in ethanol:

$$= \left[\frac{12\ \text{g/mol} \times 2}{46.068\ \text{g/mol}}\right] \times 0.482\ \text{g}$$

= 0.251 g

Mass of C atoms in ethyl lactate produced:

$$= \left[\frac{12\ \text{g/mol} \times 5}{118.13\text{g/mol}}\right] \times \text{z g}$$

= 0.508z g

Mass of C atoms in unreacted lactic acid:

$$= \left[\frac{12\ \text{g/mol} \times 3}{90.08\ \text{g/mol}}\right] \times 0.012\ \text{g}$$

= 0.005 g

Mass of C atoms in unreacted ethanol:

$$= \left[\frac{12\ \text{g/mol} \times 2}{46.068\ \text{g/mol}}\right] \times \text{y g}$$

= 0.521y g

∴ Mass of C atoms in = Mass of C atoms out

Mass of C atoms in (ethanol + lactic acid) = Mass of C atoms out (ethyl lactate + unreacted lactic acid + unreacted ethanol)

0.038 g + 0.251 g = 0.508z g + 0.005 g + 0.521y g

Oxygen atom

Mass of O atoms in lactic acid:

$$= \left[\frac{16.02\ \text{g/mol} \times 3}{90.08\ \text{g/mol}}\right] \times 0.0945\ \text{g}$$

= 0.050 g

Mass of O atoms in ethanol:

$$= \left[\frac{16.02\ \text{g/mol} \times 1}{46.068\ \text{g/mol}}\right] \times 0.482\ \text{g}$$

= 0.168 g

Mass of O atoms in ethyl lactate produced:

$$= \left[\frac{16.02\ \text{g/mol} \times 3}{118.13\ \text{g/mol}}\right] \times \text{z g}$$

= 0.407z g

Mass of O atoms in water produced:

$$= \left[\frac{16.02\ \text{g/mol} \times 1}{18.02\ \text{g/mol}}\right] \times \text{x g}$$

= 0.889x g

Mass of O atoms in unreacted lactic acid:

$$= \left[\frac{16.02\ \text{g/mol} \times 3}{90.08\ \text{g/mol}}\right] \times 0.012\ \text{g}$$

= 0.006 g

Mass of O atoms in unreacted ethanol:

$$= \left[\frac{16.02\ \text{g/mol} \times 1}{46.068\ \text{g/mol}}\right] \times \text{y g}$$

= 0.348y g

∴ Mass of O atoms in = Mass of O atoms out

Mass of O atoms in (lactic acid + ethanol) = Mass of O atoms out (ethyl leactate produced+ water produced + unreacted lactic acid + unreacted ethanol)

0.050 g + 0.168 g = 0.407z g + 0.889x g + 0.006 g + 0.348y g

Hydrogen atom

Mass of H atoms in lactic acid:

$$= \left[\frac{1\ \text{g/mol} \times 6}{90.08\ \text{g/mol}}\right] \times 0.0945\ \text{g}$$

= 0.006 g

Mass of H atoms in ethanol:

$$= \left[\frac{1\ \text{g/mol} \times 6}{46.068\ \text{g/mol}}\right] \times 0.482\ \text{g}$$

= 0.063 g

Mass of H atoms in ethyl lactate produced:

$$= \left[\frac{1\ \text{g/mol} \times 10}{118.13\ \text{g/mol}}\right] \times \text{z g}$$

= 0.085z g

Mass of H atoms in water produced:

$$= \left[\frac{1\ \text{g/mol} \times 2}{18.02\ \text{g/mol}}\right] \times \text{x g}$$

= 0.111x g

Mass of H atoms in unreacted lactic acid:

$$= \left[\frac{1\ \text{g/mol} \times 6}{90.08\ \text{g/mol}}\right] \times 0.012\ \text{g}$$

= 0.001 g

Mass of H atoms in unreacted ethanol:

$$= \left[\frac{1\ \text{g/mol} \times 6}{46.068\ \text{g/mol}}\right] \times \text{y g}$$

= 0.130y g

∴ Mass of H atoms in = Mass of H atoms out

Mass of H atoms in (lactic acid + ethanol) = Mass of H atoms out (ethyl leactate produced+ water produced + unreacted lactic acid + unreacted ethanol)

0.006 g + 0.063 g = 0.085z g + 0.111x g + 0.001 g + 0.130y g

After solve these three equations:

z = 0.113 g, y = 0.435 g, x = 0.0165 g

The Law of Conservation of Mass states that

{mass in} = {Mass out}

Substances	In (g)	Out (g)
Lactic acid	0.0945	0.012
Ethanol	0.482	0.435
Ethyl lactate	0	0.113
Water	0.0105	0.017
TOTAL	**0.587**	**0.577**

$$\%\ \text{error} = \frac{0.587\ \text{g} - 0.577\text{g}}{0.587\ \text{g}} \times 100\%$$

= 1.7%

LIST OF PUBLICATIONS

Journals

Mohammad, A. I. J. M. D., Saminathan, V., El-Bahy, Z. M., Michelin, L., Ling, T. C., & Ng, E. P. (2023). Ionothermal Crystallization of SAPO-11 Using Novel Pyridinium Ionic Liquid and Its Catalytic Activity in Esterification of Levulinic Acid into Ethyl Levulinate. ***Catalysts*****,** *13*, 433. (Q2 IF: 3.8)

Mohammad, A. I. J. M. D., Pace, L., Rodríguez-Carballo, G., Vicente, A., Chia, S., Juan, J. C., Maireles-Torres, P., Mintova, S., & Ng, E. P. (2024). Formation mechanism and catalytic behavior of pyridinium-templated SAPO-5 zeolites using different phosphorus sources. ***Materials Chemistry and Physics***, 130261. (Q2 IF: 4.3)